Tréhu, A.M., Bohrmann, G., Rack, F.R., Torres, M.E., et al., 2003
Proceedings of the Ocean Drilling Program, Initial Reports Volume 204

10. Site 1251[1]

Shipboard Scientific Party[2]

INTRODUCTION

Site 1251 (proposed Site HR2alt) was drilled in ~1210 m of water, ~5.5 km east of the southern summit of Hydrate Ridge (see Fig. F1, p. 51, in the "Leg 204 Summary" chapter). The site is located in a slope basin where well-stratified sediments were apparently deposited at a rapid rate. Seismic data record a history of deposition, tilting, folding, and depositional hiatuses in the basin that are probably related to the evolution of Hydrate Ridge. A strong bottom-simulating reflector (BSR) suggests that the base of the gas hydrate stability zone (GHSZ) is at ~200 meters below seafloor (mbsf) at this site.

The principal objectives at Site 1251 were the following:

1. Determine the source of gases forming gas hydrates in a setting that is characterized by rapid deposition of hemipelagic sediments and mass-wasting deposits, in contrast to the uplifted sediments of the accretionary complex.
2. Determine the distribution of gas hydrates in relation to the typical lithological parameters for the basin.
3. Test general models for hydrate formation in regions of rapid sediment accumulation that were developed in the Blake Ridge area from results of Ocean Drilling Program (ODP) Leg 164.
4. Provide age constraints on the geological history recorded by seismic stratigraphy.

Eight holes were drilled at Site 1251 (Fig. F1). In Hole 1251A, logging-while-drilling (LWD) measurements were made using a variable, but generally low, ROP in the upper 30 mbsf, followed by an increased ROP of ~50 m/hr from 30 mbsf to the bottom of the hole at 380 mbsf. Hole 1251B was cored with the advanced piston corer (APC) (Cores 204-1251B-1H through 24H) to 194.6 mbsf with average recovery of 80.6%.

F1. Bathymetric map, p. 39.

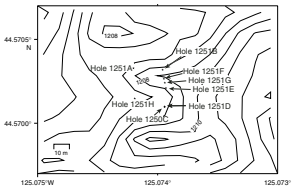

[1]Examples of how to reference the whole or part of this volume.
[2]Shipboard Scientific Party addresses.

Ms 204IR-110

This interval included pressure core sampler (PCS) deployments at 105 and 154 mbsf and a Fugro Pressure Corer (FPC) deployment at 172 mbsf. At 194.6 mbsf, more lithified sediments significantly reduced the penetration of the bit. Coring continued using the extended core barrel (XCB) down to 445.1 mbsf (Cores 204-1251B-25X through 53X) with an average recovery of 85.5%. In addition to the XCB, we used all three pressure coring tools (PCS, FPC, and Hydrate Autoclave Coring Equipment [HYACE] Rotary Corer [HRC]). Hole 1251C was terminated after two cores. In Hole 1251D, which comprises 30 cores, 3 XCB cores were drilled to 26.9 mbsf, followed by APC cores to 173.4 mbsf and XCB cores to 226.5 mbsf. Holes 1251E and 1251F were each cored by APC to 9.5 mbsf for high-density geochemical and microbiological sampling. Hole 1251G was washed to 2.5 mbsf before one APC core was taken for special sampling of turbidite layers. The hole was then washed down to 20 mbsf before an additional PCS run (at 21 mbsf) was deployed. Hole 1251H was drilled for wireline logging and seismic profiling.

OPERATIONS

Eight holes were drilled at Site 1251 (Table T1), under good weather conditions. Wind speed was 0–11 kt, gusting to 21 kt; seas were 3–7 ft; swell was 5–10 ft; and the prevailing sea-surface current was from the north at ~0.5 kt. Hole 1251A was drilled without coring on 22–23 July 2002 to obtain the initial LWD data for this site, which was followed by coring Holes 1251B–1251G on 26 July–1 August. As planned before the leg, during this period the *Sonne* and *Atlantis* conducted their scheduled research programs at the Hydrate Ridge summit. The *Ewing* was scheduled to arrive on location on 12 August to assist with the seismic profiling experiments. We returned to Site 1251 on 16 August to drill Hole 1251H for wireline logging and seismic profiling.

T1. Coring summary, p. 91.

Hole 1251A was spudded at Site 1245 on 22 July to obtain the initial LWD data for this site (see "Downhole Logging," p. 30). Drilling proceeded at a moderate rate of penetration (ROP) of 25 m/hr and 15 strokes per minute (spm) circulation to mitigate formation washout below seafloor. No real-time measurement-while-drilling (MWD) or nuclear magnetic resonance (NMR) data were recorded over this interval. The ROP was increased to 50 m/hr at a bit depth of 30 mbsf and maintained to a total depth (TD) of 380 mbsf. As a result, the vertical resolution of the Resisitivity-at-the-Bit (RAB) tool images is ~10 cm and the NMR spectral data may have lower quality. The LWD string included the RAB tool, MWD, Nuclear Magnetic Resonance (NMR-MRP) tool, and Vision Neutron Density (VND) tool. The LWD operations involved changing the Azimuthal Density Neutron (ADN) tool and replacing the RAB battery prior to running pipe to the seafloor. LWD tools were pulled to the rig floor at 0900 hr on 23 July for a total bit run of 18 hr.

Hole 1251B was APC cored to 194.6 mbsf, with an average core recovery of 80.6%. At this depth, lithified sediments significantly reduced the penetration of the bit, prompting a change to XCB coring, which proceeded to 445.1 mbsf, with an average recovery of 85.5%. Hole 1251B was terminated ahead of the proposed depth of 620 mbsf, as it appeared that the primary scientific objectives had been achieved and hole stability was deteriorating.

In addition to the XCB coring, all pressure coring tools (PCS, FPC, and HRC) were used in this hole. Three PCS cores were retrieved under pressure from Hole 1251B, two above the BSR depth (which at Site 1251 is at ~200 mbsf), and one below the BSR. One FPC and one HRC were also retrieved from this hole. Whirl-Paks and perfluorocarbon tracer (PFT) were used in 13 of these cores, and the Drill String Accelerator (DSA) tool was run twice in this hole (see Table **T4,** p. 75, in the "Leg 204 Summary" chapter). Other special tools in Hole 1251B included four APCT tool and two DVTPP runs.

Hole 1251C was spudded at 0330 hr on 30 July with the APC. When the APC failed to advance, we attempted to recover an XCB core across the same interval, which recovered 5.45 m. The hole was terminated at 17.6 mbsf.

Hole 1251D was spudded at 0715 hr on 30 July, using the XCB to collect the first three cores to 26.9 mbsf, with a recovery of 40%–90%. These cores were followed by APC to refusal at 173.4 mbsf and subsequent XCB coring to 226.5 mbsf. Whirl-Paks and PFT were used on microbiology Cores 204-1251D-22X, 25X, and 26X.

A series of special tools were deployed in Hole 1251D. Temperature measurements were obtained with one run of the APCT tool and two runs of the DVTPP. Four PCS cores were retrieved to complete the depth profile at this site, and deployments of each of the FPC and HRC were conducted as engineering tests for these pressure tools (see **"Downhole Tools and Pressure Coring,"** p. 25).

Holes 1251E through 1251F were each cored by APC to 9.5 mbsf for high-density sampling. Whirl-Paks and PFT were used only in Hole 1251E (see Table **T3,** p. 73, in the "Leg 204 Summary" chapter). No special tools were used in these holes.

Hole 1251G was washed to 2.5 mbsf before one APC core was taken for special sampling of turbidite layers. The hole was then washed down to 20 mbsf, where an additional PCS was deployed (Table **T18**).

Hole 1251H was drilled to a depth of 445 mbsf as a dedicated hole for wireline logging using separate runs of the triple combination (triple combo) tool string (Temperature/Acceleration/Pressure [TAP] tool/Dual Induction Tool [DIT]/Hostile Environment Litho-Density Tool [HLDT]/Accelerator Porosity Sonde [APS]/Hostile Environment Gamma Ray Sonde [HNGS]/Inline Checkshot Tool [QSST]) and the Formation MicroScanner (FMS)-sonic (FMS/Dipole Sonic Imager [DSI]/Scintillation Gamma Ray Tool [SGT]) tool strings. Vertical and offset vertical seismic profiles were attempted with the *JOIDES Resolution* and the *Ewing* (located at an offset of ~700 m) alternating shots (see **"Downhole Logging,"** p. 30).

LITHOSTRATIGRAPHY

Site 1251 is located on the eastern flank of southern Hydrate Ridge, where sediments from the eastern slope basin were recovered (see Figs. **F1,** p. 51, and **F8,** p. 58, in the "Leg 204 Summary" chapter). Eight holes were drilled at Site 1251 (Holes 1251A–1251H), and six of these (Holes 1251B–1251G) were cored. Hole 1251A was drilled using LWD to collect a suite of downhole measurements prior to coring. Hole 1251B was cored to 442.1 mbsf (the upper 194.6 mbsf using the APC and the next 247.5 m using the XCB). Hole 1251C was cored to 17.6 mbsf (the upper 8.1 mbsf using the APC and the next 9.5 m using the XCB). Hole 1251D was cored to 230.5 mbsf (the upper 26.9 m using the XCB, followed by

147.5 m using the APC, and then 56.1 m using the XCB). Holes 1251E and 1251F were each cored to 9.5 mbsf (APC) for high-density sampling. Hole 1251G was slightly offset from Hole 1251F and washed to 2.5 m before coring to 12 mbsf (using the APC). Hole 1251G was then washed to 20 mbsf and a 1-m-long pressure core was taken (Core 204-1251G-2P). Hole 1251H was drilled to 445 mbsf TD and wireline logged.

We divide the sedimentary sequence at Site 1251 into three lithostratigraphic units (Units I–III) (Figs. **F2, F3**). This division is based on sedimentological criteria (e.g., variations in sedimentary structure and grain size or biogenic and lithologic components) and other parameters such as calcium carbonate content (expressed as weight percent $CaCO_3$), total organic carbon (TOC), and mineralogy determined from X-ray diffraction (XRD). We also compare and correlate our results with the three dimensional (3-D) seismic data, downhole LWD data, and physical property measurements (magnetic susceptibility [MS]) to better define the entire stratigraphic sequence (Figs. **F4, F5**). Based on the above criteria, we further divide lithostratigraphic Unit I into three subunits (Subunits IA–IC) and lithostratigraphic Unit II into two subunits (Subunits IIA and IIB) (Figs. **F2, F3**). Correlation of the lithostratigraphic units defined here with the other Leg 204 sites is summarized in Figure **F10,** p. 60, in the "Leg 204 Summary" chapter.

F2. Lithostratigraphic summary, p. 40.

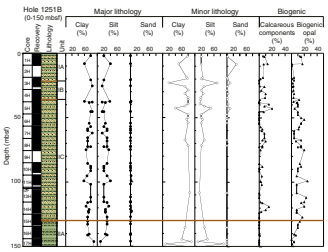

F3. Major and minor lithologies, p. 43.

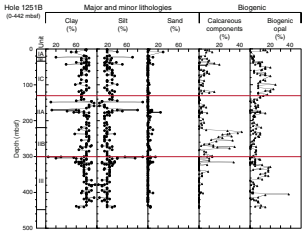

F4. Seismic reflection profile, p. 44.

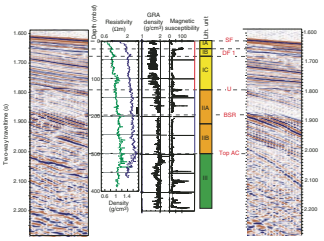

F5. Seismic reflection profile, p. 45.

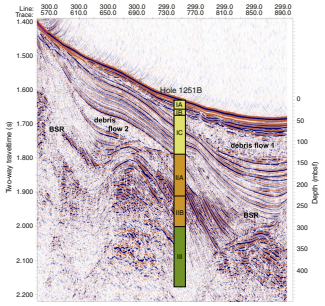

Lithostratigraphic Units

Lithostratigraphic Unit I

Intervals: Sections 204-1251B-1H-1 through 15H-4; Sections 204-1251C-1H-1 through 2X-CC; 204-1251D-1H-1 through 16H-3; Cores 204-1251E-1H; 204-1251F-1H; and 204-1251G-1H and 2P.
Depths: Hole 1251B: 0.00–130.00 mbsf; Hole 1251C: 0.00–17.60 mbsf; Hole 1251D: 0.00–130.00 mbsf; Hole 1251E: 0.00–9.50 mbsf; Hole 1251F: 0.00–9.50 mbsf; and Hole 1251G: 2.50–12.00 and 20.00–21.00 mbsf.
Age: mid-Pleistocene–Holocene

Lithostratigraphic Unit I (0–130 mbsf) is composed of silty clay and clay with interlayered sand and silt layers and mud clast deposits, which we interpret as turbidites and debris flows, respectively. Lithostratigraphic Unit I is divided into three subunits, defined as lithostratigraphic Subunits 1A (Holes 1251B [0–23 mbsf] and 1251D [0–28 mbsf] and Holes 1251C and 1251E [all cores]), IB (Holes 1251B [23–34 mbsf] and 1251D [28–34 mbsf]), and IC (Holes 1251B [34–130 mbsf] and 1251D [34–130 mbsf]), based on several sedimentological criteria.

Lithostratigraphic Subunit IA

Core recovery in the uppermost portion of lithostratigraphic Subunit IA was poor, especially in Holes 1251B and 1251D. There was no recovery for Core 204-1251B-2H and poor recovery in Cores 204-1251D-1X (39.9%) and 2X (35.3%). Core recovery improved in Cores 204-1251C-1H (101%) and 2X (57.4%) and in Cores 204-1251E-1H (104.1%), 204-1251F-1H (104.4%), and 204-1251G-1H (106.4%), but only one core was obtained from each hole.

Lithostratigraphic Subunit IA consists of dark greenish gray (5GY 4/1) clay with thin (1–5 cm thick) silt to silty sand turbidites that grade to diatom-bearing silty clay and clay (Fig. **F6A**) These graded beds increase

in frequency and thickness toward the base of lithostratigraphic Subunit IA. We place the boundary between lithostratigraphic Subunits IA and IB at 23 mbsf, the top of a seismically and lithologically distinct series of debris flow deposits (Fig. F5).

Lithostratigraphic Subunit IB

The stratigraphy of lithostratigraphic Subunit IB is dominated by zones of convoluted clay with abundant sulfide material containing unsorted clay-rich granules and pebble-sized silty clay clasts (intervals: Sections 204-1251B-3H-4 through 3H-6 and 4H-3 [all] and Sections 201-1251D-4H-1 through 4H-5) (Fig. F6B). The clasts have a noticeably different color than the matrix material (e.g., lighter and darker shades of dark greenish gray). Clasts are composed of clay and silty clay and range from 1 to 20 cm in diameter. Bioturbation and mottled sulfides are common in the clay matrix and generally absent from the clasts. Some silt layers are also present just above and within the silty clay clast layers (Section 204-1251B-2H-2). Zones of convoluted bedding are common but most often observed in the clays underlying the more clast-rich intervals.

Lithostratigraphic Subunit IC

Lithostratigraphic Subunit IC is characterized by interbedded clays and silty clays, with bioturbation and sulfides commonly observed. The relative amounts of coarse sand and silt decrease throughout the subunit, whereas the relative abundances of diatom-, foraminifer-, and nannofossil-bearing clays and silty clays increase toward the base of the subunit (Fig. F3); the frequency of visible sponge spicule clusters also increases (see **"Site 1251 Visual Core Descriptions"**). Glauconite was observed in greater amounts in Subunit IC than in the previous subunits (Fig. F7A). The percentage of sand observed in smear slides decreases throughout lithostratigraphic Unit I (e.g., is highest in lithostratigraphic Subunit IA, decreases in lithostratigraphic Subunit IB, and is lowest in lithostratigraphic Subunit IC) (Figs. F2, F3). The boundary between lithostratigraphic Subunit IC and lithostratigraphic Unit II occurs at 130 mbsf in Holes 1251B and 1251D, where an abrupt angular unconformity is seen in the 3-D seismic reflection data.

Lithostratigraphic Unit II

Intervals: Sections 204-1251B-15H-4 through 36X-CC and 204-1251D-16H-3 through 29P-1
Depths: Hole 1251B: 130.00–300.60 mbsf and Hole 1251D: 130.00–228.50 mbsf
Age: early–mid-Pleistocene

The boundary between lithostratigraphic Units I and II was placed at 130 mbsf in both Holes 1251C and 1251D. This boundary corresponds to an abrupt angular unconformity, which is seen in the 3-D seismic data (Figs. F4, F5) (see Fig. F8, p. 58, in the "Leg 204 Summary" chapter). An increased frequency of turbidites and an abundance of biogenic opal in lithostratigraphic Unit II also supports a unit boundary at this location (Figs. F2, F3).

Lithostratigraphic Unit II is composed of silty clay and clay and is divided into Subunits IIA and IIB at ~220 mbsf (Section 204-1251B-27X-5 and near the base of Hole 1251D). Below ~220 mbsf (in lithostratigraphic Subunit IIB), there is also an increase in the calcareous compo-

F6. Turbidites and soft clasts, p. 46.

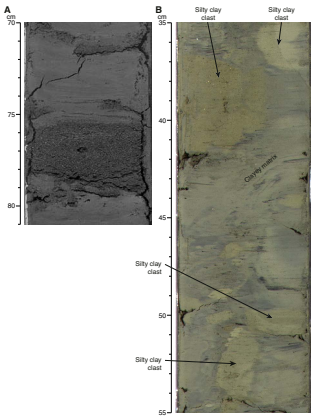

F7. Glauconite and $CaCO_3$ vs. depth, p. 47.

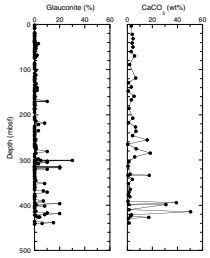

nent of the sediment (Fig. F3). Core recovery in lithostratigraphic Unit II was 80.9% in Hole 1251B and 84.9% in Hole 1251D. The base of lithostratigraphic Unit II is only present in Hole 1251B at 300 mbsf, where the character of the sediment changes and a distinct seismic reflection (the top of the accretionary complex) is observed (Figs. F4, F5) (see Fig. F8, p. 58, in the "Leg 204 Summary" chapter).

In the presence of sulfide, which is commonly found as burrow infills in highly bioturbated intervals or as disseminated horizons 1 to 5 cm thick, the color changes to very dark gray (N3). Sulfide mottles are more abundant in lithostratigraphic Subunit IIA than in Subunit IIB. A change in the character of the MS data at ~220 mbsf may reflect the change in the sulfide abundance between Subunits IIA and IIB (see "Environment of Deposition," p. 9). Where present, bedding is defined by either erosional surfaces capped with coarse silt (turbidites) or by dark sulfide horizons and is typically subhorizontal throughout both subunits. The state of lithification changes within lithostratigraphic Subunit IIB, with the base being firmer and more indurated than the top. The change from APC to XCB coring occurred at 194 mbsf in Hole 1251B and at 175 mbsf in Hole 1251D; therefore, most of the characterization of lithostratigraphic Subunit IIB is based on the examination of intact drilling biscuits from the XCB cores.

Lithostratigraphic Subunit IIA

Lithostratigraphic Subunit IIA differs from IIB in both grain size and microfossil content in smear slides, with a more abundant coarse fraction (silt and sand) in Subunit IIA and a significant increase in calcareous components in Subunit IIB (Figs. F2, F3).

Lithostratigraphic Subunit IIA consists of silty clay, which typically contains 30%–35% silt and 65%–70% clay (Figs. F2, F3). The silt fraction consists of quartz (3%–15%) and feldspar (0%–3%). Calcareous components in the sediments are rare in lithostratigraphic Subunit IIA. Only Sample 204-1251B-16H-1, 54–54 cm, contains significant amounts of calcite, as determined by XRD analysis. The lack of calcareous constituents is also mirrored in the composition of the biogenic fraction (Figs. F2, F3). Overall, biogenic components compose no more than 20% of the major and minor lithologies in lithostratigraphic Subunit IIA, and these are dominated by siliceous rather than carbonaceous components (Fig. F3). Diatoms compose up to 15% of the major and minor lithologies in Section 204-1251B-22H-5, 71 cm, whereas calcareous components compose ~3% to 9%.

Lithostratigraphic Subunit IIB

Lithostratigraphic Subunit IIB is composed of primarily clay-sized grains. The major lithology contains 15% to 20% silt and 80% to 85% clay. The quartz content of the silt-size fraction ranges from 3% to 30% and is slightly higher overall than the quartz content of lithostratigraphic Subunit IIA. The feldspar content of lithostratigraphic Subunit IIB ranges from 2% to 15% and is consistently higher than that of lithostratigraphic Subunit IIA, in which feldspar is often absent.

The biogenic components of lithostratigraphic Subunit IIB are predominantly calcareous (Fig. F3). Foraminifers first appear in smear slides in Section 204-1251B-25X (~195 mbsf) and reach a maximum of 8% in Core 28X. In Section 204-1251B-36X-CC, foraminifers are even visible without the aid of a microscope (Fig. F8A). Nannofossils, which are rare in lithostratigraphic Subunit IIA, are present in excess of 30% in lithostratigraphic Subunit IIB. The first appearance of calcareous nan-

F8. Foraminifer-rich clay, p. 48.

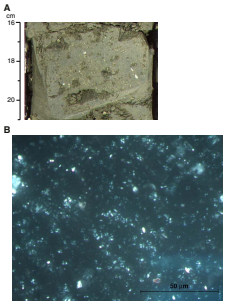

nofossils occurs in Section 204-1251B-25X-CC (~195 mbsf) (Fig. F8B). The maximum abundance of calcareous nannofossils is present in Core 204-1251B-28X, where they compose 40% of the total sediment. In Cores 204-1251B-28X through 33X (between 225 and 271 mbsf), calcareous nannofossils compose from 15% to 18% of the sediment (Fig. F3). Below 271 mbsf to the base of lithostratigraphic Unit II, they continue to compose 5%–10% of the sediment. Diatom abundance ranges from 2% to 8% throughout the subunit, which is similar to the diatom abundance observed in lithostratigraphic Subunit IIA (Fig. F3). In addition to the high biogenic carbonate content of lithostratigraphic Subunit IIB, Core 204-1251B-32X contains a carbonate-rich horizon composed of 70% authigenic calcite crystals that range in size from 1 to 5 µm in diameter. Other than this exception, both lithostratigraphic Subunits IIA and IIB lack carbonate nodules.

Pyrrhotite nodules, which are associated with the presence of sulfide, are more abundant in lithostratigraphic Subunit IIA and are absent from lithostratigraphic Subunit IIB in Hole 1251D. These nodules range in size from <0.1 to 0.2 cm in diameter. Pyrrhotite nodules are also found in lithostratigraphic Unit II in both holes (e.g., in Cores 204-1251B-15X, 20X, 29X, and 204-1251D-16H). These nodules often take the shape of burrow infilling, are attracted to a magnet, and are nonreactive in HCl.

The only gas hydrate recovered at Site 1251 was from Cores 204-1251D-22X and 24X in lithostratigraphic Subunit IIA above the BSR (Fig. F4).

Lithostratigraphic Unit III

Interval: Sections 204-1251B-37X-1 through 53X-CC
Depth: Hole 1251B: 300.6–442.62 mbsf
Age: late Pliocene–early Pleistocene

Lithostratigraphic Unit III was only drilled in Hole 1251B. In contrast to lithostratigraphic Unit II, it is composed of hard indurated clay, silty clay, and claystone with reduced calcareous components and increased biogenic opal and glauconite (Figs. F3, F7). The clay and silty clay are predominantly dark greenish gray (5GY 4/1) with lighter variations from olive to olive gray (5Y 5/3 to 5Y 5/2) in Cores 204-1251B-41X through 50X. Core recovery in lithostratigraphic Unit III was good (~88%), except in Core 204-1251B-48Y (FPC), which did not recover any sediment. All of the cores exhibited drilling disturbance; even the drilling biscuits were heavily fractured in some cases (see "Site 1251 Visual Core Descriptions").

Lithostratigraphic Unit III is characterized by its high state of lithification, diatom-rich clay, authigenic carbonate in the clay fraction, carbonate nodules, and increasing scaly clay fabric. The scaly fabric is first present in Core 204-1251B-49X and is observed in broken drilling biscuits. The boundary between lithostratigraphic Units II and III is placed at 300.6 mbsf, directly above a 120-cm-thick glauconite-bearing to glauconite-rich (<30%) silt and silty clay layer (Fig. F9A) and marks the first significant occurrence of glauconite in this hole (Fig. F7A). This concentrated presence of glauconite extends for 4.3 m to 304.9 mbsf and may correspond to an unconformity (see "Environment of Deposition," p. 9).

Borehole breakouts observed during LWD confirm the transition from clay to claystone at ~304 to 316 mbsf (see "Logging While Drill-

F9. Glauconite and carbon-rich clay p. 49.

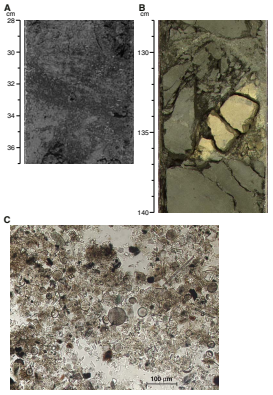

ing," p. 30, in "Downhole Logging"). Below 334 mbsf, borehole breakouts dominate the RAB images and affect the log data.

Rare bioturbation and mottled fabric, resulting from black (N3) sulfide precipitates, are present only in Sections 204-1251B-44X-4 to 46X-1 and observed as small patches in Sections 49X-2 to 49X-6. Macroscopic aggregates of sponge spicules are observed in Cores 204-1251B-49X to 50X. Clam-shell fragments are found in Cores 204-1251B-52X and 53X.

The upper part of lithostratigraphic Unit III (Sections 204-1251B-37X-1 to 43X-CC) is dominated by silty claystone. Based on smear slide analyses (major lithology), the silty claystone contains up to 5% sand and 30% silt (Fig. F2). The major components of the silty claystone, as determined by XRD analyses, are quartz, feldspar, muscovite, illite, other clay minerals, and calcite in varying amounts. The silty claystone, as well as the claystone deeper in the hole, is diatom bearing to diatom rich (Fig. F9C). The siliceous microfossil content steadily increases from the top of lithostratigraphic Unit III to ~20% diatoms at 328.4 mbsf (Fig. F3). The biogenic carbonate fraction, consisting of foraminifers and nannofossils, decreases (Fig. F3) proportionally. Below 401.79 mbsf, biogenic carbonate is absent from the sediments.

Glauconite appears not only at the top of lithostratigraphic Unit III (Fig. F9A) but is also dispersed through the whole unit. Glauconite is much more abundant in lithostratigraphic Unit III than in the overlying units, and its concentration in the sediments of Unit III increases with depth (Fig. F7A). The percentage of glauconite also increases in comparison to the other lithostratigraphic units (Figs. F7A, F9A). In lithostratigraphic Unit III, it composes up to 20% of the sediment in Sections 204-1251B-36X-4 through 36X-6, 37X-1, 46X-3, 47X-CC, 49X-1 through 49X-3, 49X-6, and 53X-3. In Sections 204-1251B-51X-1 through 51X-4, glauconite is a major lithology (e.g., glaucony).

In the lower part of lithostratigraphic Unit III (Sections 204-1251B-44X-1 through 53X-CC), the major lithology is claystone, containing up to 20% silt (Fig. F2). The major components of the claystone, as determined by XRD analyses, are similar to the composition of the silty claystone discussed above.

Substantial amounts of authigenic micritic carbonate were observed in lithostratigraphic Unit III as a minor, slightly indurated (or nonlithified) lithology (Fig. F9B). These carbonate-rich zones, which are observed in Cores 204-1251B-41X, 44X through 47X, 49X, 50X, and 52X, appear as olive-gray (5Y 5/2) to olive (5Y 5/3) patches between 1 and 60 cm thick. Clay-sized carbonate needles compose ~90% of the sediment components seen in smear slides. XRD analyses show a mixed calcite composition in Samples 204-1251B-41X-3, 18–19 cm, and 44X-6, 30–31 cm (Fig. F10). Chemical measurements of $CaCO_3$ (Fig. F7A) show that these are areas of high calcium carbonate content (Samples 204-1251B-41X-3, 18–19 cm [333.78 mbsf], 47X-5, 124–127 cm [394.5 mbsf], 49X-1, 86–90 cm [398.77 mbsf], and 50X-6, 53–55 cm [414.55 mbsf]). These samples have a $CaCO_3$ content of 17.6–50.4 wt%. For comparison, the estimated authigenic carbonate content in a nearby smear slide at 333.69 mbsf is ~80%.

The presence of carbonate nodules is characteristic of lithostratigraphic Unit III (Table T2). A distinction can be made between solid lithified nodules and semilithified nodules. Solid nodules are present at ~305.4 mbsf (Samples 204-1251B-37X-4, 30–32 cm, and 37X-4, 32–33 cm), 322.08 mbsf (Sample 204-1251B-39X-2, 68–69 cm), 336.12 mbsf (Sample 204-1251B-41X-4, 102–104 cm), and 427.12 mbsf (Sample 204-1251B-52X-1, 132–135 cm). The mineralogy of the solid carbonate sam-

F10. XRD records, p. 50.

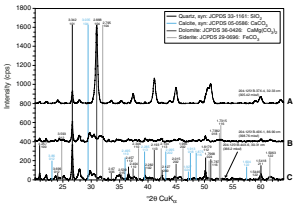

T2. Carbonate samples in lithostratigraphic Unit III, p. 95.

ples, determined by XRD analyses, varies. Samples 204-1251B-37X-4, 30–32 cm, and 37X-4, 32–33 cm, are of pure dolomitic composition (Fig. F10; Table T2). Sample 204-1251B-39X-2, 68–69 cm, shows calcitic and dolomitic carbonate phases, and Sample 204-1251B-52X-1, 132–135 cm (Fig. F10), is purely calcitic. Thin sections reveal a micritic matrix of dolomite, with 9% foraminifer tests, 5% opaque minerals, and 1% glauconite in Sample 204-1251B-37X-4, 31–32 cm. Sample 204-1251B-39X-2, 68–69 cm, shows a micritic matrix (calcite/dolomite?) as well, with only 3% foraminifers, 5% diatoms, 15% opaque minerals, 2% glauconite, and 3% quartz.

Semilithified nodules are present from 378.56 to 398.76 mbsf. Based on their d(104) spacings, Samples 204-1251B-46X-1, 96–98 cm, and 46X-CC, 7–9 cm, are of calcitic composition. Sample 204-1251B-47X-5, 121–126 cm, shows two different calcite phases, and Sample 204-1251B-49X-1, 86–90 cm, is composed of three different carbonate phases (Fig. F10) that are formed by substitution of calcium by major cations like iron, magnesium, and manganese in the crystal lattice.

Sedimentary Evidence of Gas Hydrate

The sediments of the eastern slope basin lack substantial textural evidence for the dissociation of gas hydrate. Mousselike textures were found in cores from Hole 1251B (Sections 204-1251B-10H-1 and 10H-5) and four cores from Hole 1251D (Sections 204-1251D-2X-1, 3X-1, 5X-1, and 18H-1). Thermal and chloride anomalies indicate hydrate may have been present in Cores 204-1251D-22X and 24X (see Fig. F20, p. 70, in the "Leg 204 Summary" chapter) just above the BSR, although no corresponding lithologic evidence was found.

Environment of Deposition

Site 1251 is located on the eastern flank of southern Hydrate Ridge. At this site, we recovered the stratigraphic sequence of the eastern slope basin (Fig. F5). The stratigraphy preserved in this slope basin environment is characterized by hemipelagic sedimentation and episodic coarse- and fine-grained turbidite and debris flow deposition.

Lithostratigraphic Unit III is composed of indurated scaly clay (claystone). Biostratigraphic analyses indicate an age between 2.0 and 1.6–1.0 Ma for this unit, which suggests an average sedimentation rate of ~33 cm/k.y. (see "Summary," p. 12, in "Biostratigraphy"). The presence of glauconite-rich intervals and authigenic carbonate nodules and cements (Figs. F7A, F9A, F9B) suggests that diagenetic processes are active throughout the unit. High values on the LWD gamma ray density data correlate with the presence of some of the glauconite layers, possibly resulting from the high K content of glauconite clay minerals.

Authigenic formation of green glauconite grains is documented by submarine weathering of phyllosillicates, which were modified as a result of an adequate supply of both potassium and iron from seawater. In general, glauconization forms a diagenetic sequence ranging from glauconitic smectite to glauconitic mica (Odin and Matter, 1981). Since glauconite contains both ferric and ferrous iron, its formation is limited to a specific level of oxidation potential close to the seafloor, which needs to be maintained over long timescales (1–1000 k.y.). These distinct glauconite layers often represent time intervals of very low or zero sediment accumulation and result in unconformities in the sediment sequence.

The 3-D seismic data suggest a major discontinuity exists at ~300 mbsf, between irregular, discontinuous, and chaotic reflections (lithostratigraphic Unit III) and well-stratified seismic reflectors (lithostratigraphic Unit II). Visual core descriptions, examinations of seismic reflection profiles, and the presence of borehole breakouts on LWD resistivity data all suggest that lithostratigraphic Unit III is part of the older accretionary complex of Hydrate Ridge.

Lithostratigraphic Unit II is composed of hemipelagic silty clays and clays ranging from ~1.0 to 0.3 Ma in age, yielding a sedimentation rate of ~17 cm/k.y. (see **"Summary,"** p. 12, in "Biostratigraphy"). In the 3-D seismic data, lithostratigraphic Unit II is characterized by a series of well-stratified east-dipping seismic reflectors. The reflectivity changes from low above the BSR to high below the BSR, delimiting the boundary between a possible free gas zone beneath the BSR and gas hydrate–bearing region above. Hydrate was sampled from Unit II near the BSR (190 mbsf) and is associated locally with coarse-grained sediments (Figs. **F2, F4**).

Lithostratigraphic Subunit IIB is clay dominated and characterized by the highest abundance of calcareous microfossils at Site 1251 (Fig. **F3**). The homogeneous fine-grained sediments and lack of significant iron sulfides within lithostratigraphic Subunit IIB correlate well with the uniform low signature of MS data (Fig. **F4**) (see **"Magnetic Susceptibility,"** p. 22, in "Physical Properties"). Because lithostratigraphic Subunit IIA contains few sand and silt turbidites, a distinct abundance of iron sulfide material (pyrrhotite) may help explain the large excursions recorded in MS data (see **"Magnetic Susceptibility,"** p. 22, in "Physical Properties").

The boundary between lithostratigraphic Units II and I corresponds to a major angular unconformity at ~130 mbsf best seen in the 3-D seismic data (Fig. **F5**). This discontinuity, however, is not obvious in the recovered core from Site 1251 because the lithologies of lithostratigraphic Subunit IC are similar to those of Unit II and bedding planes and attitudes are difficult to identify in the stratigraphy. Nevertheless, there is a noticeable lack of the large MS excursions in Subunit IC (Fig. **F2**). Lithostratigraphic Subunit IC is also characterized by the onset of pelagic sediment components, including diatoms, foraminifers, and nannofossils, and an abrupt decrease in terrigenous coarse components (Figs. **F2, F3**). An observed decrease in sedimentation rate may be consistent with this style of sedimentation (see **"Summary,"** p. 12, in "Biostratigraphy"). In the 3-D seismic data, Unit III corresponds to a 100-m-thick sequence characterized by subparallel, well-stratified, and slightly folded seismic reflectors (Fig. **F5**).

Lithostratigraphic Subunit IB is composed of large unsorted clasts of heterogeneous compositions and convolute bedding, suggestive of debris flow deposition. The lithology of this subunit correlates with a large positive peak (up to 100 SI units) in the MS data (see **"Magnetic Susceptibility,"** p. 22, in "Physical Properties"). In the 3-D seismic data, lithostratigraphic Subunit IB is characterized as a lens-shaped sediment package with a chaotic internal reflection pattern and an erosional base. This depostional unit reaches a thickness of up to 70 m at the center of the eastern basin (Fig. **F5**) and covers an area ~2.5 km wide × 8 km long. Similar deposits are observed on the Mediterranean margin and are interpreted to have resulted from slope instability initiated by the sea level lowstand during the late Pleistocene (Rothwell et al., 1998). Perhaps the sediments of lithostratigraphic Subunit IB have a similar origin.

Lithostratigraphic Subunit IA is composed of a series of turbidite deposits that increase in frequency and size downhole. Fine-grained, low-frequency turbidites are present within the upper 11 mbsf of this subunit, whereas coarser and larger events dominate the lower part. An increase in siliceous microfossil abundance in the upper part of lithostratigraphic Subunit IA (Fig. F4) may represent the late Pleistocene/Holocene boundary, as documented in several cores throughout the northern and central Cascadia margin (Duncan et al., 1970).

BIOSTRATIGRAPHY

Seven holes were drilled at Site 1251. Of these holes, Hole 1251B contains the most complete sequence, a 445-m-thick upper Pliocene–Quaternary sedimentary sequence. Biostratigraphy for Site 1251 was based on examination of all core catcher samples and a few of the samples within cores from Hole 1251B.

Diatoms

The abundance and preservation of diatoms in sediments from Hole 1251B varies significantly, indicating possible variations in ocean productivity and/or dilution by nonsiliceous biogenic and clastic components. Diatoms are few to abundant and poorly to well preserved in the interval from 0 to 120 mbsf and from 320 mbsf to the bottom of the hole. Diatoms are rare or absent in the interval from 120 to 320 mbsf, except for Samples 204-1251B-19H-CC (163.6 mbsf), 27X-CC (222.8 mbsf), and 31X-CC (258.3 mbsf), where diatoms are common. Diatom assemblages from Hole 1251B are dominated by species of the subarctic North Pacific Ocean. A few warm-water taxa, such as *Hemidiscus cuneiformis* and *Fragilariopsis doliolus,* are sporadically present. Neritic species, such as *Actinoptychus senarius* and *Cocconeis* spp., are present in most samples, whereas freshwater species, such as *Aulacoseira* spp., are present sporadically.

The interval between the top of Hole 1251B and Sample 204-1251B-19H-CC (0–163.6 mbsf) contains *Neodenticula seminae* but lacks *Proboscia curvirostris.* This interval is assigned to North Pacific Diatom Zone (NPD) 12 (*N. seminae* Zone). The last occurrence (LO) of *P. curvirostris* was found in Sample 204-1251B-20H-CC (171.7 mbsf), whereas the LO of *Actinocyclus oculatus* was found in Sample 39X-6, 57–59 cm (328.0 mbsf). The interval between these two LOs (171.7–28.0 mbsf) is assigned to NPD 11 (*P. curvirostris* Zone). The interval between Samples 204-1251B-39X-6, 57–59 cm, and 52X-CC (328.0–434.7 mbsf) contains *A. oculatus* but lacks *Neodenticula koizumii* and is assigned to NPD 10 (*A. oculatus* zone). The first occurrence (FO) of *P. curvirostris* was found in Sample 204-1251B-42X-CC (348.4 mbsf). The LO of *N. koizumii* was found in Sample 204-1251B-53X-2, 64–66 (437.6 mbsf), indicating an age of ~2.0 Ma for the bottom of Hole 1251B 5 m below this event. The interval between the LO of *N. koizumii* and the bottom of Hole 1251B contains *N. koizumii* and *N. seminae* but lacks *Neodenticula kamtschatica.* It was assigned to the upper part of NPD 9 (*N. koizumii* Zone).

Calcareous Nannofossils

Calcareous nannofossils from Hole 1251B were investigated in smear slides from core catcher samples and from selected within-core samples

to better constrain the biohorizons. Hole 1251B yielded common to rare, well- to moderately preserved nannofossils in Holocene–Pliocene sections.

Emiliania huxleyi is continuously present from the top of Hole 1251B down to Sample 204-1251B-19H-1, 74–76 cm (156.3 mbsf), assigning this interval to Zone NN21. Abundant *E. huxleyi* was observed in Sample 204-1251B-1H-CC (9.0 mbsf). The abundance decreases distinctly in the next Sample 204-1251B-3H-CC, allowing us to assign Sample 1H-CC to the *E. huxleyi* Acme Zone. The interval between Samples 204-1251B-19H-CC and 24X-CC (between 163.6 and 189.0 mbsf) contains abundant *Gephyrocapsa* spp. but lacks *E. huxleyi* and *Pseudoemiliania lacunosa;* this interval was assigned to Zone NN20. The presence of *P. lacunosa* in Sample 204-1251B-25X-CC (204.1 mbsf) marks the NN19b/NN20 zonal boundary. Various small *Gephyrocapsa* spp. are abundant in Samples 204-1251B-33X-CC and 34X-CC (280.5–289.1 mbsf). This interval was assigned to the mid-Pleistocene small *Gephyrocapsa* spp. Acme Zone (1.0–1.2 Ma). The LO of *Calcidiscus macintyrei* was found in Sample 204-1251B-34X-CC (289.1 mbsf), indicating an age of 1.59 Ma (NN19) for this stratigraphic level. *Gephyrocapsa lumina* is present in Sample 204-1251B-38X-4, 66–68 cm (315.5 mbsf), suggesting an age of 1.67 Ma.

Based on calcareous nannofossils, the Pliocene/Pleistocene boundary (1.77 Ma) (Berggren et al., 1995) is located below the FO of medium-sized *Gephyrocapsa* spp. (>4 µm). The FO of a few medium-sized *Gephyrocapsa* spp. was observed in Sample 204-1251B-45X-3, 66–68 cm (371.7 mbsf), indicating this sample is of Quaternary age. The interval from Samples 204-1251B-45X-CC to 53X-CC (378–443 mbsf) does not contain any Pliocene bioevent marker species; for example, there are no species of genus *Discoaster,* which are warm-water species and absent in high latitudes and cold-current regions. However, this interval contains a calcareous nannofossil assemblage with abundant *Reticulofenestra productus* and *P. lacunosa,* whereas the early Pliocene event marker *Reticulofenestra pseudoumbilicus* is absent. This evidence suggests that the lowest sequence of 378–443 mbsf in Hole 1251B is of late Pliocene age.

Summary

Sediments recovered at Site 1251 yielded few to abundant diatoms and rare to common calcareous nannofossils in most samples examined. A total of eleven microfossil events (four diatom and seven nannofossil events) was recognized at Site 1251 (Table **T3**). An age-depth plot shows that biohorizons from the two fossil groups generally agree (Fig. **F11**). The Pleistocene/Pliocene boundary is estimated by the FO of medium *Gephyrocapsa* spp. and is located between 371 and 377 mbsf.

The linear sedimentation rates at Site 1251 have been calculated based on biostratigraphic data (Table **T3**) and are estimated to be 60 cm/k.y. for the interval from the top of Hole 1251B to 170 mbsf, 17 cm/k.y. for the interval from 170 to 290 mbsf, 3 cm/k.y. for the interval from 290 to 310 mbsf, and 33 cm/k.y. for the interval from 310 mbsf to the bottom of Hole 1251B (Fig. **F11**). According to seismic data, a regional unconformity is located at about 130 mbsf at Site 1251. An alternative sedimentation rate is estimated for the interval from the top of Hole 1251B to 130 mbsf by putting an inflexion point at 130 mbsf, the depth of the unconformity. In this case, the sedimentation rate above 130 mbsf is 160 cm/k.y. (Fig. **F11**). In conclusion, sedimentation rates

T3. Bioevents, p. 96.

F11. Age-depth plot, p. 51.

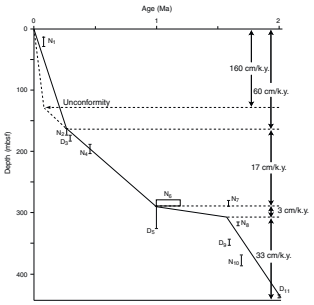

are very high in the two intervals from the top of Hole 1251B to 170 (or 130) mbsf and from 310 mbsf to the bottom of Hole 1251B.

INTERSTITIAL WATER GEOCHEMISTRY

A total of 115 whole-round samples were collected for pore water analyses at Site 1251 (70 samples from Hole 1251B, 4 samples from Hole 1251C, 32 samples from Hole 1251D, and 8 samples from Hole 1251E). Routine samples were collected at a frequency of approximately two whole-round samples per core in the upper 200–225 mbsf, followed by a sampling rate of one whole-round sample per core below these depths. A higher-resolution sampling protocol was used within the anaerobic methane oxidation (AMO) zone in Hole 1251E, where sampling occurred at a frequency of two whole-round samples per section in a coordinated program with the shipboard microbiologists. Interstitial water (IW) geochemistry data are tabulated in Table **T4** and are illustrated in Figure **F12.**

Chloride Concentration and the Presence of Gas Hydrate

The distribution of dissolved chloride at Site 1251, shown in Figure **F12,** displays an approximately linear decrease with depth at a rate of ~0.46 mM/m to ~300 mbsf with deviations that might be related to gas hydrate dynamics. Similar decreases were observed at other sites drilled on the Cascadia margin (see **"Interstitial Water Geochemistry,"** p. 13, in the "Site 1244" chapter) (also see Kastner et al., 1995) and probably reflect diffusion of chloride ions from present-day seawater values to the low-chlorinity fluids that characterize the accreted sediments below 300 mbsf. The onset of low-chloride fluids observed between 300 and 310 mbsf corresponds to a seismic reflector that might image the top of the accreted sedimentary wedge (see **"Introduction,"** p. 1). This horizon also corresponds to the top of lithostratigraphic Unit III (see **"Lithostratigraphic Unit III,"** p. 7, in "Lithostratigraphic Units" in "Lithostratigraphy") and the onset of borehole breakouts in the LWD data (see **"Logging While Drilling,"** p. 30, in "Downhole Logging"). As discussed for Site 1244, the chloride decrease in the IW at Site 1251 corresponds to an increase in dissolved lithium (Fig. **F13**), suggesting a fluid source deeper than 1 km. This inference is similar to the interpretation based on IW data from Sites 889 and 890 on the Cascadia margin off Vancouver Island (Kastner et al., 1995). At Site 1251, the deep-seated fluids have chloride concentrations of 435 mM. Similarly, the dissolved chloride in the lower sections of Hole 1244C averaged 472 mM (see **"Interstitial Water Geochemistry,"** p. 13, in the "Site 1244" chapter). In contrast, the deep fluids at Sites 889 and 890 have an average concentration of 370 mM (Fig. **F14**). The difference might reflect variations in the composition of the sediments and/or variations in the depth to which accreted sediments have been buried.

The dissolved chloride distribution in the sediments above the BSR is different from all the other sites drilled during Leg 204. The other sites all show repeated excursions to low chloride values throughout much of the GHSZ. In contrast, at Site 1251, we only observe a significant chloride anomaly just above the BSR, indicating that significant amounts of gas hydrate are present only near the base of the GHSZ, with very little gas hydrate present in the sediments above. Drilling in

T4. Dissolved species in pore waters, p. 97.

F12. Concentration profiles of various dissolved species, p. 52.

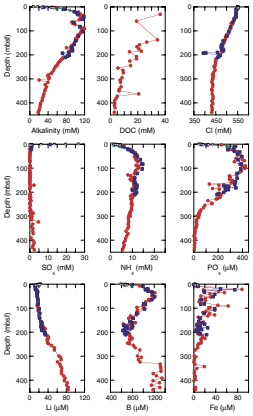

F13. Distribution of dissolved chloride and lithium, p. 54

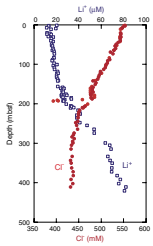

F14. Chloride distribution, p. 55.

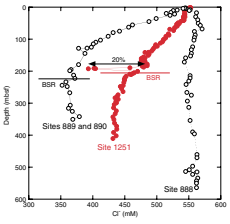

Hole 1251B had no recovery of gas hydrate near the BSR (see "Operations," p. 2), and no hydrates were identified by the chloride data above or below the BSR in Hole 1251B (Fig. F14). However, the second attempt to drill through the BSR at this site recovered Core 204-1251D-24X, whose infrared (IR) temperature data indicated the presence of gas hydrate throughout the core (see "Physical Properties," p. 19). The four IW samples taken from Core 204-1251-24X (Table T4) all show chloride anomalies indicating the presence of gas hydrate (Fig. F14). Larger anomalies were observed in Sections 204-1251D-24X-3 and 24X-4 and correspond to gas hydrate occupying ~20% of the pore space.

Sulfate, Methane, and the Sulfate/Methane Interface

The clearest record of the sulfate gradient and the position of the sulfate/methane interface (SMI) comes from Hole 1251E (for a general discussion on the SMI see "Interstitial Water Geochemistry," p. 13, in the "Site 1244" chapter). Here, the SMI is located at ~4.5 mbsf (Fig. F15), where interstitial sulfate first reaches a minimum concentration concomitant with increasing methane concentration as documented by headspace gas data from Hole 1251C (see "Organic Geochemistry," p. 16,). The zone where AMO occurs was sampled extensively by the microbiology team at this site (see "Microbiology," p. 18). The sulfate profile is approximately linear between 1.5 and 4.5, with curvature at the top and bottom of the profile that probably reflects oxidation of sedimentary organic matter by sulfate and/or fluid advection processes.

F15. Sulfate and methane concentration profile, p. 56.

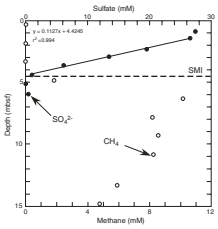

Following the method developed by Borowski et al. (1996) and outlined at Site 1244 (see "Interstitial Water Geochemistry," p. 13, in the "Site 1244" chapter), the estimated methane flux at Site 1251 is 5.5×10^{-3} mM/cm²/yr, based on a sulfate gradient of 8.8 mM/m (estimated from the linear portion of the curve) (see Fig. F15), a sulfate diffusion coefficient of 5.8×10^{-6} cm²/s at 5°C, and an average porosity of 0.70%. For comparison, the estimated methane flux at Site 1251 is about twice that calculated for Site 1244 and about three times larger than that estimated at the Blake Ridge, a large passive-margin gas hydrate terrain. These estimates assume methane delivery through diffusion only and that the linear portion of the sulfate curve is mainly created by sulfate demand at the SMI. If significant advection of water or free gas occurs or if sulfate depletion through AMO is of minor importance, then this estimate is invalid.

Organic Matter Decomposition

The early diagenesis of marine sediments is often dominated by organic matter decomposition (e.g., Berner, 1980). Interstitial alkalinity (a proxy for total dissolved CO_2) (ΣCO_2), ammonium (NH_4^+), and phosphate (PO_4^{3-}) concentrations increase with increasing depth, reaching maximum concentrations at ~40, ~80, and ~100 mbsf, respectively (Table T4; Fig. F12). From the shape of the profiles, it is likely that the microbial decomposition of sedimentary organic matter is most active in the upper 100 mbsf of the sedimentary section. During postcruise shore-based research, we will have the opportunity to correlate microbial abundance and activity to key interstitial constituents that identify organic matter decomposition.

The alkalinity profile at Site 1251 is curious in that an anomalous deflection toward lower values occurs between 50 and 90 mbsf (Table T4;

Fig. F12). This decrease in alkalinity is not an artifact because data from Holes 1251B and 1251D show the same pattern. Localized decreases in interstitial concentrations of CO_2 are often a result of authigenic carbonate formation. However, there is no macroscopic evidence for authigenic carbonate precipitation in this portion of the stratigraphic sequence, and sediment carbonate content is not elevated in the zone of lowered alkalinity (see "Lithostratigraphy," p. 3). Detailed shore-based sampling and microscopic and chemical analyses may resolve the question.

Major and Minor Element Distributions

The distribution of the dissolved ions in pore fluids often (Fig. F12; Table T4) provides clues on the nature of the fluid sources, diagenetic reactions, and microbiological processes within these sediments. We will discuss the pore water distributions in lithostratigraphic Units I and II, followed by changes observed in lithostratigraphic Unit III (see "Lithostratigraphic Unit III," p. 7, in "Lithostratigraphic Units" in "Lithostratigraphy").

The increase in dissolved barium to 75 µM following depletion of dissolved sulfate at 4.5 mbsf follows the general trend described at other Leg 204 sites (Fig. F16). The overall increase in dissolved boron in the upper 40 mbsf (Fig. F12), similar to that observed at Site 1244, may be related to carbonate diagenesis (e.g., Deyhle et al., 2001), as evidenced by the similarity between alkalinity and boron distributions. As described for Site 1244, the transformation of aragonite to calcite may release boron and magnesium into the IW. Such a process has been documented by laboratory studies (Kitano et al., 1978) and by boron distribution in carbonate phases (Deyhle et al., 2001). Although the upper 23 mbsf show low dissolved iron content, the sediments between 23 and 130 mbsf show tremendous variability in the dissolved iron values in both Holes 1251A and 1251B. This section of high iron concentrations corresponds to lithostratigraphic Subunits IA, IB, and IIA, which are all characterized by the presence of abundant sulfide minerals (Fig. F17). The onset of high iron in the pore fluids corresponds to the top of a debris flow deposit (see "Lithostratigraphy," p. 3) and a large excursion in the MS data (see "Magnetic Susceptibility," p. 22, in "Physical Properties"). Recycling of iron below the depth of sulfide depletion is likely to be responsible for the observed iron distribution.

The increase in lithium and strontium within the deep accreted sediments of lithostratigraphic Unit III reflects release of these ions from aluminosilicates at depth, as discussed for Site 1244 (see "Interstitial Water Geochemistry," p. 13, in the "Site 1244" chapter). This zone is similar in composition to that reported for Sites 889 and 890 in the northern section of the accretionary prism (Kastner et al., 1995). In addition to high lithium and strontium, the sediments corresponding to lithostratigraphic Unit III (see "Lithostratigraphic Unit III," p. 7, in "Lithostratigraphic Units" in "Lithostratigraphy") show a marked change in the dissolved barium and boron content. Particularly striking at Site 1251 is the sharp increase in dissolved boron in the pore fluids of accreted sediments below 315 mbsf. These high levels (~1.3 mM) result from the loss of boron from aluminosilicate minerals during the accretion of sediments. Tectonically expelled waters in subduction zones have been shown to have elevated boron contents (up to 2 mM), and their distribution and isotopic composition have proven useful in elucidating fluid processes in these environments (You et al., 1996; Spivack

F16. Dissolved sulfate and barium profiles, p. 57.

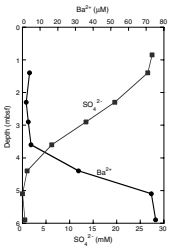

F17. Downcore variations in MS, p. 58.

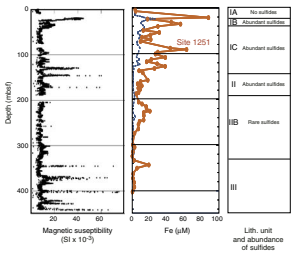

and You, 1997). The drastic increase in dissolved boron at Site 1251 likely demarks the contact with the accreted sediments at this site.

ORGANIC GEOCHEMISTRY

Site 1251 is located in a slope basin in a contrasting environment to sites on or near Hydrate Ridge. The shipboard organic geochemistry program at Site 1251 included analyses of hydrocarbon gases, carbonate and organic carbon (OC), as well as total sulfur and total nitrogen content. A description of the methods used for these analyses is summarized in "Organic Geochemistry," p. 16, in the "Explanatory Notes" chapter.

Hydrocarbon Gases

The levels of methane (C_1), ethane (C_2), ethylene ($C_{2=}$), and propane (C_3) remaining in cores were measured using the headspace technique. The results are reported in Table T5 and plotted as parts per million by volume (ppmv) of gas component vs. depth in Figure F18. Methane content increases rapidly from levels of 48–178 ppmv in the shallowest samples at 0–3 mbsf to ~40,000–60,000 ppmv at ~6 mbsf and below. In addition to the ppmv concentrations of hydrocarbons in the vial headspace, the C_1 values have been recalculated to express the millimoles of methane remaining in the cores per liter of pore water. These estimates of absolute gas concentration are meaningful only in shallow zones where sediments are undersaturated or slightly supersaturated with respect to dissolved methane. The calculated dissolved CH_4 concentration is shown in Figure F19, along with the sulfate depletion profile illustrating the depth of the SMI. Sample depths in the upper part of Hole 1251B have been increased by an empirically determined constant amount (3.7 m) only for purposes of plotting in Figure F19. The methane content vs. depth curves for the upper part of Holes 1251B and 1251C coincide after the depths in Hole 1251B are adjusted downward. Apparently, the first core in Hole 1251B did not recover the SMI.

Ethane content is low (1–2 ppmv or below detection levels) in headspace analyses of cores from Site 1251 in the depth interval from the seafloor to 195 mbsf. Ethylene is sporadically present at trace levels (0.3–2 ppmv) throughout the depth interval cored, whereas propane traces are present in headspace gas only for samples below depths of 313 mbsf (Table T5; Fig. F18).

The compositions of gas samples from voids or expansion gaps in the core liner are listed in Table T6 and plotted in Figure F20. The void gas (vacutainer [VAC]) samples are relatively pure methane, generally with minimal air contamination. Contents of methane in the voids from Hole 1251B are generally >900,000 ppmv (>90% by volume), unless diluted by air. Ethane content of void gas shows a gradual increase with depth, from 3 ppmv near the seafloor to a range of 7–33 ppmv in the interval from 85 to 185 mbsf just above the BSR. Beneath the BSR, the ethane content increases abruptly to a range of 200–300 ppmv. This order-of-magnitude increase in the relative ethane content just below the BSR is also apparent in the headspace gas analyses. These trends may be related to the formation and decomposition of gas hydrate, but the exact mechanism producing this relative ethane enrichment is still being investigated. Propane contents range from 3 to 26 ppmv, with no apparent relationship to depth or the base of GHSZ (Table T6; Fig. F20).

T5. Methane, ethane, and propane in HS samples, p. 100.

F18. C_1, C_2, $C_{2=}$, and C_3, p. 59.

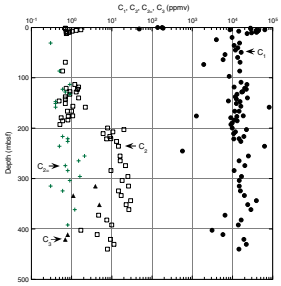

F19. Dissolved residual methane and sulfate, p. 60.

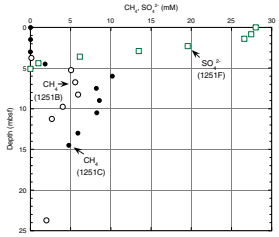

T6. Light hydrocarbon and nonhydrocarbon gases in VAC samples, p. 102.

F20. Light hydrocarbons vs. depth, p. 61.

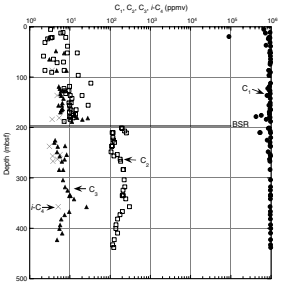

Gas composition expressed as the C_1/C_2 ratio of headspace and void gas is plotted vs. depth in Figure F21. The C_1/C_2 ratios for both headspace and void gas do not show any systematic decrease, other than the marked offset discussed above due to an increase in ethane content in sediments beneath the BSR.

F21. C_1/C_2 ratio vs. depth, p. 62.

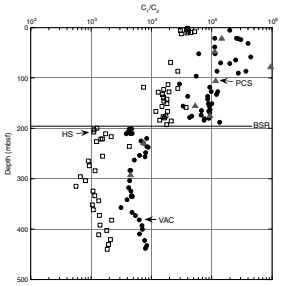

Gas Hydrate and Pressure Cores

No gas hydrate pieces or gas hydrate–bearing sediments were physically recovered from cores on the catwalk although several Cl^- and IR anomalies were detected (see "Physical Properties," p. 19, and "Interstitial Water Geochemistry," p. 13). Eight deployments of the PCS successfully retrieved full (1 m) cores from depths of 20–291 mbsf. Two of these (Cores 204-1251D-6P and 204-1251B-12P) contained sufficient gas to confirm a subsurface presence of methane hydrate (see "Downhole Tools and Pressure Coring," p. 25). The compositions of gas samples obtained during controlled PCS degassing experiments are listed in Table T7. The C_1/C_2 ratios for gas from all but one of the PCS cores (based on volume-averaged composition) fall on the vacutainer/void gas trend (Fig. F20), confirming that gases exsolved in the core liner are a valid representation of subsurface hydrocarbon composition. Gas from PCS Core 204-1251D-10P at 76.4 mbsf is almost totally lacking in ethane and appears to be from sediment that is undersaturated with respect to methane hydrate. Gas from this sample may reflect ethane depletion in the pore water, which is a possible consequence of the ethane enrichment (theoretically) occurring in the gas hydrates.

T7. Gas composition of samples from PCS experiments, p. 104.

Carbon Analyses, Elemental Analyses, and Rock-Eval Characterization

A total of 39 sediment samples (one per core except for special tool cores) were analyzed for carbonate carbon (IC), total carbon (TC), OC (by difference), total nitrogen (TN), and total sulfur (TS). The results are listed in Table T8. IC, plotted against depth of burial in Figure F22, varies from 0.04 to 2.19 wt%. Concentrations of IC are relatively high at 255.78, 284.68, and 333.78 mbsf. When calculated as $CaCO_3$, the IC in Hole 1251B sediments varies from 0.3 to 18.27 wt% (Fig. F22). Samples from depths of 255.8, 284.7, and 333.8 mbsf contain >15 wt% $CaCO_3$. The upper two $CaCO_3$-enriched samples are from a depth interval in Hole 1251B that contains up to 50% biogenic carbonate (see "Lithostratigraphy," p. 3). The lower sample is probably authigenic carbonate. The sediments below 350 mbsf generally contain relatively low amounts of carbonate carbon.

T8. IC, OC, TN, TS, and C/N ratios, p. 106.

F22. IC, OC, TN, and TS and C/N ratios, p. 63.

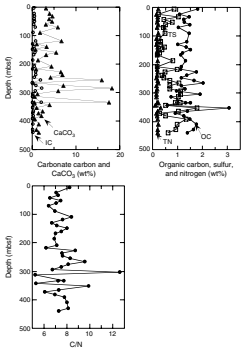

Organic carbon content varies from 0.58 to 3.06 wt% (average = 1.37 wt%) (Table T8; Fig. F22). The analyzed sample with the highest OC content is at a depth of 352.48 mbsf, where the C/N ratio approaches a value of 10, possibly resulting from the input of terrestrial organic matter. The C/N ratios of the other samples are generally <10, suggesting that input of marine organic matter was dominant during deposition. An exception is the sample at 304 mbsf, which also is relatively enriched in OC at 1.87 wt%. For the most part, C/N ratio varies according to the content of OC in the sediment because the concentration of TN is relatively uniform throughout the section. Total nitrogen in the sediments varies consistently between 0.11 and 0.22 wt% (Table T8; Fig. F22), with no apparent trends with either depth or OC content.

Sediment samples have total sulfur contents ranging from 0.17 to 1.77 wt% (Table T8), with the amount of sulfur roughly proportional to OC content. A plot of sulfur vs. carbon (not shown) for Site 1251 sediments has a linear relationship with a slope of 0.5. This type of plot has traditionally been used to estimate the fraction of deposited OC oxidized during sulfate reduction (Goldhaber and Kaplan, 1974; p. 601). Typical marine sediments have sulfur to OC ratios of 0.36, which suggest that ~20% of the deposited OC was oxidized during sulfate reduction. The ratio of 0.5 for Site 1251 sediments would suggest that >40% of the OC was oxidized during sulfate reduction (i.e., there is excess sulfur present for the amount of preserved OC). However, the assumptions underlying the use of the sulfur/organic carbon ratio do not include the possibility of sulfate reduction coupled with AMO. Probably the apparent excess of sulfur in Site 1251 sediments is due to the fact that a significant component of the sulfur is derived from sulfate reduced in connection with methane oxidation.

The results of Rock-Eval pyrolysis of selected samples are given in Table T9. This analysis was performed in part to evaluate the possible presence of migrated liquid hydrocarbons. Although the production index values seem moderately elevated (i.e., >0.1), they are fairly typical for continental margin sediments cored by ODP. There is no correlation between increased C_{2+} gas components and higher production index values and no definitive evidence for oil staining.

T9. Rock-Eval pyrolysis, p. 107.

MICROBIOLOGY

Introduction

Site 1251, located in a slope basin to the east of Hydrate Ridge, was a main target site for microbiological study, as it provides a contrast to the ridge summit (Sites 1249 and 1250). Compared to the summit sites, hydrates and thermal anomalies were rare at Site 1251 (see **"Infrared Scanner,"** p. 20, in "Physical Properties") and the SMI was easily discernible in the sediment column (see **"Sulfate, Methane, and the Sulfate/Methane Interface,"** p. 14, in "Interstitial Water Geochemistry").

Microbiological Sampling

Collecting sediments at the SMI, which was estimated at ~4.5 mbsf from methane (see **"Hydrocarbon Gases,"** p. 16, in "Organic Geochemistry") and sulfate (see **"Sulfate, Methane, and the Sulfate/Methane Interface,"** p. 14, in "Interstitial Water Geochemistry") concentrations, was a prime objective at Site 1251. Site 1251 also has a more rapid sedimentation rate (see **"Summary,"** p. 12, in "Biostratigraphy") than the other sites sampled for microbiological purposes (Sites 1244 and 1245). This different depositional environment may change the microbial habitat.

Although the methane flux is estimated to be larger than that at Sites 1244–1247 (see **"Hydrocarbon Gases,"** p. 16, in "Organic Geochemistry"), hydrates were not abundant and the only significant IR thermal anomalies encountered were directly above the BSR (see **"Infrared Scanner,"** p. 20, in "Physical Properties"). IR images will be correlated with microbiological samples to determine the possible influence of hydrate on sediments sampled.

The depth of penetration makes this an interesting site at which to study methanogenesis. Below the base of the GHSZ at Site 1251, methane is often undersaturated in pore fluids (see "Hydrocarbon Gases," p. 16, in "Organic Geochemistry"), providing a more favorable environment for methanogenesis.

Intervals sampled for microbiology are summarized in Table T10.

T10. Intervals sampled for microbiology, p. 108.

Core Quality Assessment

Perfluorocarbon Tracer

PFT concentrations shown in Table T11 are low both on the inside and outside of the core. Although samples from the inside of the core show a hundred-fold reduction in PFT compared to the outer layers, all concentrations are extremely low and probably reflect loss from sampling vials. Samples were not analyzed until much later in the cruise, and the perfluorocarbon is extremely volatile.

T11. Core quality indicators, p. 109.

Fluorescent Microspheres

A comparison of fluorescent microsphere penetration in core interiors and exteriors is summarized in Table T11. Most deployments of microspheres were successful (i.e., the Whirl-Pak bag broke). Microscopic analysis of outer core layers showed numbers of microspheres ranging upward from 10^4/g of sediment, whereas microspheres were generally below the detection limit of 10/g of sediment in the interior of the core.

Shallow Marine Biosphere

When Section 204-1251B-1H-1 was split, sedimentologists noticed a peachy orange gelatinous material within a fracture in the sediment at 47–48 cm. Wet-mount fluorescence (Fig. F23) and transmitted-light microscopy revealed an apparent monoculture of coccoid cells, often clumped in tetrads. These cells did not autofluoresce. Samples were preserved for deoxyribonucleic acid extraction.

F23. DAPI-stained "slime," p. 64.

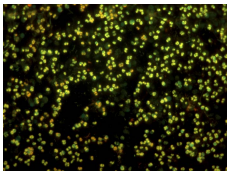

PHYSICAL PROPERTIES

In this section, we describe the downhole distribution of physical property data collected from Site 1251. Site 1251 is located in the basin to the east of the southern summit of Hydrate Ridge. Samples from three holes (Holes 1251B–1251D) drilled at this site were used to make physical property measurements. Holes 1251E–1251G were devoted to special microbiology and high-resolution turbidite studies, and no physical property measurements were performed on the cores from these holes. LWD data were available from Hole 1251A.

Routine physical property measurements were collected on whole-round core sections (see "Physical Properties," p. 22, in the "Explanatory Notes" chapter). A scan of IR emission along the entire core-liner surface was recorded for most cores at this site prior to sectioning and sampling on the catwalk. Special comparisons of IR scans between Holes 1251B and 1251D were performed to study the effects of different coring techniques (APC vs. XCB) on core temperatures.

Samples were taken from split cores to measure moisture and density (MAD). Compressional (*P*)-wave velocities (V_P) were not measurable at

this site because of gas expansion, with the exception of the upper 50 cm of Core 204-1251B-1H. Shear strength was measured with the hand-held Torvane on selected core sections to a depth of 180 mbsf.

The sampling for MAD at this site was mainly from Hole 1251B. For those depth intervals in Hole 1251B where core recovery was low or special tools were used, MAD samples were collected from Hole 1251D to fill the sampling gaps.

Measurement spacing, count times, and data acquisition schemes (DAQs) used for the multisensor track (MST) were the following: MS: spacing = 2.5 cm, count time = 3 × 1 s; gamma ray attenuation (GRA): spacing = 2.5 cm, count time = 5 s; *P*-wave logger (PWL): spacing = 2.5 cm, DAQ = 50. At this site, the Non Contact Resistivity (NCR) system was fully operational and was used in Holes 1251B and 1251D. A calibration was run for the NCR system to convert uncalibrated conductivity into resistivity of several standards of seawater with varying salinity (see **"Physical Properties,"** p. 22, in the "Explanatory Notes" chapter).

Infrared Scanner

IR imaging of cores drilled at Site 1251 provided identification on the catwalk of hydrate zones in each core. This information was used to facilitate hydrate sampling and preservation for all cores from this site. Thermal images suggest that most of the hydrate observed at this site is present as disseminated layers or zones, except for a major hydrate zone with interlayed sediment in Hole 1251D from 190 to 202 mbsf (near the BSR). An example of a typical hydrate thermal anomaly is shown in Figure **F24.** The IR thermal anomalies from this site are cataloged in Table **T12,** including an interpretation of the overall hydrate shape.

Successive thermal images were used to produce a downcore thermal profile for Holes 1251B and 1251D (Fig. **F25**). The profiles show the overall thermal structure of each core. The dominant features of the profiles are similar to those described for Site 1244, except for the zone of high hydrate abundance noted above. The downcore temperature profiles also include artifacts such as large positive anomalies caused by sun illumination and overall temperature trends that are caused by daily ambient temperature changes on the catwalk. Calibration data, to eliminate the atmospheric and ambient temperature effects, have been collected and will be applied during later data analysis. The artifacts are spatially limited or they create systematic differences in background temperatures that did not impact the identification of hydrates on the catwalk. The detailed analysis of hydrate thermal anomalies for estimating the concentration of hydrate in the subsurface was not affected. The temperature anomalies created by hydrate have been extracted from the downcore temperature data and from direct examination of IR images. Results are displayed graphically in Figure **F26** and demonstrate the overall low abundance of hydrate at this site, which is broadly consistent with pore water saturation (S_w) from the LWD data (see Fig. **F46**). Comparison of the thermal anomalies from Holes 1251B and 1251D (24.3 m apart) shows that hydrate zones match in general, but specific zones do not correlate between the holes. Comparison of S_w (Hole 1251A) with thermal anomalies shows a lack of exact depth correlation. Possible reasons for the lack of detailed correlation include (1) hydrate zones that are not stratigraphically controlled, (2) stratigraphically controlled zones that are laterally discontinuous, or (3) uncertainty in core depth due to poor core recovery. Note that the ~12-m-thick hydrate zone near the BSR in Hole 1251D was not detected in Hole 1251B,

F24. Cold-spot anomalies, p. 65.

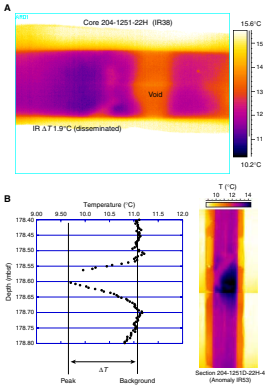

T12. Gas hydrate, p. 110.

F25. Downcore temperatures, p. 66.

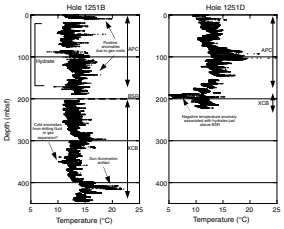

F26. Negative temperature anomalies, p. 67.

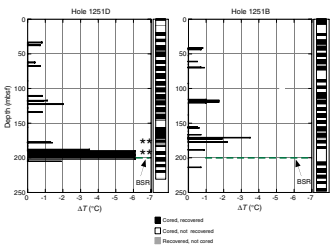

where there was nearly zero recovery at the equivalent depth. We suspect but cannot be certain that a thick zone was actually present in Hole 1251B and was not recovered. S_w from LWD resisitivity data (Hole 1251A) does show hydrate present over the depth intervals 187–197 and 202–205 mbsf but not with a response consistent with the thermal response in Hole 1251D. There is clearly significant hydrate near the BSR in Holes 1251A and 1251D and possibly in Hole 1251B, but it is likely that there is also significant lateral heterogeneity in hydrate concentration on a scale of ~25 m. This is important because the presence of a 10-m-thick zone of hydrate near the BSR is a significant contribution to the total volume of gas hydrate estimated for slope basins.

The absence of negative thermal anomalies below ~205 mbsf in Hole 1251D is consistent with the BSR depth and measured in situ thermal profile (see **"Downhole Tools and Pressure Coring,"** p. 25) at this site. Minor cold anomalies are present at 213.8 and 350.1 mbsf in Hole 1251B (Anomalies 204-1251B-IR42 and IR43) (Table **T12**). Both of these anomalies are present at the top of XCB cores, which are commonly slightly cooler than other parts of the core. Likely explanations include a larger than normal quantity of relatively cold drilling fluid entering the top of the core barrel during retrieval or gas expansion during retrieval. Recorded drilling parameters did not change significantly before, during, and after retrieval of these cores. Cooling from gas expansion, similar to that observed at Blake Ridge (Paull, Matsumoto, Wallace, et al., 1996), is perhaps less likely given the relatively low permeability of these sediments and the location of the anomalies at the core tops. In the case of the deep cold anomalies at Blake Ridge, some cores were actually retrieved frozen, apparently as a result of gas expansion in situ. Examples of gas-expansion cooling of the core liner have been observed in IR images (Core 204-1244A-7H), but neither of the anomalies noted here has features suggesting an obvious connection to gas expansion.

The IR data also show the thermal difference between XCB- and APC-cored intervals at this site, similar to that observed at Site 1244. This difference is shown in Figure **F27**, where XCB and APC cores were taken under similar ambient temperature conditions. There are at least four possible explanations for the temperature difference: (1) circulation of drilling fluid near the bit face during XCB coring; (2) greater tolerance and size variability between the core liner and the diameter of XCB core, resulting in greater movement of drilling fluid along the core during core recovery; (3) greater frictional heating during collection of APC cores; and (4) greater gas expansion or gas exsolution in XCB cores. At present, we cannot determine which of these four explanations is most important. For future hydrate drilling, it will be important to develop a better understanding of the relative thermal impacts of APC and XCB drilling. In some instances, the XCB is more effective for retrieving and preserving hydrate. For example, there was greater hydrate recovery just above the BSR in Hole 1251D (where the XCB was used) compared to Hole 1251B (where the ACP was used on the same interval). However, the circulation of drilling fluid in the case of XCB coring almost certainly produces a significant physical disruption of hydrate that needs to be considered in selecting the coring method for these types of sediments.

The thick thermal anomaly (hydrate zone) near the BSR in Hole 1251D provides an opportunity for relating chlorinity of IW to the presence of hydrate. Figure **F28** shows this relationship, clearly linking a zone of thermal anomaly with a negative chlorinity anomaly. These re-

F27. Downcore temperatures from IR scans, p. 68.

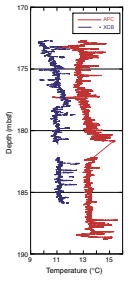

F28. Downcore temperature and chlorinity values, p. 69.

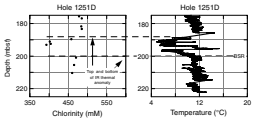

sults demonstrate the importance of selecting some IW samples within a meter or less of gas hydrate to increase the probability of detecting chlorinity anomalies (see also Fig. F25, p. 64, in the "Site 1245" chapter).

Sediment Density from Multisensor Track and Moisture and Density

A density profile was available prior to coring from the LWD program. In addition to the LWD data, routine sediment density measurements were carried out with the MST on whole-round cores (GRA density measurements) and on discrete samples (MAD measurements) (Table T13). The bulk density values show a perfect match with the LWD data (Fig. F29). The GRA density data show identical trends compared to those of MAD and LWD; however, the values were larger by ~0.3 g/cm³.

Sediment density at this site generally increases with depth from values of ~1.4 g/cm³ near the seafloor to ~1.9 g/cm³ at 300 mbsf. This is the expected trend resulting from normal compaction of the sediments. The boundary between lithostratigraphic Units I and II (defined at 130 mbsf) is not evident in the density records. However, the boundary between lithostratigraphic Units II and III is marked by a decrease in density. The density drop at 300 mbsf is well resolved in all three types of density measurements (MAD, LWD, and GRA). Values drop from ~1.9 g/cm³ at 320 mbsf to almost 1.5 g/cm³ at 370 mbsf. This boundary is also associated with a strong seismic reflector dipping east. (Fig. F30). The change in physical properties is caused by higher amounts of biogenic opal. This sediment component has a low grain density of ~2.0 g/cm³, resulting from the amorphous character of opal-A and a certain amount of structural water (up to 10%) within the silica phase. Within lithostratigraphic Unit III, a change in density occurs at ~360 mbsf. Density values increase at this depth to ~1.75 g/cm³ and are constant for the remainder of Hole 1251B. No seismic reflection can be associated with this increase in density. The deeper seismic record is characterized by a chaotic reflection pattern typically observed in accreted sediments.

Porosity decreases almost linearly from values of ~65% at the seafloor to ~50% at 300 mbsf. The porosity values in the low-density layer located between 320 and 370 mbsf are slightly higher at ~65%. Below 365 mbsf, porosity is nearly constant at values of ~55%. Calculated grain densities vary between 2.6 and 2.9 g/cm³ and are uniform for the entire site with an average value of 2.7 g/cm³.

Magnetic Susceptibility

The MS profile at Site 1251 is characterized by relatively uniform values of <40 $\times 10^{-7}$ (SI) but with occasional susceptibility peaks of up to 200 $\times$ 10^{-7} (SI) (Fig. F29). Most of the peaks observed on the MS profile can be correlated to sand layers (e.g., at 20 and 170 mbsf) or to the zones of abundant sulfides (e.g., at 130 mbsf). However, close comparison with the sedimentological record shows that there are no sand layers or sulfide zones below 400 mbsf that could explain the spikes in the MS.

T13. MAD index sample values, p. 111.

F29. Physical properties, p. 70.

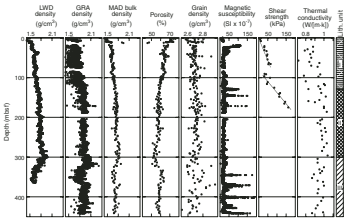

F30. Correlation between the seismic record and physical properties, p. 71.

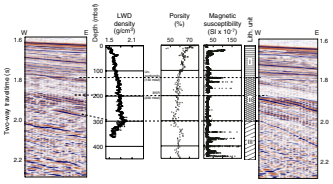

The boundary between lithostratigraphic Units I and II (unconformity) is marked by a spike in MS. However, an expanded view of the MS record at this depth shows that this spike is formed by two separate peaks (Fig. F31). A comparison with the core description shows that the high MS values correlate to the abundance of sulfides. This correlation was further investigated using the MS point sensor and X-ray images to help identify intervals with high sulfide concentrations (Fig. F31). The X-ray images are sensitive to variations in density. In general, sulfides form along small cracks or fill in former bioturbation features. On the X-ray images, darker spots (equivalent to higher-density material) are present at locations that also have larger MS values. Those spots are most likely sulfides, which have a much higher density than the surrounding sediments. It should be noted that pyrite (a common sulfide) does not have high MS and, thus, cannot be the cause of the anomaly. However, XRD analyses of a sulfide concretion found in Section 204-1244C-5H-4 showed a high abundance of pyrrhotite, a highly magnetic mineral. Sections 204-1251B-15H-2 through 15H-6 do not contain enough sulfide to be detectable by the onboard XRD. We were therefore not able to identify the magnetic mineralogy within this interval.

F31. MS anomaly, p. 72.

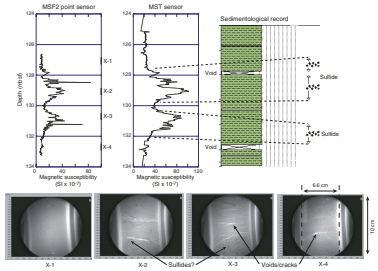

Non Contact Resistivity System

The NCR sensor was implemented for the first time as part of the suite of MST sensors at Site 1251. Early interfacing difficulties were overcome while drilling Hole 1251B, and it was possible to ensure consistent readings by "zeroing" before each core section was measured. This sensor system was still in a testing phase; therefore, we did not attempt any detailed interpretation of the data or correlate it to other physical properties at this site. We measured the resistivity for all cores recovered from Hole 1251B (Fig. F32). The resistivity was calculated from the raw values using the calibration function explained in "Physical Properties," p. 22, in the "Explanatory Notes" chapter. The measurements are very sensitive to the distance between the sensor and the surface of the core liner. The position of the sensor changed during the measurements of Hole 1251B between 90 and 173 mbsf, resulting in a shift of the raw values (Fig. F32). Because the relative position of the sensor to the core liner was not measured, no calibration is available for this range of depth.

F32. NCR, p. 73.

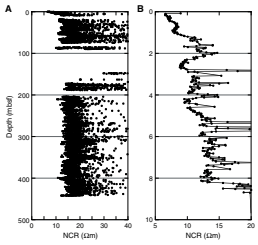

The NCR sensor produces data dominated by the effects of gas expansion in these sediments. It is, in fact, yet another MST "crack detector" similar to the GRA sensor and PWL. Gas voids in the core are electrical insulators and, hence, will provide very high resistivity values. It is clear from Figure F32B, which shows just the upper 10 m of data, that the cracks caused by gas expansion occur below 3 mbsf in Hole 1251B. Above 3 mbsf, the resistivity shows a discernible structure that is related directly to the sediment lithology rather than to the core disturbance caused by gas expansion. The conclusion from these first tests is that the NCR system is stable and can reliably measure the resistivity of the core, even if most of the measurements respond to the presence of gas expansion cracks or are dominated by other coring artifacts.

Compressional Wave Velocity from the Multisensor Track and Hamilton Frame Velocimeter

It is almost impossible to measure V_P at this site because of gas expansion. The V_P was measurable at only four points within the first meter below seafloor at Hole 1251B. The average value of these four data points is 1533 m/s. Only one velocity measurement was performed using the Hamilton Frame velocimeter, which gave a result of 1557 m/s (Table T14).

T14. V_P, p. 113.

Thermal Conductivity

Thermal conductivity measurements were made routinely after the cores were equilibrated to ambient room temperatures. The general procedure was to measure thermal conductivity in one section per core (normally in Section 3). However, in cores where special downhole temperature measurements were conducted, three thermal conductivity measurements were made in Sections 1, 3, and 5, respectively.

At Site 1251, the measured thermal conductivity values vary between 0.721 and 1.036 W/(m·K), with an average value of 0.933 W/(m·K) (Table T15; Fig. F29). Data are scattered in the upper 160 mbsf, possibly because of gas expansion in the sediment. A small downhole increase in thermal conductivity was observed to 200 mbsf. The thermal conductivity values are reduced slightly between 300 and 450 mbsf, with an average value of 0.945 W/(m·K).

T15. Thermal conductivity values, p. 114.

A plot of average normalized thermal conductivity vs. bulk density shows a good correlation between the two, indicating that the thermal conductivity is a direct function of water content in the sediments (Fig. F33).

F33. Comparison of normalized bulk density and thermal conductivity, p. 74.

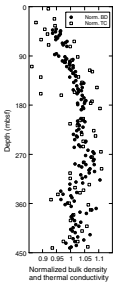

Shear Strength

Vane shear strength measurements were conducted on samples in Hole 1251B to a depth of 175 mbsf. Below 175 mbsf, the XCB coring technique disturbed the sediments too strongly to make reliable measurements. Measurements were made on the working half of the split core sections in locations where the sediment appeared generally undisturbed. Intervals within core sections exhibiting abundant cracks and voids resulting from gas expansion were avoided. Measured values vary between 4 kPa at shallow depths and 162 kPa at 175 mbsf (Table T16; Fig. F29). The shear strength increases linearly with depth (gradient = 0.5 kPa/m) from the seafloor to 80 mbsf, where a sharp decrease in shear strength is observed. This depth does not coincide with a change in shear vane size nor does it correspond to a change in stratigraphic unit or lithology. Below 80 mbsf, shear strength increases again linearly with depth but at a larger gradient (0.75 kPa/m) than that observed at shallow depth.

T16. Shear strength values, p. 115.

Summary and Discussion

The variations in physical properties at Site 1251 are consistent with the three main lithostratigraphic units discussed in "Lithostratigraphy," p. 3. The upper two units are characterized by uniformly increasing density values, probably a function of normal consolidation. The boundary between Units I and II is an unconformity, which is well defined in the seismic record. However, there is no apparent change in

density. The unconformity correlates to a spike in MS, which can be explained by diagenetic mineral formation (differences in sulfide abundance) within the sediments. The X-ray images show a high abundance of sulfides in those intervals that correlate to high MS values. One possible mineral is pyrrhotite, but it was not confirmed by XRD analysis at this horizon. A sulfide concretion found in Section 204-1244C-5H-4 was determined by XRD analysis to have a high concentration of pyrrhotite, but this was not large enough to be detected with the MS sensor of the MST. Small individual concretions can only be detected with the MS point sensor, which has the required spatial resolution. Another option to explain higher MS values is a change in sedimentation rate, which can result in changes of the relative concentration of magnetic minerals. However, with onboard techniques no definitive interpretation for the high MS values is possible.

Thermal imaging using the track-mounted IR camera on the catwalk provided the best method of detecting zones of gas hydrate in the cores at this site, especially when the hydrate occurred in disseminated form. Relatively low concentrations of hydrate were observed at Site 1251, except near the BSR, where IR anomalies and chlorinity indicate a zone of high hydrate concentration. The lateral extent of this zone is uncertain and important, as its presence or absence results in a relatively large difference in the total amount of hydrate estimated in the slope basin. Discrete samples of hydrate were not found in Hole 1251B, although several zones with cold anomalies were identified. The temperature anomalies observed in Hole 1251B were relatively small compared to the main anomaly encountered at Hole 1251D just above the BSR depth. These small thermal anomalies are interpreted to be indicative of disseminated hydrate.

DOWNHOLE TOOLS AND PRESSURE CORING

In Situ Temperature Measurements

Nine measurements of in situ temperatures were made at this site: five with the APCT tool and four with the DVTPP (Tables **T17, T18, T19**). Four of the APCT tool runs resulted in temperature histories that showed clear penetration and extraction pulses and smooth temperature decay (see **"Downhole Tools and Pressure Coring,"** p. 34, in the "Explanatory Notes" chapter). A fifth APCT tool run turned on prematurely and ran out of memory prior to recovery but recorded long enough to provide a good temperature measurement (Core 204-1251D-20H). Raw data are shown in Figure **F34.** Only data from the immediate time period before, during, and after tool insertion is shown. APCT data were modeled using the software program TFIT (as described in **"Downhole Tools and Pressure Coring,"** p. 34, in the "Explanatory Notes" chapter) measured thermal conductivities (see **"Physical Properties,"** p. 19). Uncertainty in the extrapolated value of in situ temperature resulting from subjective analyst picking of t_p, t_i, and t_f is <0.02°C for these high-quality records. Uncertainty resulting from uncertainty in values of thermal conductivity is ~0.02°C. Additional uncertainty results from uncertainty in instrument calibration (see **"Downhole Tools and Pressure Coring,"** p. 14, in the "Site 1246" chapter).

The DVTPP temperature data do not show the "textbook" response observed during the first deployment (Fig. **F34B**). Moreover, the run at 155.6 mbsf was noisy and showed an unrealistic value of 6.0°C for the

T17. Temperature measurements, p. 116.

T18. Results from degassing experiments, p. 117.

T19. HYACINTH pressure coring summary, p. 118.

F34. In situ temperatures, p. 75.

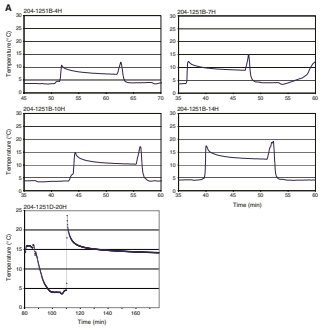

mudline temperature (measured at the end of the run), probably reflecting a calibration error for DVTPP tool 3. The DVTPP measurement at 198.6 mbsf yielded an anomalously low temperature value compared to the other data (Fig. F35). These two data points were not included in the determination of temperature gradient. The other two DVTPP deployments yielded temperatures consistent with the APCT data, suggesting that good-quality temperature measurements can be taken in spite of poor-quality pressure records. Moreover, the data suggest that there is no significant change in temperature gradient at the BSR, although this is not well constrained.

Least-square linear fit temperature gradients were calculated for different subsets of the data, excluding the two outliers. The solution is not sensitive to the inclusion or exclusion of the DVTPP data or to the mudline temperature estimate. The solution shown in Fig. F35 is for the combined data set. This temperature gradient predicts that the BSR should be at 202 mbsf, which is not significantly different from the BSR depth of 193 mbsf indicated by seismic data, given uncertainties in the velocity used to obtain the estimate of BSR depth.

F35. Subsurface temperatures, p. 77.

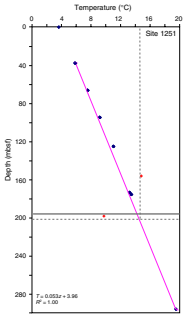

In Situ Pressure Measurements

Four in situ pressure measurements were attempted using the DVTPP. The signals from these measurements do not follow the expected decay patterns, suggesting problems with insertion of the probe. Interpretation of these measurements will be the object of postcruise research.

Pressure Core Sampler

The PCS was deployed nine times at Site 1251 (Table T18). Eight of these deployments were successful (i.e., a core under pressure was recovered). Only water was recovered during the other deployment because the tool actuated prematurely. The main objectives of the deployments were (1) to construct a detailed profile of concentration and composition of natural gases in the upper part of the section (0–300 mbsf) and (2) to identify the presence/absence and concentration of gas hydrate within the GHSZ.

Specific depth intervals were targeted for deployment of the PCS. Six cores (Cores 204-1251B-12P [104.1–105.1 mbsf] and 18P [153.6–154.6 mbsf]; 204-1251D-6P [45.9–46.9 mbsf], 10P [76.4–77.4 mbsf], and 21P [173.4–174.4 mbsf]; and 204-1251G-2P [20–21 mbsf]) were recovered from above the BSR at ~193 mbsf. Successful retrieval and degassing of Core 204-1251G-2P suggests that the PCS can be deployed at shallow subseafloor depths. The other two cores (Cores 204-1251B-35P [290.6–291.6 mbsf] and 204-1251D-29P [227.5–228.5 mbsf]) were recovered from below the BSR.

The time to degas the PCS chambers ranged from 672 to 1567 min (Table T18). Pressure was recorded during degassing experiments (Fig. F36). Gas was collected in a series of sample increments (splits), and most were analyzed for molecular composition (see "Organic Geochemistry," p. 16). In addition, gas splits were subsampled for onshore analyses. After degassing, the PCS chambers were disassembled. The lengths of the cores were measured (Table T18), and samples were taken for analysis of physical properties (see "Physical Properties," p. 19).

Gas was collected in 5- to 720-mL increments. The measured incremental and cumulative volumes are plotted vs. time (Fig. F36). The cu-

F36. Volume-pressure-time plots for the PCS, p. 78

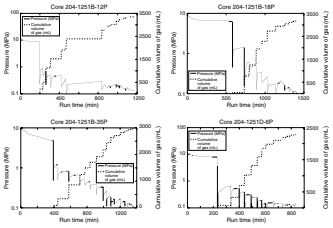

mulative volume of released gas varies from 1320 (Core 204-1251G-2P) to 3365 mL (Core 204-1251B-12P) (Table T18). The volume of the last gas splits varies from 5 (Core 204-1251B-12P) to 20 mL (Core 204-1251D-6P). This observation suggests that almost all gas present in the cores was collected.

Gases released from the PCS are mixtures of air (N_2 and O_2), CH_4, CO_2, and C_{2+} hydrocarbon gases (see "Gas Hydrate and Pressure Cores," p. 17, in "Organic Geochemistry"). The abundance of air components in the PCS gas samples (2.7%–53.2% of gas mixtures) suggests that air was not properly displaced from the PCS by seawater during deployments. Methane is the dominant natural gas present in collected gas splits. The molecular composition of gases from the PCS is similar to the composition of gas voids at adjacent depths (see Fig. F21).

Sediments in cores recovered with the PCS have lithologies that are similar to sediments recovered by the APC at adjacent depths (see "Physical Properties," p. 19). Porosity values measured on samples from APC cores taken near the PCS were used to estimate the methane concentration in situ (Table T18).

The concentration of methane in situ was estimated based on data from the degassing experiment (i.e., total volume of methane) and core examination (i.e., length of recovered core and the porosity of sediments). The calculation yields equivalent concentrations varying from 46.9 to 157.6 mM of methane in pore water. These concentrations have been compared with the theoretical methane-solubility curve extrapolated from values calculated for higher pressures (depths) (Handa, 1990; Duan et al., 1992) (Fig. F37).

F37. Methane concentration, p. 80.

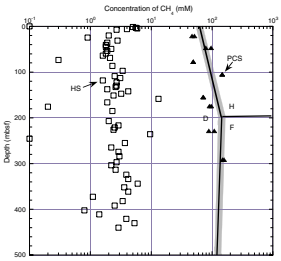

Preliminary analysis of gas concentrations suggests that gas hydrate may have been present in small concentrations (<1% of pore volume) in Cores 204-1251B-12P and 204-1251D-6P. In addition to relatively high gas concentrations, evidence of the presence of gas hydrate was found in the pressure record of core degassing (Fig. F36). However, other cores retrieved from the GHSZ, including Core 204-1251D-21P recovered from ~173.9 mbsf, just above the gas hydrate–bearing intervals inferred from IR thermal anomalies in Cores 22X and 24X at depths from 175 to 191 mbsf, suggest that only dissolved methane is present in some intervals within the GHSZ. A high concentration of methane in Core 204-1251B-35P may indicate the presence of free gas in the deep subsurface at ~291.1 mbsf (~100 m below the BSR), but only dissolved methane appears to be present in Core 204-1251D-29P, recovered from ~32 m below the BSR. Additional comparison of measured methane concentrations with theoretical methane solubility above and below the BSR will be performed on shore to better estimate if methane was present in situ in solution, in free phase, or as gas hydrate.

HYACINTH Pressure Cores

Coring Summary

Five deployments of the HYACINTH pressure coring tools were made at Site 1251: three with the FPC and two with the HRC (Table T19). These were the first deployments made during Leg 204 and were primarily considered to be engineering tests. One of the most important successes was the improvement in the handling of the tools and the downhole procedures compared with tests that had been conducted during previous legs (Legs 194 and 201). As a result, the total rig time used per deployment was limited to about 1.5 hr for each tool at this water

depth (1224 m). A number of minor technical and operational issues arose with each tool during the tests, which were addressed at each stage during the testing program. The final outcome at the end of Site 1251 was that the HRC had recovered a short 22-cm-long core (22% recovery) under pressure (but lower than in situ pressures) and the FPC had recovered good cores, 70–80 cm in length (70%–80% recovery), but without retaining pressure. Unfortunately, the DSA tool failed to provide any downhole data during the coring operations, which limited the ability for downhole performance analysis. However, the rig floor data will prove valuable in analyzing some aspects of the behavior during each deployment. The transfer chamber system was tested, but expanding cores and coring-related problems prevented a satisfactory transfer.

HYACE Rotary Corer Operations

The first two HRC deployments, Cores 204-1251B-48E (HRC 1) and 204-1251D-30E (HRC 2), were made at Site 1251, where the BSR is at 196 mbsf and which coincided with the transition between the use of the APC and XCB (194.6 mbsf) in Hole 1251B (see Table **T19**). This is relevant because it has been generally proposed that the type of material that is best suited for the HRC is at the upper limit of shear strengths that can be cored using the APC.

Core 204-1251B-48E (HRC 1) was collected in Hole 1251B at 396.9 mbsf, where the clay sediments are well indurated and the mechanical properties were considered well suited for the "dry auger bit" used by the HRC. Shear strengths in recovered cores from this depth are well in excess of the maximum shear strength that can be measured with the hand-held Torvane (250 kPa). Although large amounts of gas expansion were occurring in shallower parts of the hole, by this depth these expansion effects had almost disappeared and recovery with the XCB had been generally very good.

The tool was assembled for the first time on the pipe racker in 3 hr and fitted with the new strongbacks (one of these had been slightly shortened for easier handling on the rig floor). It was raised into a vertical position, and the strongbacks were removed as it was lowered into the shuck where the DSA tool was attached. This handling procedure (using the strongbacks) only took about 20 min and was a significant improvement compared to the last engineering tests of the tool during Leg 194, when it was assembled in a vertical position. It was then lifted into the drill pipe and lowered on the wireline while circulating and rotating. The tool was lowered onto the landing shoulder when the drill string rotation and circulation had been stopped, and slack wire was payed out. Problems with cleaning the hole resulted in lifting the tool out of the landing position at one time during the procedure. Pumping began slowly to build up pressure to activate the tool and continued at 93 gallons per minute (gpm), which causes the core barrel to rotate and cut core. However, a final pressure spike was not observed (even after 18 min) that would have indicated that the full stroke had been reached. Pumping was stopped while the drill string was lifted and continued for 2 min afterward to ensure full stroke. The tool was then raised on the wireline (slowly for the first 16 m) to the surface. The DSA tool was removed, and the HRC was broken into three vertical sections vertically and then taken aft to the pipe racker and laid on the trestles. On examination of the autoclave chamber, it was found that the core liner had broken (no core recovered) and that the by-pass port, which gives the

indication of end-stroke, had not opened. The evidence suggests that the tool may have been activated while it was still in the hanging position prior to landing at TD.

A second deployment of the HRC was planned at the bottom of Hole 1251B, but the hole was abandoned after poor hole conditions developed at around 445 mbsf. The HRC was again deployed at this site, Core 204-1251D-30E (HRC 2), at a depth of 229.5 mbsf. Although the lithology was softer at this depth compared with the material at ~400 mbsf, it was still considered useful (although not ideal) as a test for the HRC rotary cutter. The test proceeded smoothly with the handling on the rig floor being the same as for the previous deployment. This time there were no hole cleaning problems and pumping began after lowering to TD with the wireline slack. Active heave compensation was used throughout. Pumping was continued at 100 gpm for 15 min without observing any significant pressure spikes. The drill string was raised off bottom and a further 2 min of pumping (92 gpm) should have ensured full stroke of the coring barrel. The tool was then raised on the wireline slowly for the first 16 m and then continued at 110 m/min before being broken out of the drill string at the rig floor and placed in the adjacent shuck. The DSA tool was removed and the strongbacks attached before the tool was transferred to the trestles on the pipe-racker rather than being disassembled vertically. This procedure saves about 40 min compared with the vertical disassembly procedure.

This time the barrel had fully retracted, the flapper valve had closed, and the pressure was measured at ~20 kbar (much less than in situ pressure). However, the core got stuck during the transfer process and had to be removed manually. A 22-cm-long core (recovery = 22%) was recovered, but sediment smeared on the inside of the liner indicated that the majority of the cored material had not been retained in the barrel during retrieval, indicating that this type of catcher is not suitable for these soft formations. A leak was found later in the upper part of the autoclave section, which explained the loss of high pressure inside the chamber.

Fugro Pressure Corer Operations

The first three FPC deployments, Cores 204-1251B-21Y (FPC 1) and 40Y (FPC 2) and 204-1251D-28Y (FPC 3) were made at Site 1251 in a water depth of 1224 m. Core 204-1251B-21Y (FPC 1), at 171.7 mbsf, was in lithologies that were still suitable for the APC (XCB coring began at 194.6 mbsf) (see Table **T19**) and where large amounts of gas expansion were occurring. Shear strengths measured with the hand-held Torvane in Core 204-1251B-22H were ~160 kPa (see **"Physical Properties,"** p. 19), although it should be noted that in situ strengths are likely to be higher, perhaps by up to a factor of 1.5. Operationally, the deployment ran smoothly with the active heave compensator being used throughout (including pull-out). The total time taken for the complete operation was 1.5 hr.

On recovery, it was apparent that the coring mechanism had undergone a full stroke but had not fully retracted into the autoclave. However, a good-quality 0.71-m-long core had been cut (recovery = 71%). Under normal circumstances of autoclave recovery, the core would have been cut free from the piston under full pressure in the shear transfer chamber. We attempted to remove this core from the piston with a hacksaw; however, after one cut the core liner exploded violently, leaving a pile of shattered liner and sediment on the deck. Obvi-

ously the liner was under significant stress from the gas expansion, with the piston and the lower part of the core providing good seals. As the liner was first cut, a stress concentration probably occurred in the liner, allowing the catastrophic failure to propagate. An analysis indicated that a latching mechanism may not have been operating smoothly, which prevented the core from fully retracting into the autoclave. This was modified prior to the next deployment. Both the FPC and the DSA data loggers stopped prematurely and failed to capture data during the operations on the bottom.

A second deployment of the FPC was made in Hole 1251B at 329.6 mbsf, Core 204-1251B-40Y (FPC 2). At this depth, the sediments had not changed significantly in character apart from being more indurated. Shear strengths were outside the range of the hand-held Torvane device (>250 kPa). The operational procedures were the same as for Core 204-1251B-21Y (FPC 1) and again went smoothly, taking only ~1.5 hr. On recovery, it was apparent that this time the coring mechanism had fully retracted into the autoclave. However, a visual examination revealed that the lower flapper valve (which seals the lower end of the autoclave) had not fully closed, and hence, the autoclave was not pressurized. Subsequent investigations revealed that the flapper valve was unable to seal because of debris that fell out of the retracted liner onto the valve seating. We also discovered that the core liner had imploded. This was probably caused on pull out as a result of not fully stroking into the sediments. Unfortunately, both the FPC and the DSA data loggers again failed to capture the test interval and, hence, could not provide any diagnostic information about the tool's behavior.

The final FPC deployment at this site, Core 204-1251D-28Y (FPC 3), was made at the bottom of Hole 1251D at 226.5 mbsf. All operations were as for previous deployments except that the driller observed a 100-psi increase in pressure indicating an "end of stroke." After setting the tool on the trestles, we found that a good core had been taken (full stroke) but retraction into the autoclave had been prevented because one of the upper seals had been dislodged. The seal was caught by the holes inside the core barrel during retrieval and jammed the liner in the core barrel. This made it impossible to pull the core out of the autoclave. This was rectified prior to the next deployment. Care was taken when releasing the pressure inside the liner by drilling small holes and then cutting rather than simply using a hacksaw as with Core 204-1251B-21Y (FPC 1). The core was removed for logging and curation. During this deployment, the FPC pressure and temperature logger worked well but the DSA tool only collected data from the very beginning part of the test.

DOWNHOLE LOGGING

Logging While Drilling

Operations

LWD operations at Site 1251 began with replacing both the ADN tool and the RAB batteries prior to running pipe to the seafloor at 2300 hr Universal Time Coordinated (UTC) on 22 July 2002. Hole 1251A was spudded at a water depth of 1228.00 meters below rig floor (mbrf) ~3.2 nmi east of southern Hydrate Ridge. The LWD tool string included the GeoVision Resistivity (GVR) (RAB), MWD (Powerpulse), NMR-MRP tool,

and Vision Neutron Density (VND). An attempt to limit the initial ROP in the upper part of the hole to 25 m/hr was only partially successful. For the most part, the upper 30 mbsf of Hole 1251A was drilled at various ROP, ranging from values as low as 20 to as high as 70 m/hr. At a bit depth of ~30 mbsf, the ROP was increased and maintained at a high rate of ~50 m/hr to the bottom of the hole (BOH) at 380 mbsf. As a result of the higher ROP, the vertical resolution of the RAB tool images was reduced to ~10 cm and the NMR spectral data were also slightly degraded. The LWD tools were pulled to the rig floor at 1700 hr on 23 July for a total bit run of ~18 hr. Upon recovery, the LWD data from Hole 1251A were downloaded and the ship was offset to Site 1250.

Logging Quality

In general, the recorded LWD data from Hole 1251A are of good quality. There is minimal reduction in vertical resolution as a result of the faster ROP, and the borehole is in good shape through the shallow interval. Figure F38 shows the quality control logs for Hole 1251A. As discussed above, the ROP in the uppermost ~30 m of Hole 1251A was highly variable; however, below 30 mbsf the ROP was maintained at a relatively constant rate of 50 m/hr (±10 m/hr). This is sufficient to record one sample per 10-cm interval, which was obtained over 92% of the total section of the hole. The quality of RAB images is, thus, quite high, and no significant resolution loss is observed with variation in ROP in Hole 1251A.

The differential caliper log (DCAL), which gives the distance between the tool sensor and the wall of the borehole as recorded by the LWD density tool, is the best indicator of borehole conditions. The differential caliper values are <1 in over 90% of the total section in Hole 1251A. Only the uppermost ~38 m (0–38 mbsf) of the hole and the bottom ~70 m (310–380 mbsf) of the hole show washouts >1 in. The density correction (DRHO), calculated from the difference between the short- and long-spaced density measurements, varies from 0 to 0.175 g/cm³ (Fig. F38), which shows the good quality of the density measurements above ~280 mbsf. A standoff of <1 in between the tool and the borehole wall indicates high-quality density measurements with an accuracy of ±0.015 g/cm³.

Time-after-bit (TAB) measurements for most of Hole 1251A are 5 ± 2 min for ring resistivity and gamma ray logs and 50 ±10 min for density and neutron porosity logs (Fig. F38). TAB values remain relatively constant over most of the hole, coinciding with the relatively consistent ROP while drilling, although some large variations in ROP were observed near the top of the hole.

The depths relative to seafloor for all of the LWD logs were fixed by identifying the gamma ray signal associated with the seafloor and shifting the logging data to the appropriate depth as determined by the drillers pipe tallies. For Hole 1251A, it was determined that the gamma ray log pick for the seafloor was at a depth of 1216.5 mbrf. The rig floor logging datum was located 11.1 m above sea level.

F38. Quality control LWD logs, p. 81.

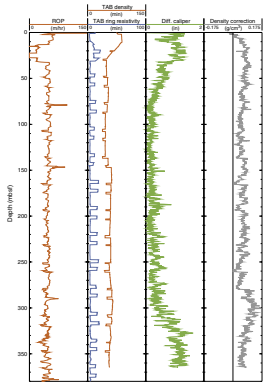

Wireline Logging

Operations

Hole 1251H was planned as a dedicated conventional wireline logging (CWL) hole and was to be drilled with a 9.875-in tricone rotary bit

to a depth 445 mbsf. The drilling target was reached much faster than anticipated, but the cleaning and conditioning of the hole proved to be difficult and time consuming. Rig-up for logging started at 2200 hr on 17 August, 14 hr after reaching the initial TD of the hole (445 mbsf). The first lowering of the triple combo tool string could not pass an obstruction at 240.5 mbsf; each subsequent log run to the bottom of the hole encountered more fill or obstructions. The final run of the FMS-sonic tool could not pass below 209.5 mbsf. The final rig down of the FMS-sonic tool was complete by 1145 hr on 18 August. See Table **T20** for detailed information on the Hole 1251 CWL program.

CWL operations in Hole 1251H began with the deployment of the triple combo tool string (TAP/DIT/HLDT/APS/HNGS/QSST) (Table **T20**). The triple combo tool string initially encountered a borehole bridge at a depth of 240.5 mbsf that it could not pass, which corresponds to the depth of the shallowest significant borehole breakouts on the LWD RAB images from Hole 1251A (Fig. **F39**). The quality of the data acquired during the main and repeat uplog pass of the triple combo tool string was moderately degraded because of the washed-out nature of the borehole (see **"Logging Quality,"** p. 31). Before the start of the second log pass, several checkshots were attempted with the QSST, but the signal-to-noise ratio was poor, preventing the acquisition of useful data. The repeat pass of the triple combo tool string was conducted over an interval from 225.5 mbsf up to the bottom of the pipe (78.5 mbsf). TAP and depth data were recorded without any problems. The triple combo logging run ended with the rig-down of the tool string being completed at 0645 hr on 18 August.

For the second CWL run in Hole 1251H, the FMS-sonic tool string (FMS/DSI/SGT) was deployed. The FMS-sonic tool string reached a maximum depth of 207.5 mbsf on two consecutive passes. The obstruction at 207.5 mbsf was near the depth of the BSR for this site (estimated at 205 mbsf) (see **"Introduction,"** p. 1). The length of the FMS-sonic tool string (31 m) prevented the recording of acoustic logging data across the estimated depth of the BSR. The FMS calipers also showed that most of the hole was severely enlarged, consistent with the HLDT caliper recorded on the triple combo run. DSI modes used for the first pass were the standard-frequency monopole, low-frequency lower dipole, and standard-frequency upper dipole. DSI modes used for the second pass were the same, except for the monopole run at low frequency. The recorded sonic waveforms are of very high quality, particularly the dipole recordings, but the very low velocity of this formation made it difficult for the automatic slowness/time coherence (STC) picking program to select accurate V_P. By increasing the maximum slowness of the dipole in the STC processing, we were able to accurately pick the shear velocity in the dipole waveforms. Despite an irregular hole, acoustic data from Hole 1251H are of good quality, but the DSI-derived V_P will require further reprocessing.

A final run was made for seismic experiments, which will be discussed elsewhere.

Logging Quality

The quality of the CWL data from Hole 1251H was moderately degraded by the size and uneven nature of the borehole (Figs. **F40, F41, F42, F43**). The triple combo caliper log from Hole 1251H (Fig. **F40**) shows borehole diameters greater than the 17.6-in maximum range of the caliper for a significant portion of the hole. The HLDT/APS/HNGS–

T20. CWL operations summary, p. 119.

F39. LWD data, p. 82.

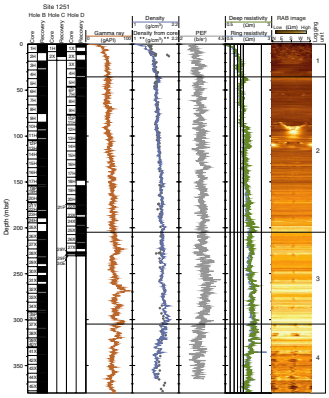

F40. CWL data, p. 83.

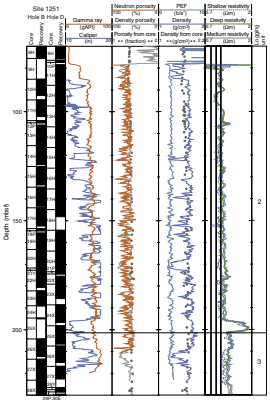

F41. CWL gamma ray logging data, p. 84.

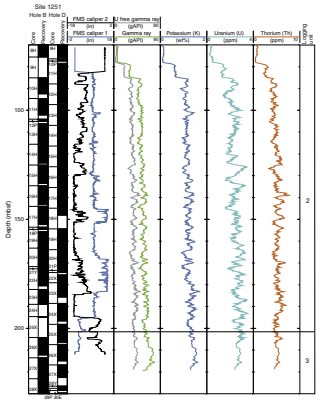

derived gamma ray, density, and neutron porosity data are particularly susceptible to the adverse effects from large and irregular hole diameters. The gamma ray logs (Figs. **F40, F41**) from Hole 1251H were not significantly affected by the size of the borehole. However, the density log in Hole 1251H was severely degraded within the depth interval from 120 to 197 mbsf. Relative to the density log measurements, the neutron log does not appear as severely degraded. The DIT and DSI also appear to yield useful resistivity and acoustic data (as discussed above).

The absolute depths, relative to seafloor, for all of the CWL logs were fixed by identifying the gamma ray signal associated with the seafloor and depth shifting the logging data appropriately. The gamma ray pick for the seafloor in Hole 1251H was 1219.5 mbrf for both CWL runs.

Interpretation of Logging While Drilling and Wireline Logging

Data from Holes 1251A and 1251H show excellent quality LWD logs and moderately degraded CWL logs. Analysis of LWD resistivity data and CWL acoustic and resistivity data suggests the presence of gas hydrate within two intervals at Site 1251, from 90 to 115 mbsf and 185 to 205 mbsf. Low- to high-density interbedding is observed throughout the hole below 130 mbsf, which likely indicates lithologic changes associated with turbidite sequences. The RAB images in Hole 1251A revealed borehole breakouts in the lower portion of the hole (300–380 mbsf) that are subparallel to similar features in Hole 1244D. NMR-MRP data were transmitted to shore for processing to estimate bound-fluid volume and total free-fluid porosity and for comparison with neutron, density, and core porosity estimates.

Logging-While-Drilling and Wireline Logging Comparison

Figure **F42** shows a comparison of downhole LWD and CWL data from Holes 1251A and 1251H using the gamma ray, neutron porosity, density, photoelectric factor, and deep resistivity logs. The highly variable CWL data within the upper 85 mbsf of Hole 1251H was obtained through the drill pipe. Comparison of similar log signatures on Figure **F42** reveals that the LWD data from Hole 1251A are offset by ~3 m relative to CWL data from Hole 1251H. This depth difference is best shown with the deep resistivity logs from the two holes. At a depth of ~196 mbsf in Hole 1251H, the CWL resistivity log shows a distinct increase in value; however, this same log response is at a depth of ~199 mbsf on the LWD data from Hole 1251A. This offset could possibly be explained by local variability in the geology of this site; however, Hole 1251H was located only 20 m south of Hole 1251A (Fig. **F1**). This apparent depth discrepancy will be further examined after the cruise. When considering the apparent depth difference between the two logged holes, the LWD and CWL gamma ray and resistivity logs as depicted in Figure **F42** match relatively well, exhibiting similar curve shapes and absolute log values. The CWL (Hole 1251H) and LWD (Hole 1251A) density and neutron logs, however, are still characterized by numerous mismatches and anomalies that do not correlate between the two holes. As discussed above, the CWL was degraded by enlarged borehole conditions. Within intervals of relatively in-gauge hole, such as between 85 and 120 mbsf, the CWL and LWD density logs compare favorably with the core-derived density data. The CWL- (Hole 1251H) and LWD-recorded (Hole 1251A) resistivity logs exhibit some differences in measured val-

F42. LWD and CWL downhole logging data, p. 85.

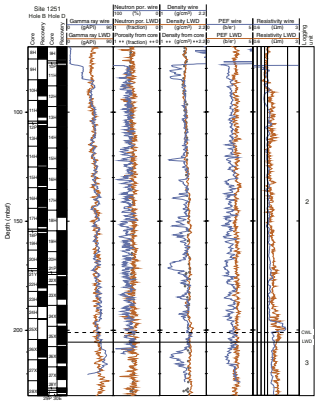

F43. CWL acoustic logging data, p. 86.

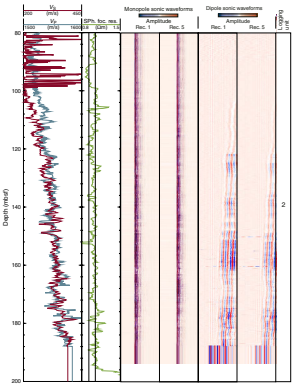

ues with depth and a difference in the apparent vertical resolution of each device, with the LWD RAB tool yielding a log with a higher vertical resolution.

Logging Units

The logged sequence in Holes 1251A and 1251H is divided into four "logging units" on the basis of obvious changes in the LWD and CWL gamma ray, density, electrical resistivity (Figs. **F39, F40, F41**), and acoustic velocity (Fig. **F43**).

Logging Unit 1 (0–36 mbsf) is characterized by increasing resistivities, densities, and gamma ray values with depth as measured by the LWD tools. However, this trend in the downhole logging data is probably due, in part, to degraded log measurements within the enlarged portion of the near-surface borehole as shown in Figure **F38.** The base of logging Unit 1 appears to coincide with the base of lithostratigraphic Subunit IB (34 mbsf), which is composed of clay to silty clay. The transition from logging Unit 1 to 2 is defined by an increase in electrical resistivity and formation densities.

Logging Unit 2 (36–205 mbsf) is characterized by zones of distinct high resistivity and somewhat higher V_P, with peak resistivity values exceeding 2 Ωm and V_P recorded at >1.59 km/s. The gamma ray log in this unit shows a characteristic cyclicity of values that may reflect the silty clay to clay interbedded turbidite sequences as described by the shipboard sedimentologists for Lithostratigraphic Subunits IC, IIA, and the upper part of Subunit IIB (34–300 mbsf) (see **"Lithostratigraphy,"** p. 3). The downhole LWD-measured densities increase with depth in logging Unit 2 (1.6 at the top to near 1.85 g/cm^3 at the bottom). Since the CWL acoustic transit-time log was not able to pass below the expected depth of the BSR (~193 mbsf) at this site, other downhole logging data were used to identify the base of the deepest LWD-CWL inferred presence of gas hydrate. The RAB resistivity logs have been used to select the depth of the boundary between logging Units 2 and 3, which is marked by a relatively dramatic drop in resistivity of >1 Ωm at a depth of 205 mbsf. Also noted on the LWD density log is a subtle drop in density at the contact between Units 2 and 3, which roughly corresponds to the depth of the BSR at this site. Because of an offset in resistivity logs between Holes 1251A and 1251H (as discussed above), the contact between logging Units 2 and 3 in Hole 1251H would be at 202 mbsf (Figure **F42**).

Logging Unit 3 (205–304 mbsf) correlates with the lower part of lithostratigraphic Subunit IIB (178–300 mbsf), which is described as an interbedded clay, silty clay, to sand turbidite sequence. Logging Unit 3 is generally characterized by numerous intervals of varying thickness that exhibit high resistivities (>1.7 Ωm) and low densities (<1.7 g/cm^3), which collectively suggest the presence of free gas–saturated sediments. The transition from Unit 3 to Unit 4 is marked by an abrupt drop in density (from ~1.9 to 1.7 g/cm^3) (Fig. **F39**), which appears to mark the contact with the underlying deformed sediments of the accretionary complex.

Logging Unit 4 (304–380 mbsf; TD of Hole 1251A), reflecting the upper portion of the deformed sediments of the accretionary complex, is characterized by highly variable resistivity and density measurements that are the result of enlarged borehole breakouts (with DCAL values >1 in). These breakouts appear consistently with nearly a north-south orientation in the borehole.

Resistivity-at-the-Bit and Formation MicroScanner Images

The RAB tool produces high-resolution images of the electrical resistivity characteristics of the borehole wall that can be used for detailed sedimentological and structural interpretations. The RAB tool can also be used to make high-resolution electrical images of gas hydrates in the borehole, thus yielding information about the nature and texture of gas hydrates in sediments. During Leg 204, the RAB images proved to be a useful tool for evaluation of borehole breakouts, which are the product of differential horizontal stresses acting on the borehole. In Figure **F44**, the RAB image from Hole 1251A shows a dominant set of parallel borehole breakouts oriented approximately north-south.

F44. RAB image showing borehole breakouts, p. 87.

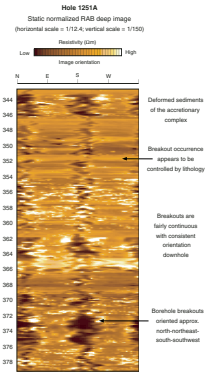

Logging Porosities

Sediment porosity can be determined from analyses of recovered cores and from numerous borehole measurements (see **"Physical Properties,"** p. 22, and **"Downhole Logging,"** p. 43, both in the "Explanatory Notes"). Data from the LWD density, neutron, and NMR-MRP logs have been used to calculate sediment porosities for Hole 1251A. Core-derived physical property data, including porosity (see **"Physical Properties,"** p. 19), have been used to both calibrate and evaluate the log-derived sediment porosities.

The VND LWD log-derived measurements of density in Hole 1251A (Fig. **F39**) are relatively consistent throughout most of the hole, with values ranging from ~1.5 near the seafloor to over 1.9 g/cm³ at the bottom of logging Unit 3 at 304 mbsf. The density log measurements are degraded in logging Unit 4, as discussed earlier in this chapter. The LWD log-derived density measurements (ρ_b) from Hole 1251A were used to calculate sediment porosities (ϕ) using the standard density-porosity relation,

$$\phi = (\rho_m - \rho_b)/(\rho_m - \rho_w).$$

Water density (ρ_w) was assumed to be constant and equal to 1.05 g/cm³; however, variable core-derived grain/matrix densities (ρ_m) were assumed for each logging density-porosity calculation. The core-derived grain densities (ρ_m) in Hole 1251A ranged from an average value at the seafloor of 2.69 to ~ 2.71 g/cm³ at the bottom of the hole (see **"Physical Properties,"** p. 19). The density log-derived porosities in logging Units 1 through 3 (0–304 mbsf) of Hole 1251A range from ~45% to 70% (Fig. **F45**). However, the density logging porosities in logging Unit 4 (304–380 mbsf) are more variable, ranging from 45% to 72%, which is in part controlled by poor borehole conditions.

F45. LWD- and core-derived porosities, p. 88.

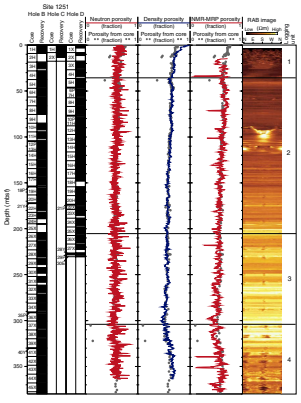

The LWD neutron porosity log from Hole 1251A (Fig. **F45**) yielded sediment porosities ranging from an average value at the top of the logged section of ~70% to ~60% in logging Unit 4. The "total" sediment porosities derived by the LWD NMR tool in Hole 1251A (Fig. **F45**) ranged from ~75% near the seafloor to ~55% near the bottom of the hole.

In studies of downhole logging data, it is common to compare porosity data from different sources to evaluate the results of particular measurements. The comparison of core- and log-derived porosities in Figure **F45** reveals that the density log-derived porosities are generally similar to the core porosities in logging Units 2 through 3 (36–304 mbsf). However, the density log-derived porosities are generally higher than the

core-derived porosities in logging Units 1 and 4. The neutron- and NMR-MRP–derived log porosities are generally similar to the core-derived porosities in logging Units 1 and 2, but the neutron and NMR-MRP log porosities are higher than the core-derived porosities throughout most of logging Units 3 and 4. The NMR-MRP porosity log also exhibits numerous low-porosity zones throughout the entire hole, which will be further evaluated after the cruise.

Gas Hydrate

Several specimens suspected of containing gas hydrate were preserved from Hole 1251C at depths of 175.4, 178.11, 189.87, and 190.72 mbsf (Fig. **F46**). Despite the limited samples of gas hydrates, it was inferred, based on geochemical pore water analyses (see **"Interstitial Water Geochemistry,"** p. 13), IR image analysis of cores (see **"Physical Properties,"** p. 19), and downhole-logging data that disseminated gas hydrate is present in portions of logging Unit 2. As previously discussed in **"Downhole Logging,"** p. 43, in the "Explanatory Notes" chapter, the presence of gas hydrate is generally characterized by increases in logging-measured electrical resistivities and acoustic velocities. Certain zones in logging Unit 2 at Site 1251 are characterized by distinct stepwise increases in both electrical resistivities and acoustic velocities.

Resistivity log data were used to quantify the amount of gas hydrate at Site 1251. For the purpose of discussion, it is assumed that the high resistivities and velocities measured in logging Unit 2 are due to the presence of gas hydrate. Archie's Relation,

$$S_w = (aR_w/\phi^m R_t)^{1/n}$$

(see **"Downhole Logging,"** p. 43, in the "Explanatory Notes" chapter), was used with resistivity data (R_t) from the LWD RAB tool and porosity data (ϕ) from the LWD density tool to calculate water saturations in Hole 1251A. It should be noted that gas hydrate saturation (S_h) is a measurement of the percentage of pore space in sediment occupied by gas hydrate, which is the mathematical complement of Archie-derived S_w, with

$$S_h = 1 - S_w.$$

For Archie's Relation, the formation water resistivity (R_w) was calculated from recovered core water samples and the Archie a and m variables were calculated using a crossplot technique, which compares the downhole log-derived resistivities and density porosities. See Collett and Ladd (2000) for details on how to calculate the required formation water resistivities and Archie variables. The values used for Site 1251 were $a = 1$, $m = 2.8$, and $n = 1.9386$.

Archie's Relation yielded water saturations (Fig. **F46**) ranging from an average minimum value of ~82% to a maximum value of 100% in logging Unit 2 (31–205 mbsf) of Hole 1251A, which implies the gas hydrate saturations in logging Unit 2 range from 0% to 18%. The low water saturations shown in logging Unit 3 that fall below the predicted base of the methane hydrate stability zone (Fig. **F46**) are indicative of free gas–bearing sediments.

F46. LWD-derived water saturations, p. 89.

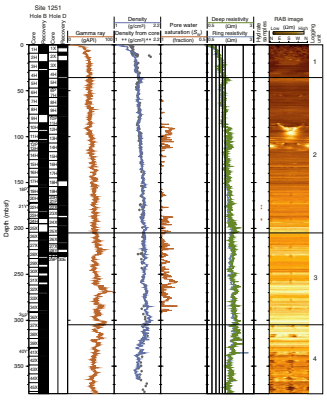

Temperature Data

The TAP tool was deployed on the triple combo tool string in Hole 1251H (Fig. F47). During the process of coring and drilling, cold seawater is circulated in the hole, cooling the formation surrounding the borehole. Once drilling ceases, the temperature of the fluids in the borehole gradually rebounds to the in situ equilibrium formation temperatures. Thus, the temperature data from the TAP tool cannot be easily used to assess the nature of the in situ equilibrium temperatures. However, the plot of the first pass downgoing temperature profile in Figure F47 reveals several gradient changes, which were caused by borehole temperature anomalies. The temperature anomaly at ~78.5 mbsf is the base of the drill pipe during the initial descent of the triple combo tool string. The break in the slope of the first pass downgoing temperature log at a depth ~210 mbsf is near the depth of the BSR (205 mbsf) at this site.

F47. TAP tool temperatures, p. 90.

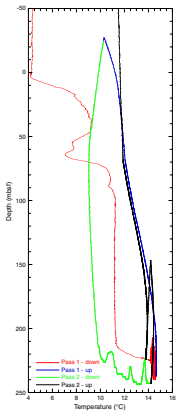

REFERENCES

Berggren, W.A., Kent, D.V., Swisher, C.C., III, and Aubry, M.-P., 1995. A revised Cenozoic geochronology and chronostratigraphy. *In* Berggren, W.A., Kent, D.V., Aubry, M.-P., and Hardenbol, J. (Eds.), *Geochronology, Time Scales and Global Stratigraphic Correlation*. Spec. Publ.—SEPM, 54:129–212.

Berner, R.A., 1980. *Early Diagenesis: A Theoretical Approach:* Princeton, NJ (Princeton Univ. Press).

Borowski, W.S., Paull, C.K., and Ussler, W., III, 1996. Marine pore-water sulfate profiles indicate in situ methane flux from underlying gas hydrate. Geology, 24:655–658.

Clague, D., Maher, N., and Paull, C.K., 2001. High-resolution multibeam survey of Hydrate Ridge, offshore Oregon. In Paull, C.K., and Dillon, W.P. (Eds), *Natural Gas Hydrates: Occurrence, Distribution, and Detection*. Am. Geophys. Union, Geophys. Monogr. Ser., 124:297–306.

Collett, T.S., and Ladd, J., 2000. Detection of gas hydrate with downhole logs and assessment of gas hydrate concentrations (saturations) and gas volumes on the Blake Ridge with electrical resistivity log data. *In* Paull, C.K., Matsumoto, R., Wallace, P.J., and Dillon, W.P. (Eds.), *Proc. ODP, Sci. Results,* 164: College Station, TX (Ocean Drilling Program), 179–191.

Deyhle, A., Kopf, A., and Eisenhauer A., 2001. Boron systematics of authigenic carbonates: anew approach to identify fluid processes in accretionary prisms. *Earth Planet. Sci. Lett.,* 187:191–205.

Duan, Z., Møller, N., Greenberg, J., and Weare, J.H., 1992. The prediction of methane solubility in natural waters to high ionic strengths from 0° to 250°C and from 0 to 1600 bar. *Geochim. Cosmochim. Acta,* 56:1451–1460.

Duncan, J.R., Fowler, G.A., and Kulm, L., 1970. Planktonic foraminiferal-radiolarian ratios and Holocene–late Pleistocene deep sea stratigraphy off Oregon. *Geol. Soc. Am. Bull.,* 81:561–566.

Goldhaber, M.B., and Kaplan, I.R., 1974. The sulfur cycle. *In* Goldberg, E.D. (Ed.), *The Sea* (Vol. 5): *Marine Chemistry: The Sedimentary Cycle:* New York (Wiley-Interscience), 569–655.

Handa, Y.P., 1990. Effect of hydrostatic pressure and salinity on the stability of gas hydrates. *J. Phys. Chem.,* 94:2652–2657.

Kastner, M., Kvenvolden, K.A., Whiticar, M.J., Camerlenghi, A., and Lorenson, T.D., 1995. Relation between pore fluid chemistry and gas hydrates associated with bottom-simulating reflectors at the Cascadia margin, Sites 889 and 892. In Carson, B., Westbrook, G.K., Musgrave, R.J., and Suess, E. (Eds.), *Proc. ODP, Sci. Results,* 146 (Pt. 1): College Station, TX (Ocean Drilling Program), 175–187.

Kitano, Y., Okumaura, M., and Idogak, M., 1978. Uptake of phosphate ions by calcium carbonate. *Geochem. J.,* 12:29–37.

Odin, G.S., and Matter, A., 1981. Die glauconarium origine. *Sedimentology,* 28:611–643.

Paull, C.K., Matsumoto, R., Wallace, P.J., et al., 1996. *Proc. ODP, Init. Repts.,* 164: College Station, TX (Ocean Drilling Program).

Rothwell, R.G., Thomson, J., and Kahler, G., 1998. Low-sea-level emplacement of a very large late Pleistocene megaturbidite in the western Mediterranean Sea. *Nature,* 392:377–380.

Spivack, A.J., and You, C.F., 1997. Boron isotopic geochemistry of carbonates and pore waters, Ocean Drilling Program Site 851. *Earth Planet. Sci. Lett.,* 152:113–122.

You, C.-F., Spivack, A.J., Gieskes, J.M., Martin, J.B., and Davisson, M.L., 1996. Boron contents and isotopic compositions in pore waters: a new approach to determine temperature induced artifacts-geochemical implications. *Mar. Geol.,* 129:351–361.

Figure F1. Bathymetric map showing locations of holes drilled at Site 1251. Bathymetry from EM300 data acquired by Monterey Bay Aquarium Research Institute (MBARI) (Clague et al., 2001).

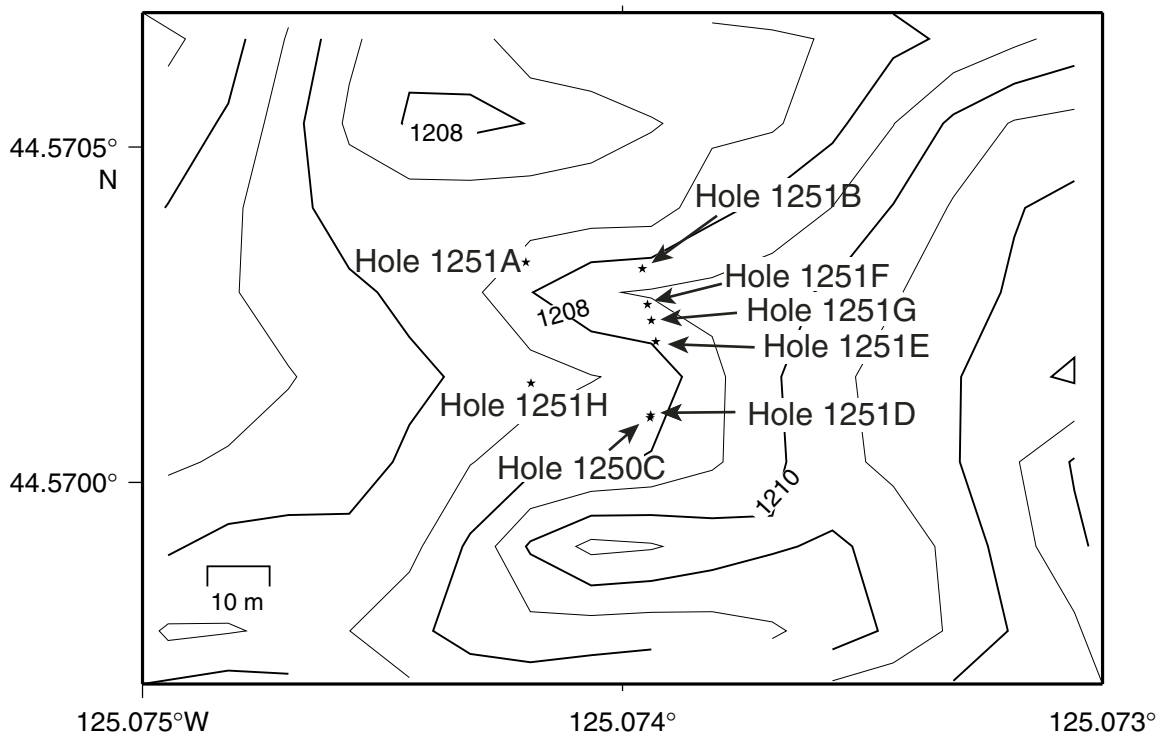

Figure F2. Lithostratigraphic summary for Site 1251. (Continued on next two pages.)

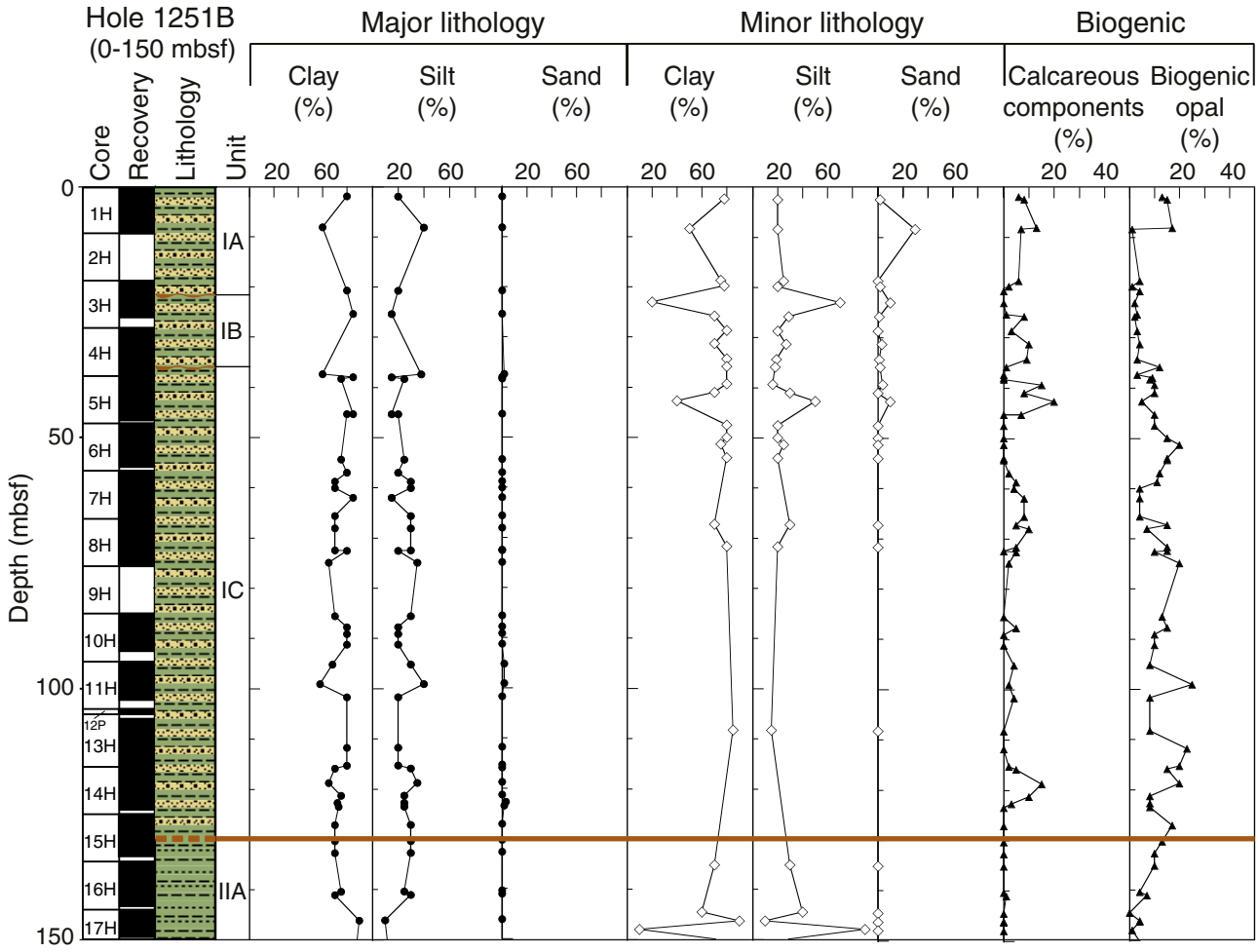

Figure F2 (continued).

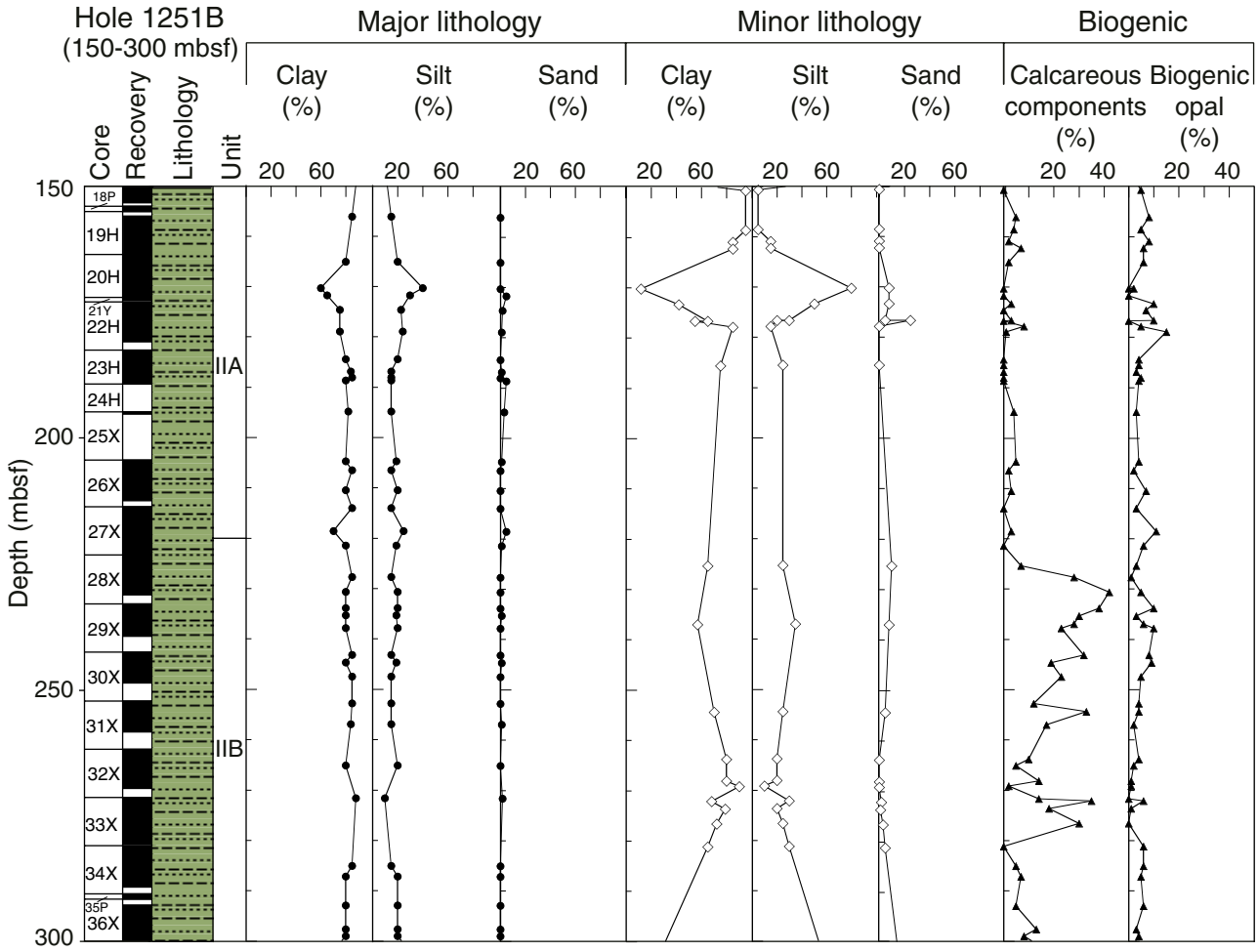

Figure F2 (continued).

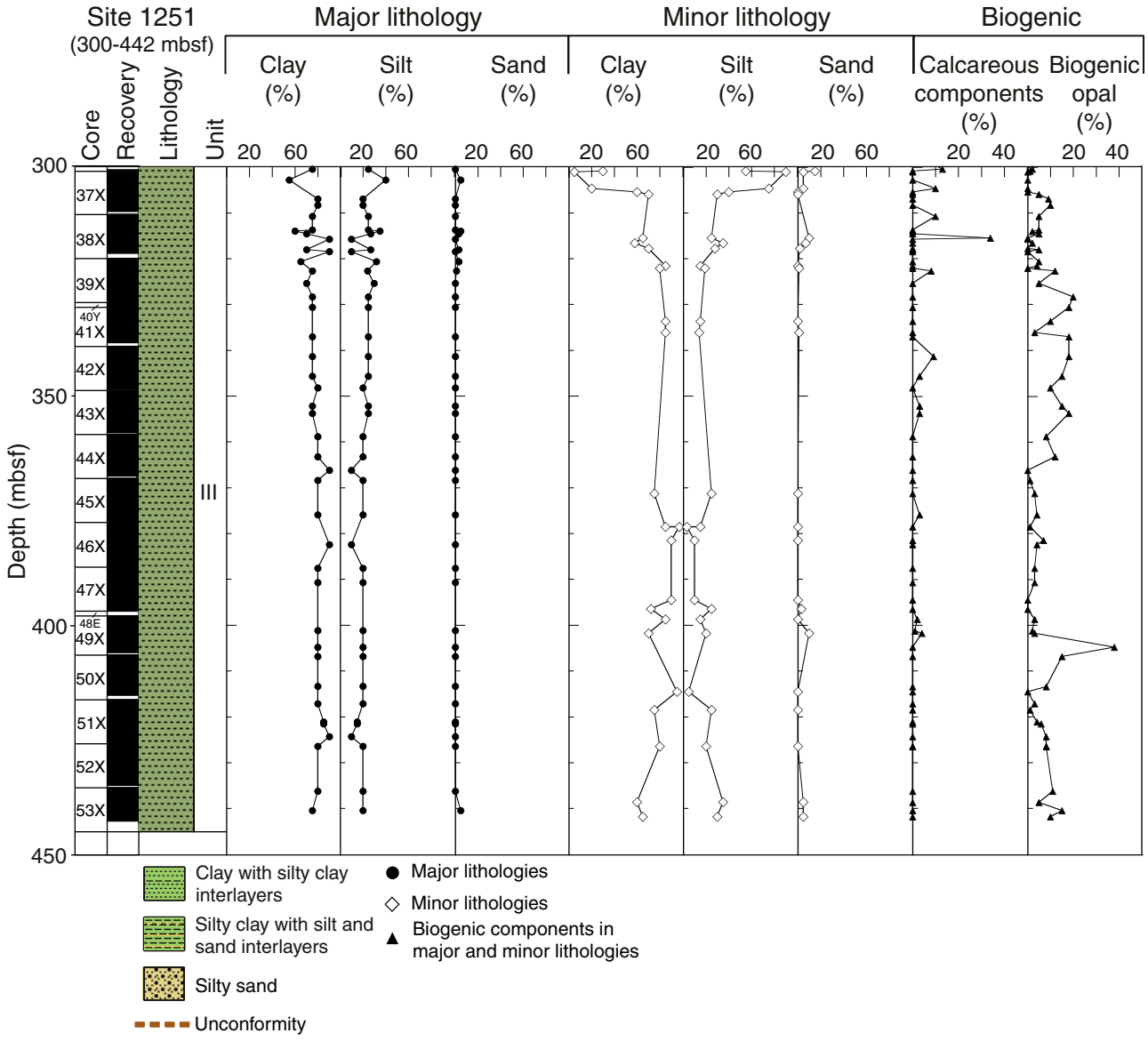

Figure F3. Abundance of clay, silt, sand, calcareous components, and biogenic opal in Hole 1251B (major and minor lithologies) based on smear slide descriptions.

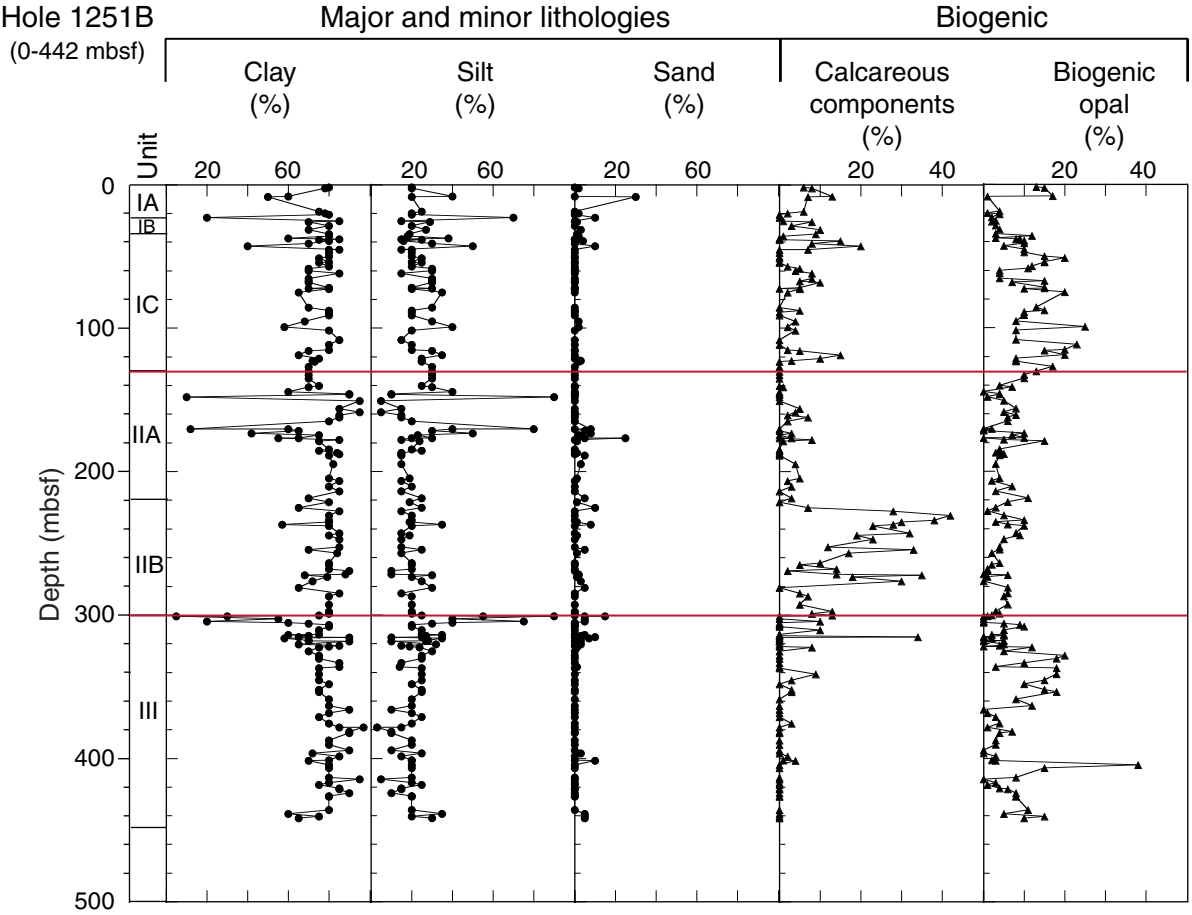

Figure F4. Seismic reflection profile from west (left) to east (right) across Site 1251. Correlation of lithostratigraphic units and subunits and seismic reflection, downhole gamma ray attenuation (GRA) density, MS, and CWL electrical resistivity (left curve) and CWD density (right curve) are shown. BSR = bottom simulating reflector, AC = accretionary complex, DFl = debris flow 1 (see Fig. **F5,** p. 45). U = unconformity. Note the location of the only gas hydrate sample recovered at this site from Hole 1251D (see Fig. **F20,** p. 70, in the "Leg 204 Summary" chapter). SF = seafloor, DF = debris flow, BSR = bottom-simulating reflector.

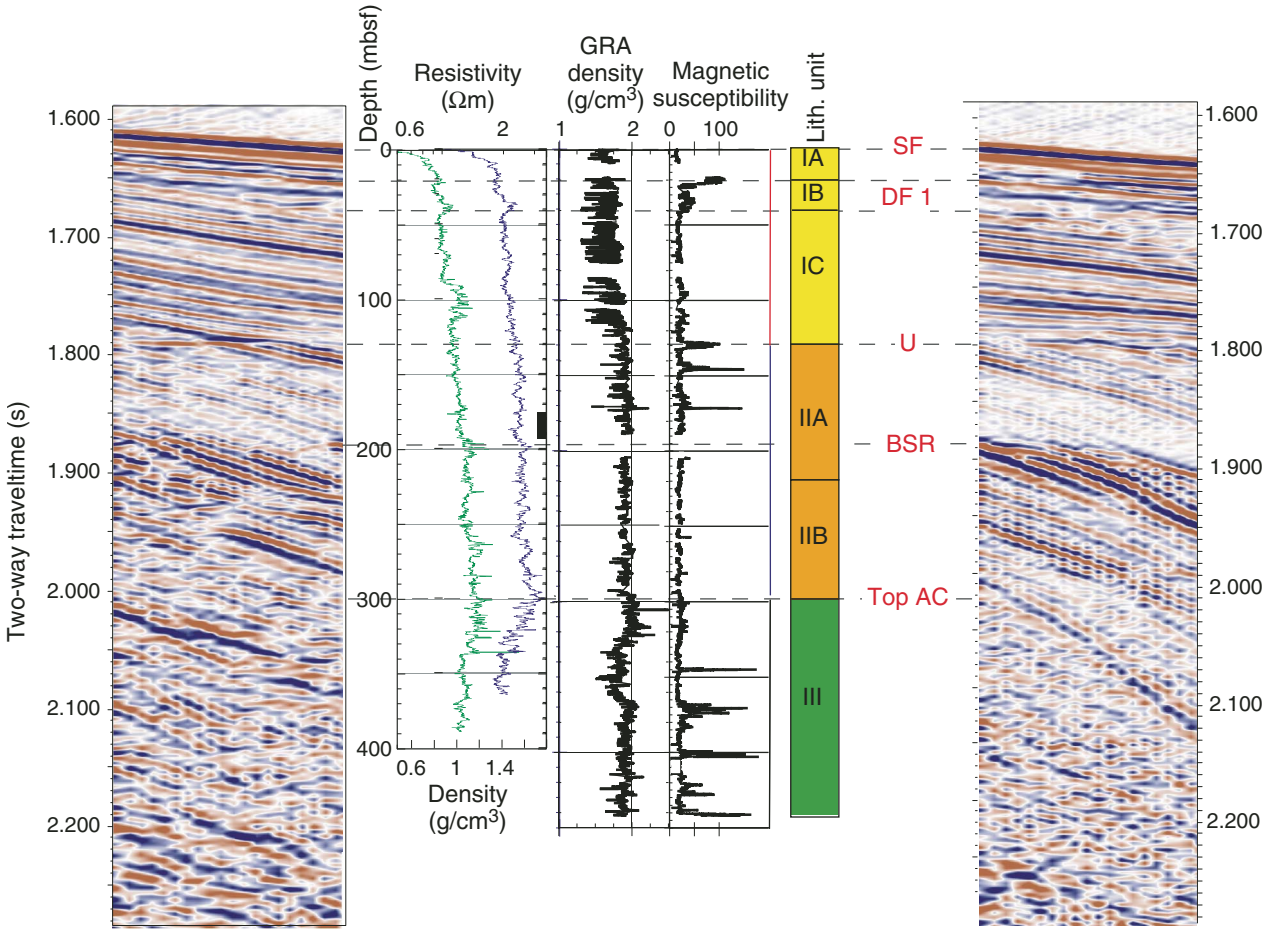

Figure F5. Seismic reflection profile from west (left) to east (right) across the location of Site 1251. Lithostratigraphic units and subunits are shown. BSR = bottom-simulating reflector.

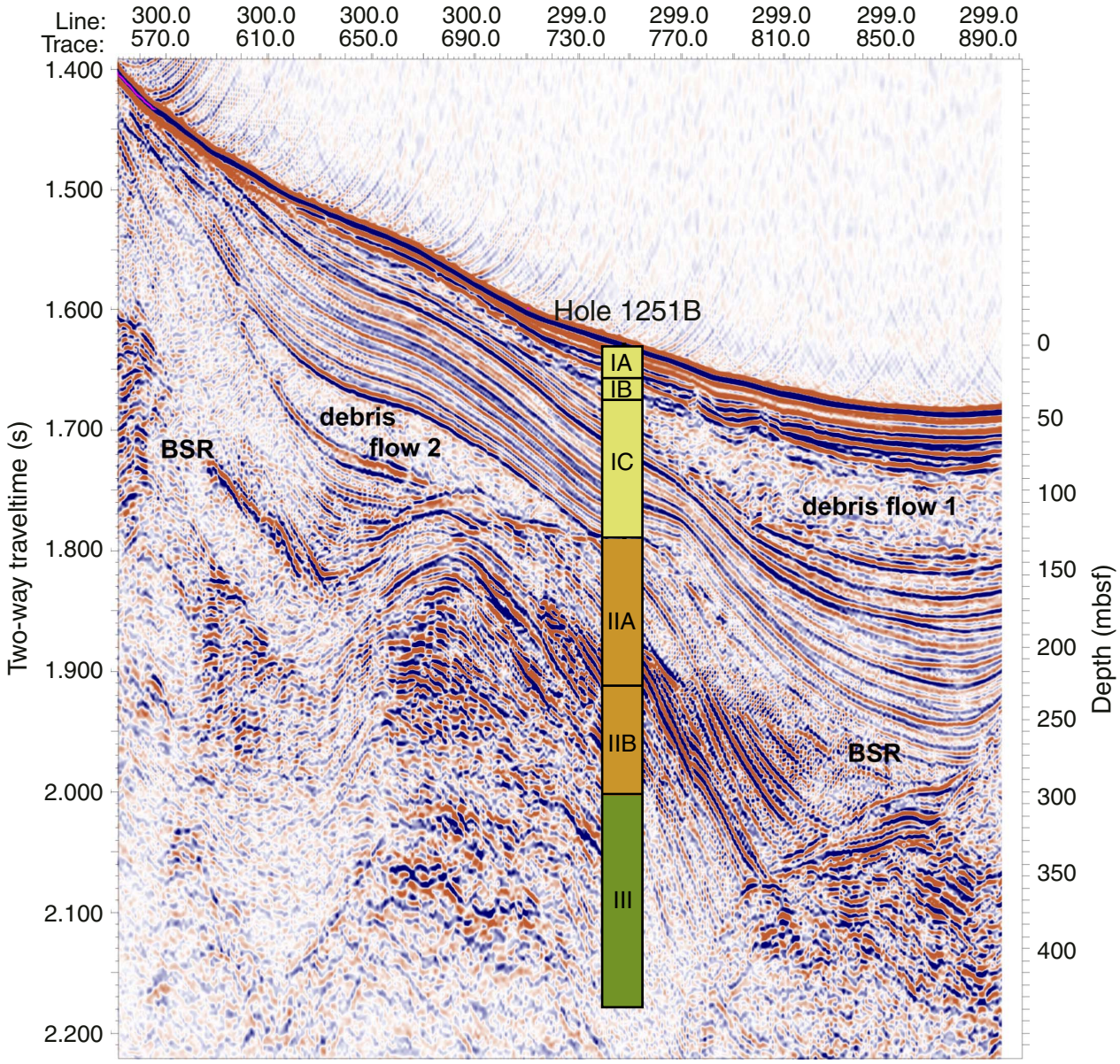

Figure F6. A. Close-up photograph of a turbidite (interval 204-1251C-2X-4, 70–81 cm), typical of the lower portion of lithostratigraphic Subunit IA. **B.** Core photograph of soft clasts in an interpreted debris flow (interval 204-1251B-3H-5, 35–55 cm), typical of lithostratigraphic Subunit IB.

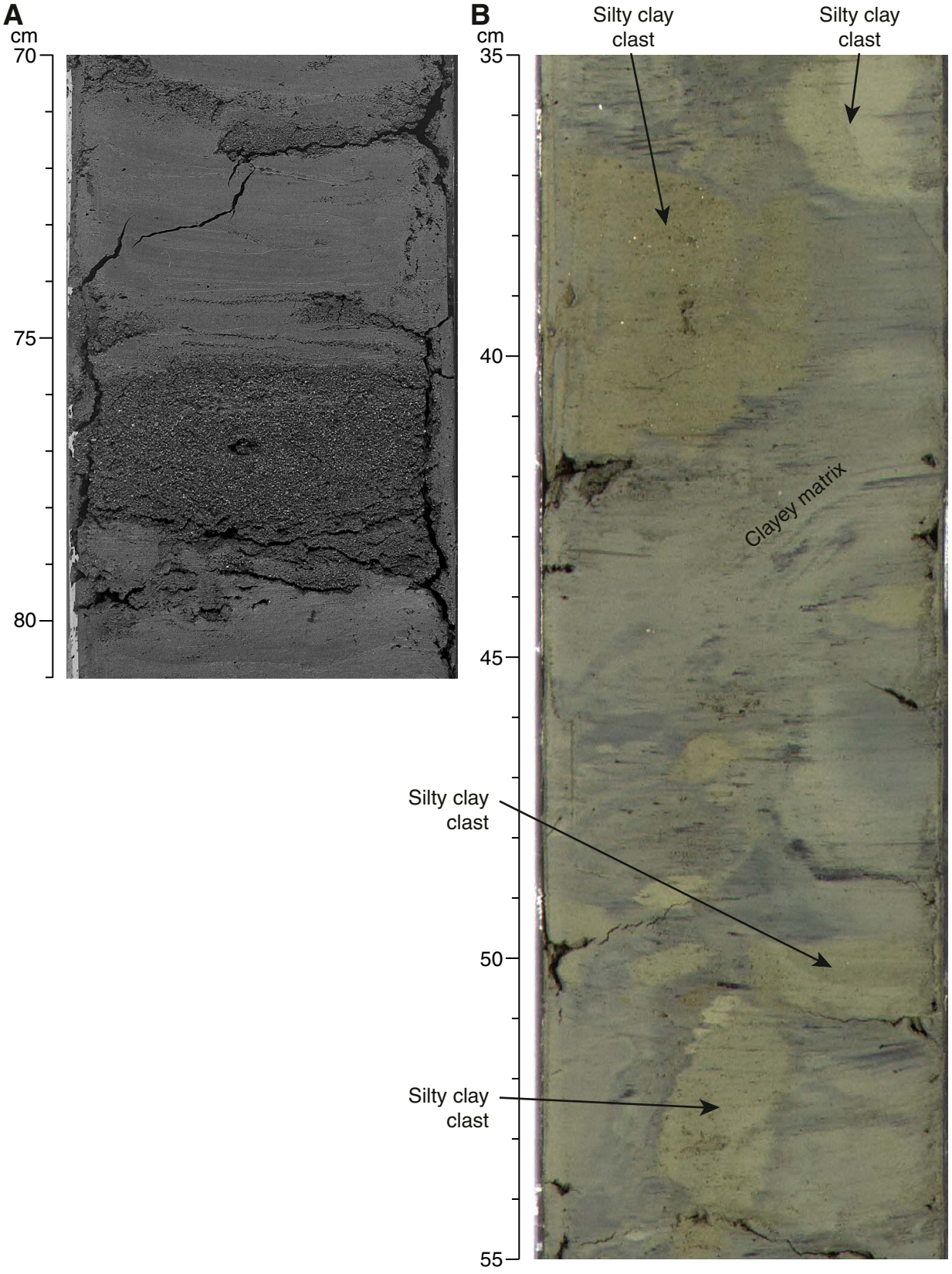

Figure F7. A. Abundance of glauconite vs. depth in Hole 1251B based on smear slide descriptions of the major and minor lithologies. **B.** Weight percent $CaCO_3$ vs. depth in Hole 1251B, determined by coulometry (see **"Organic Geochemistry,"** p. 16, in the "Explanatory Notes" chapter).

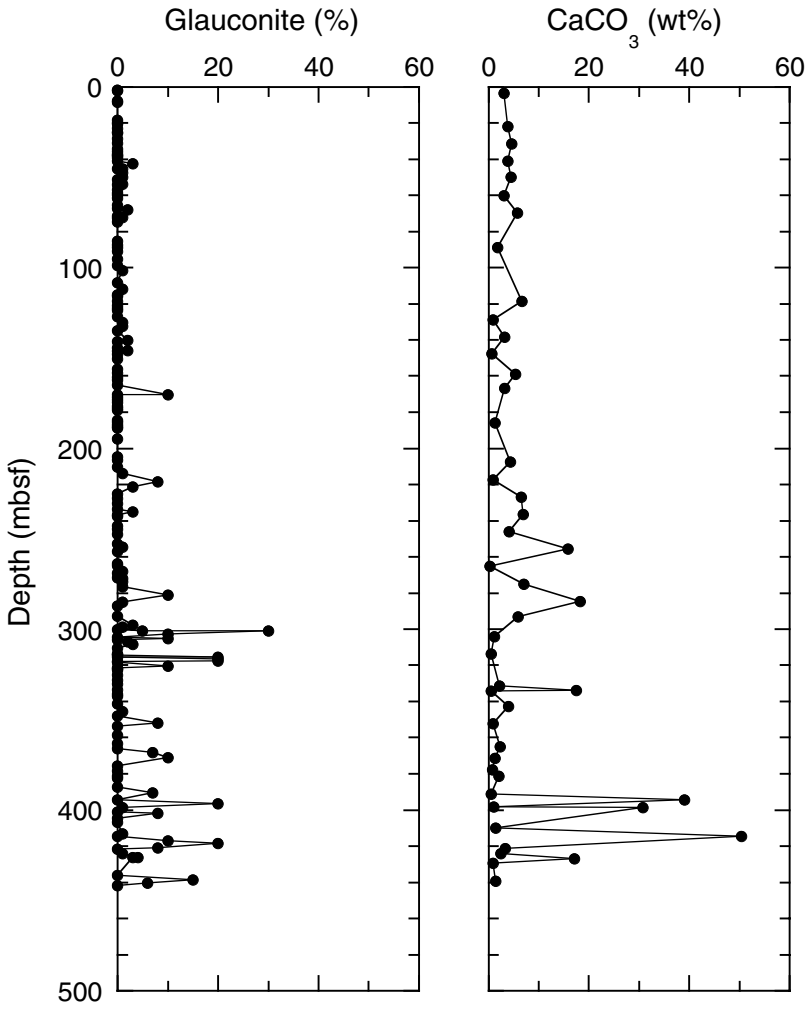

Figure F8. A. Close-up photograph of foraminifer-rich clay (interval 204-1251B-36X-CC, 16–21 cm) showing visible foraminifer tests (small light-colored specks) (lithostratigraphic Subunit IIB). **B.** Photomicrograph of nannofossil-rich foraminifer-bearing clay (100×) (Sample **204-1251B-28X-CC, 44 cm**) (lithostratigraphic Subunit IB).

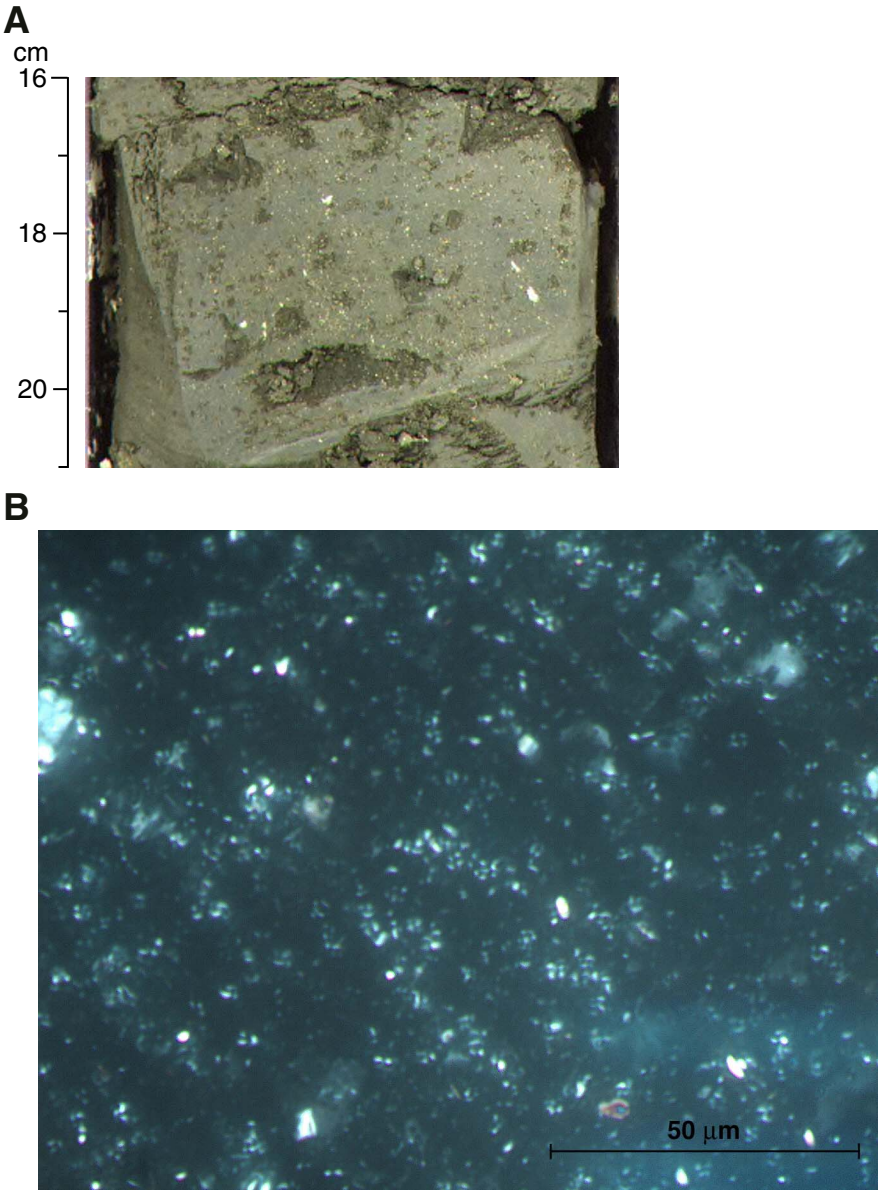

Figure F9. A. Glauconite-rich clay occurrence (interval 204-1251B-37X-1, 28–37 cm) (lithostratigraphic Unit III). **B.** Close-up photograph of carbonate nodule (interval 204-1251B-52X-1, 128–140 cm) (lithostratigraphic Unit III). **C.** Photomicrograph of diatom-rich clay (20×) (interval 204-1251B-42X-2, 50 cm) (lithostratigraphic Unit III).

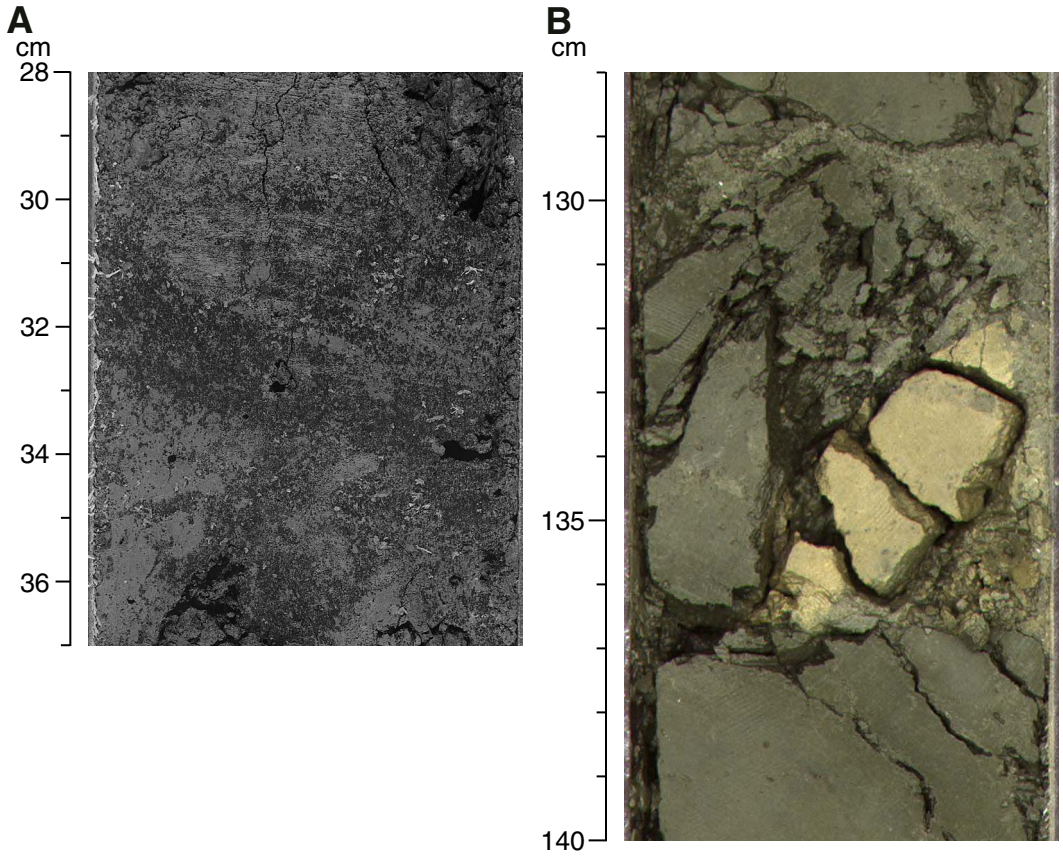

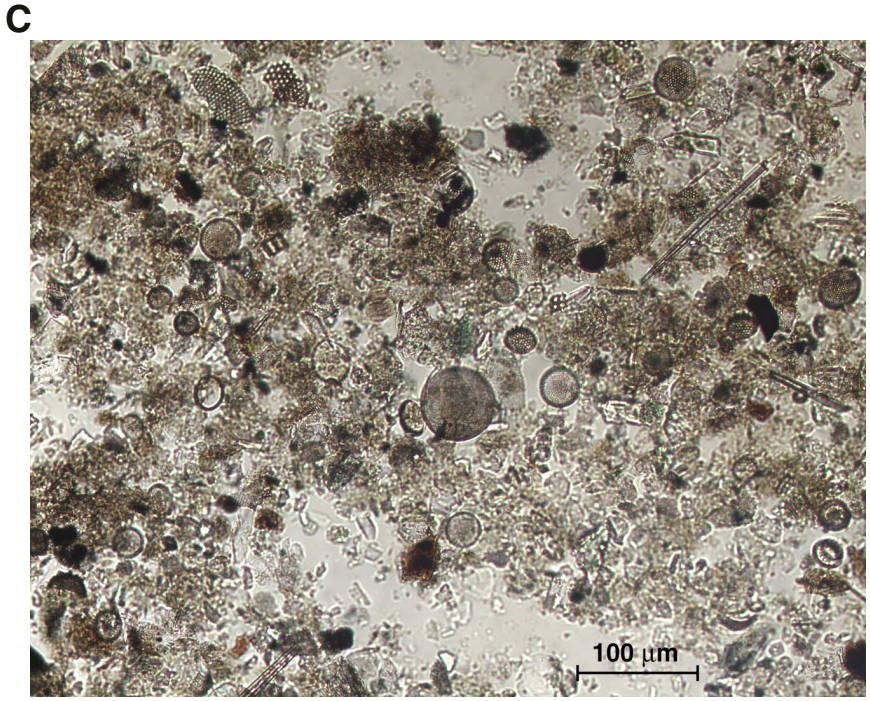

Figure F10. A. XRD record from a dolomite. **B.** XRD record showing two carbonate phases. **C.** XRD record of a light-colored sediment patch.

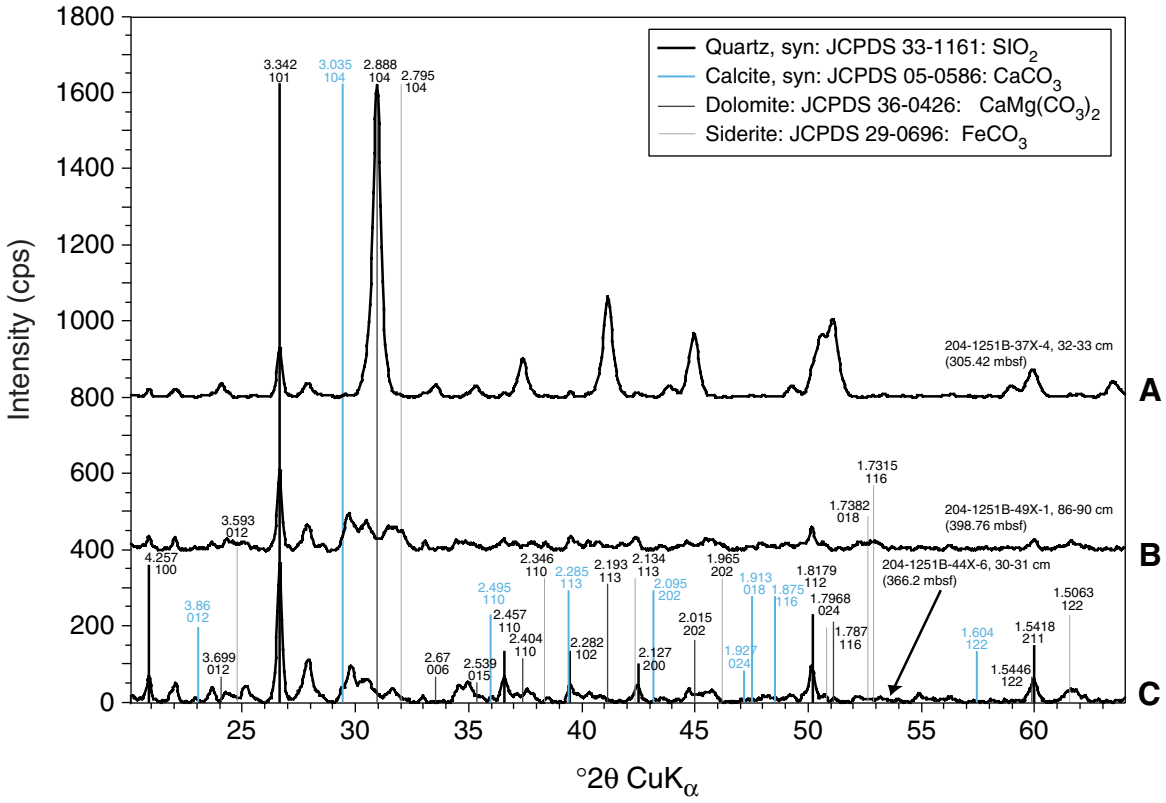

Figure F11. Age-depth plot for Hole 1251B based on diatom and calcareous nannofossil bioevents. The detailed age and depth of control points are given in Table T3, p. 96 (1–10).

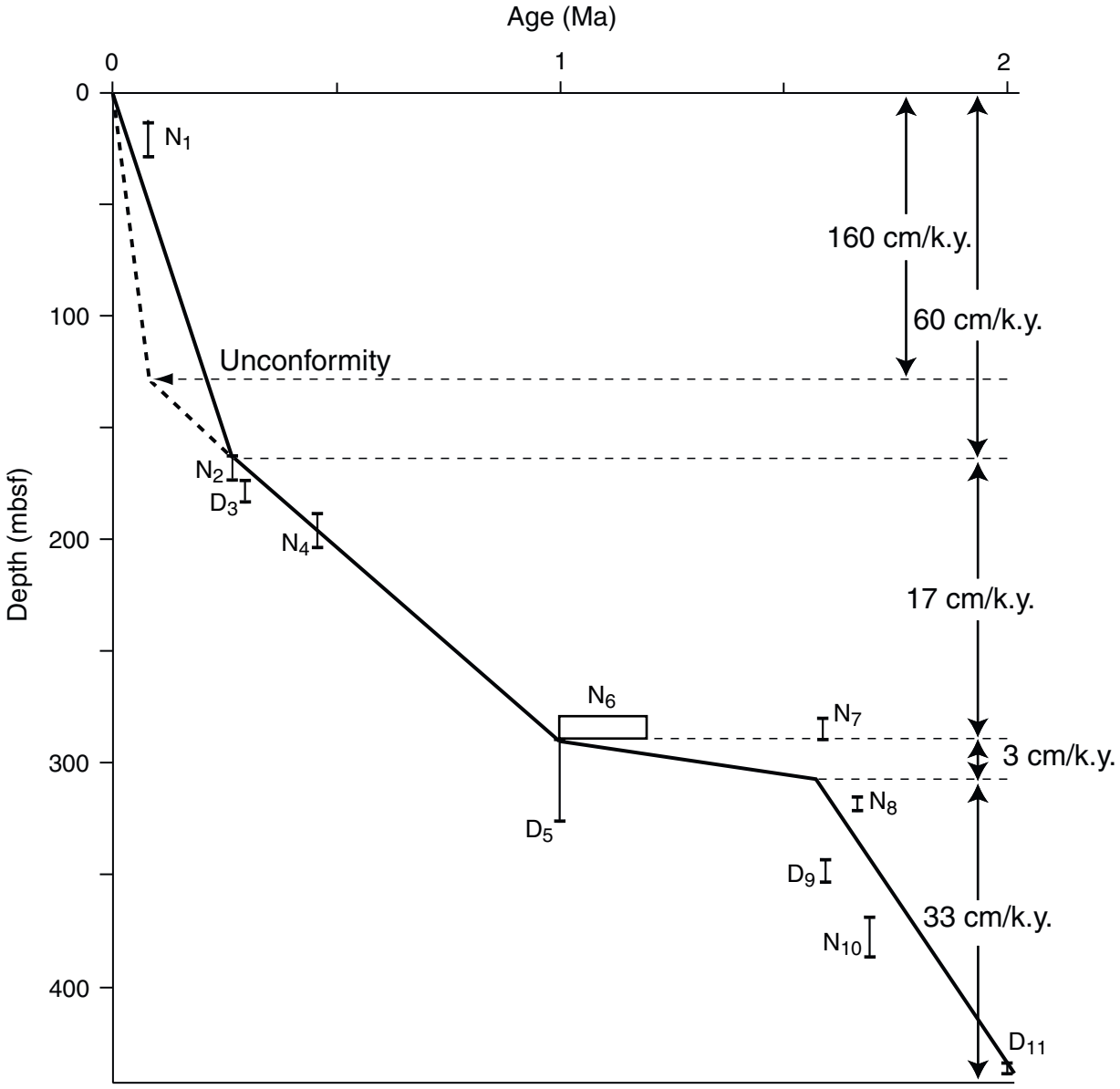

Figure F12. Concentration profiles of various dissolved species in pore waters from Holes 1251B (red circles), 1251C (green triangles), 1251D (blue squares), and 1251E (open triangles). DOC = dissolved organic carbon. (Continued on next page.)

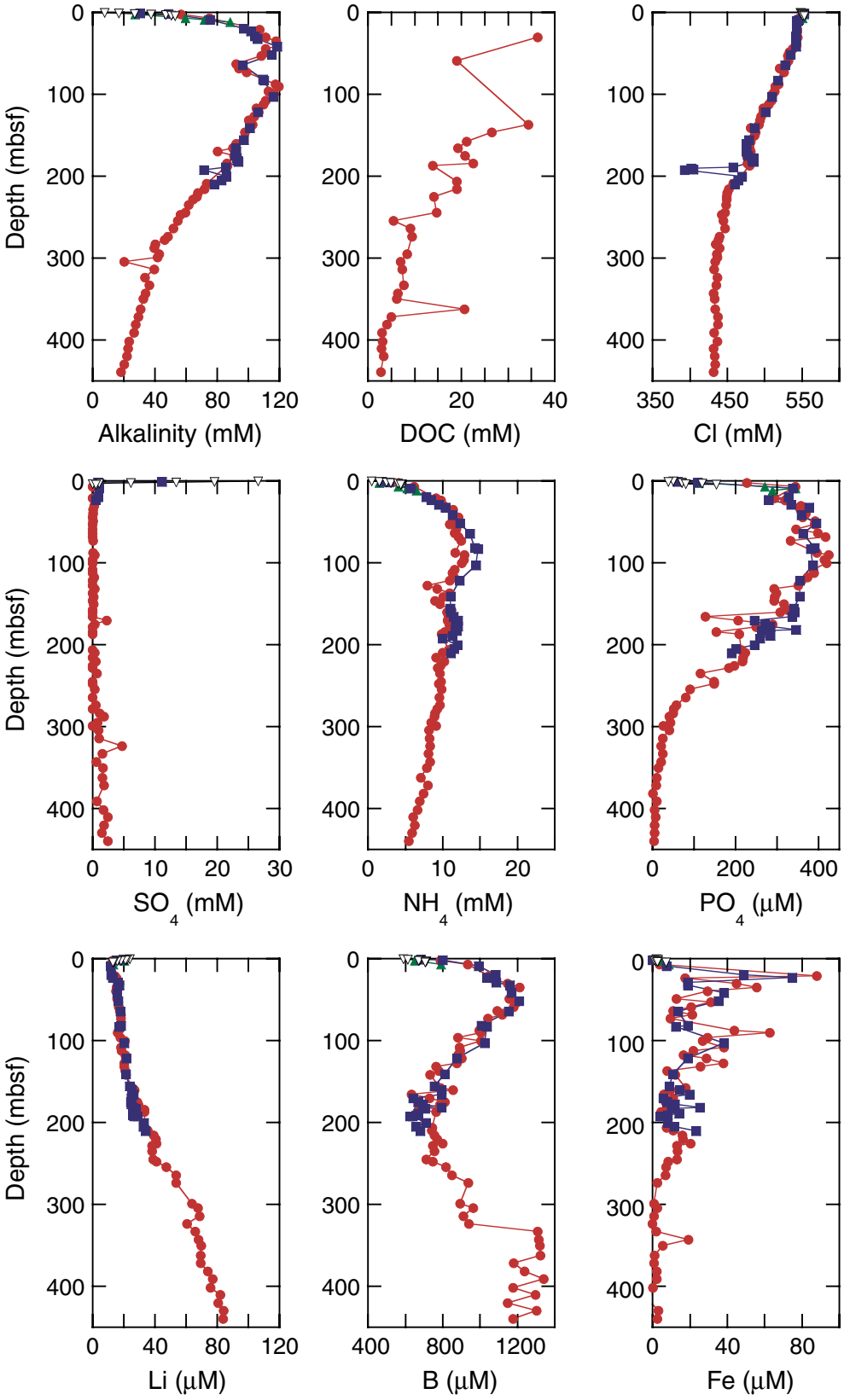

Figure F12 (continued).

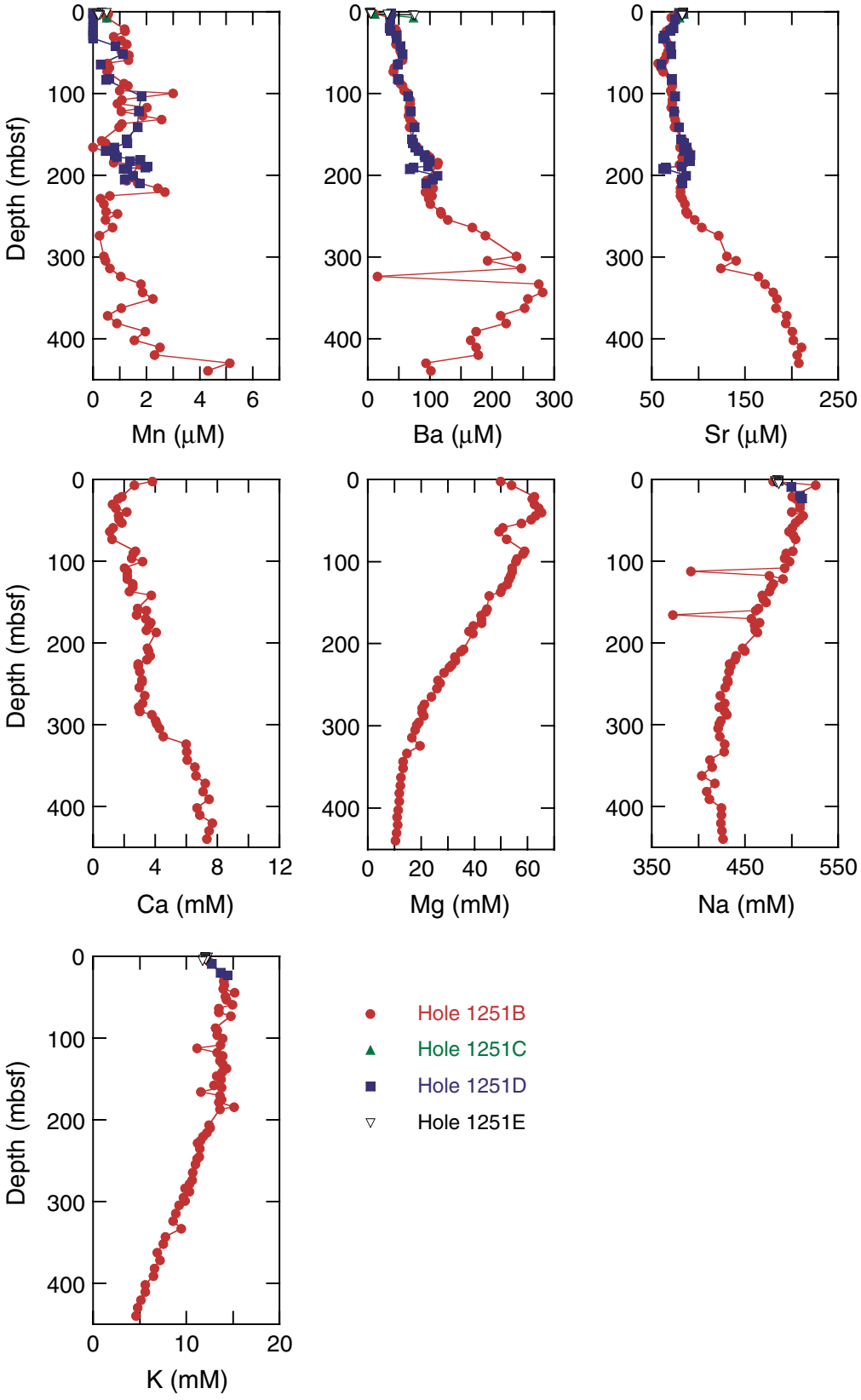

Figure F13. Distribution of dissolved chloride and lithium in pore waters from Holes 1251B and 1251C. The increase in lithium and decrease in chloride with depth suggest a fluid source within the deep-seated sediments of the accretionary complex.

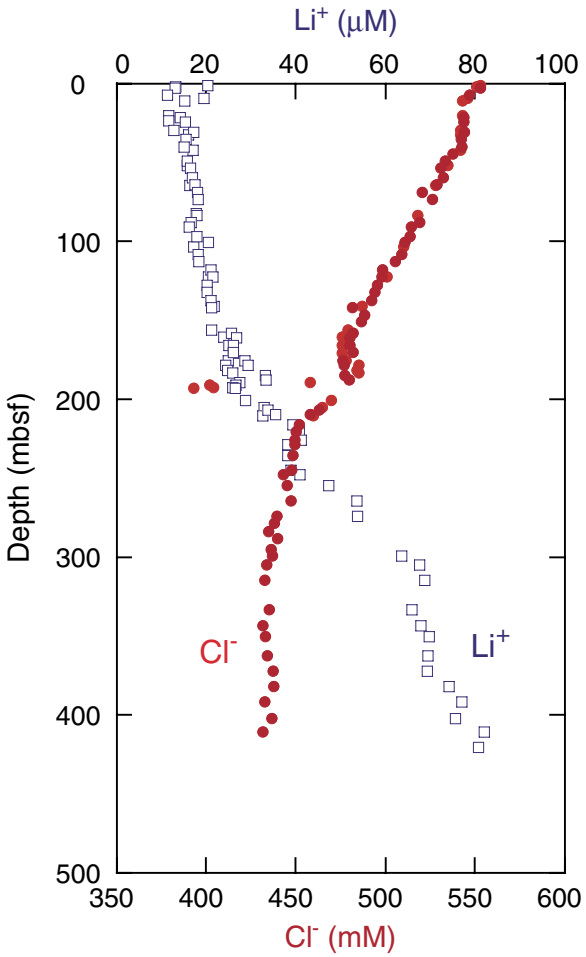

Figure F14. Comparison of chloride distribution (solid circles) with sites drilled during Leg 146 (open circles) at Site 1251. All sites show a decrease in dissolved chloride with depth, reflecting the influence of a deep-seated fluid source. Site 888, which was drilled west of the deformation zone during ODP Leg 146, represents a background chloride distribution (Kastner et al., 1995). Estimates of gas hydrate amounts based on deviations in chloride (Cl^-) concentration from the linear Cl^- decrease reveal that gas hydrate occupies ~20% of the pore space in sediments at the bottom of the GHSZ. The lack of any other significant deviation in chloride concentration indicates that there is very little gas hydrate present above the deep hydrate layer just above the bottom-simulating reflector (BSR).

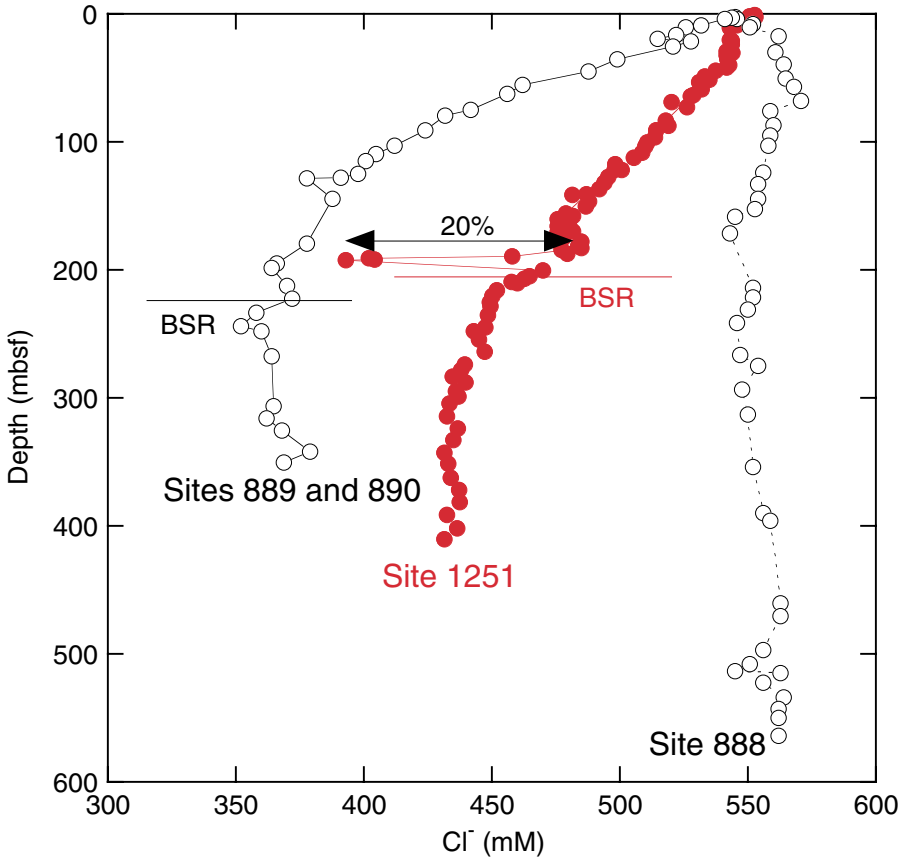

Figure F15. Sulfate (SO_4^{2-}) and methane (CH_4) concentration profile at in the upper 15 mbsf at Site 1251. Sulfate data are from Hole 1251E, where high-resolution sampling occurred in conjunction with microbiological studies. Interstitial methane concentrations are from headspace data from Hole 1251C (see **"Organic Geochemistry,"** p. 16). The sulfate profile is linear through the majority of the sulfate reduction zone, with curvature at both the top and bottom of the sulfate reduction zone. This linear portion of the curve was used to calculate upward methane flux at Site 1251, based on the shown linear regression. The sulfate/methane interface (SMI) is also shown at a depth of ~4.5 mbsf, where sulfate concentration falls below 1 mM; interstitial methane concentrations were depth shifted ~30 cm to correspond to the sulfate data.

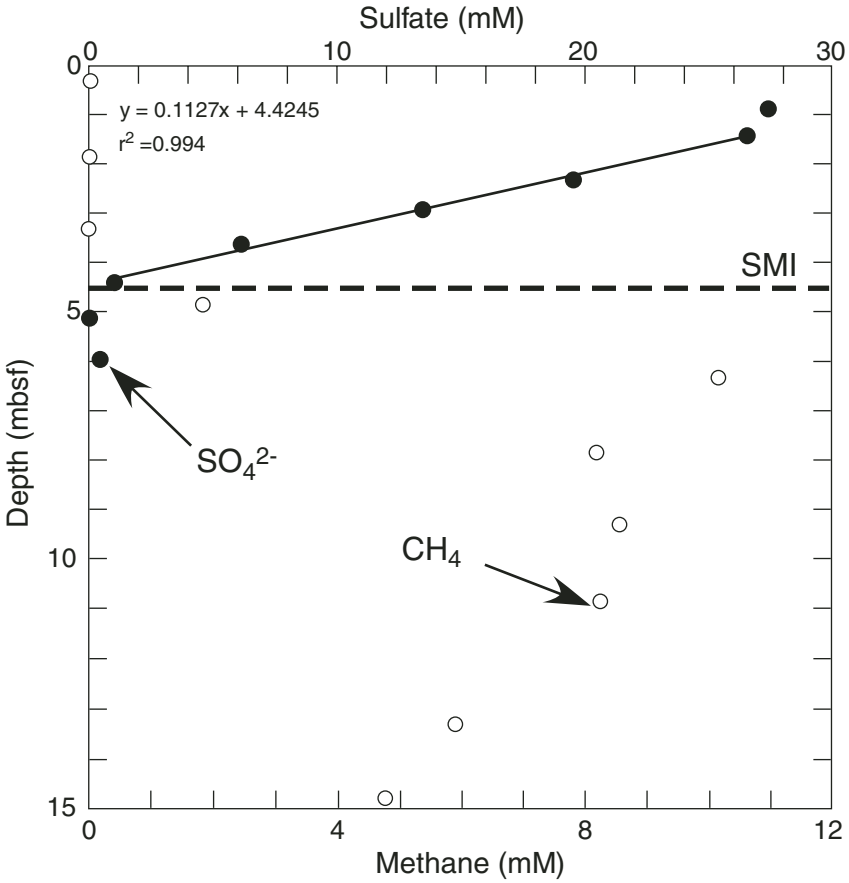

Figure F16. Dissolved sulfate (SO_4^{2-}) and barium (Ba^{2+}) profiles in the upper 6 mbsf at Site 1251, illustrating barium remobilization at the zone of sulfate depletion.

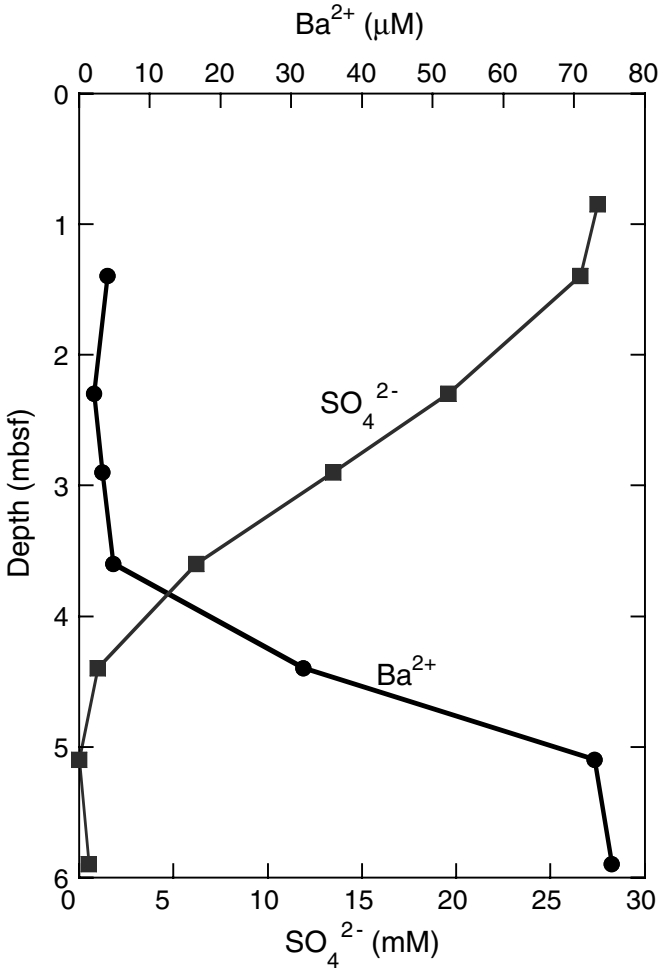

Figure F17. Downcore variations in MS data (see **"Physical Properties,"** p. 19), iron content, and lithostratigraphic units showing a correspondence between high iron content and presence of sulfide minerals in the sediments at Site 1251. The dotted line in the iron distribution corresponds to the dissolved iron profile at Site 1244, which also shows high variability within the upper sulfide-rich sediments (see **"Interstitial Water Geochemistry,"** p. 13, in the "Site 1244" chapter).

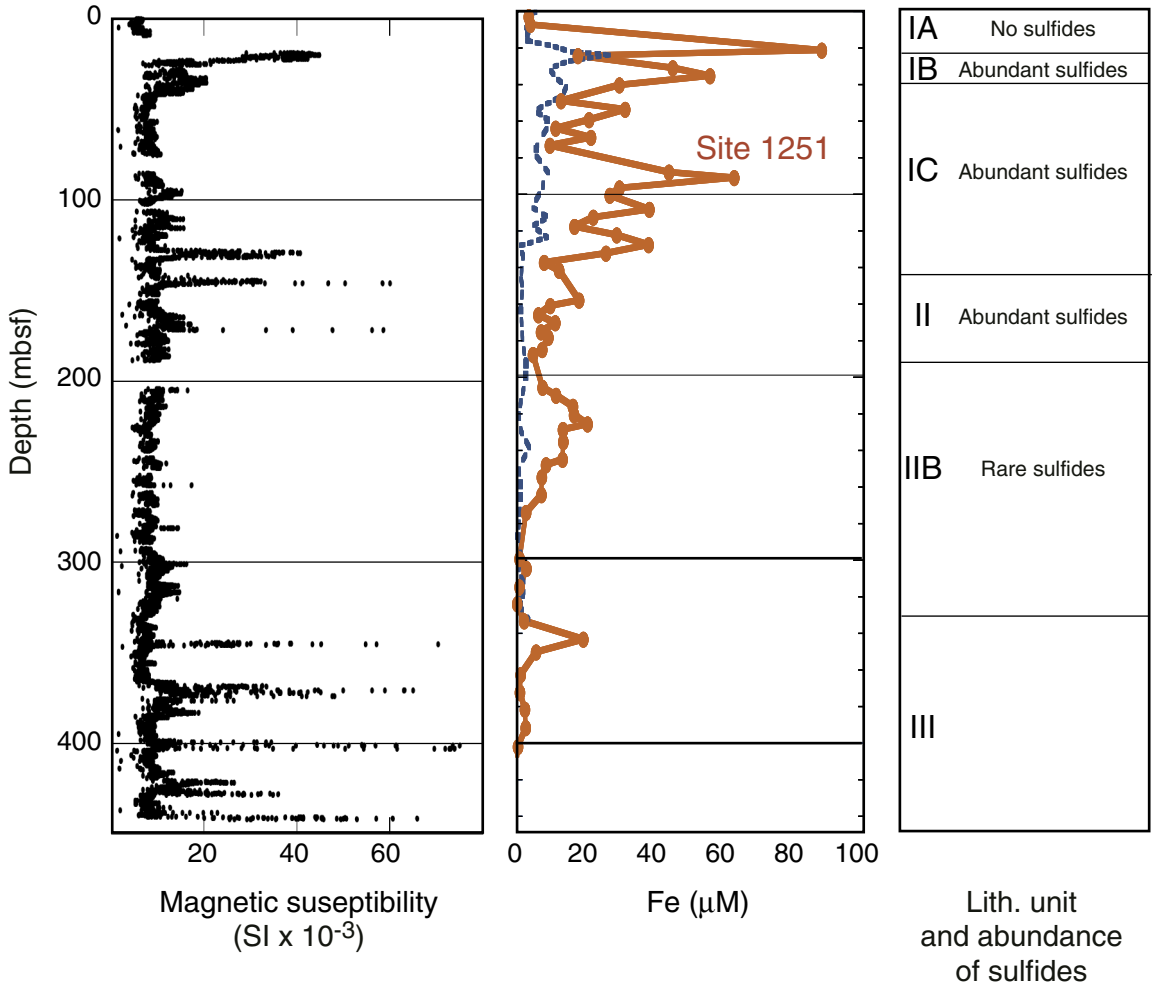

Figure F18. Concentrations of C_1, C_2, $C_{2=}$, and C_3 from headspace method vs. depth at Site 1251.

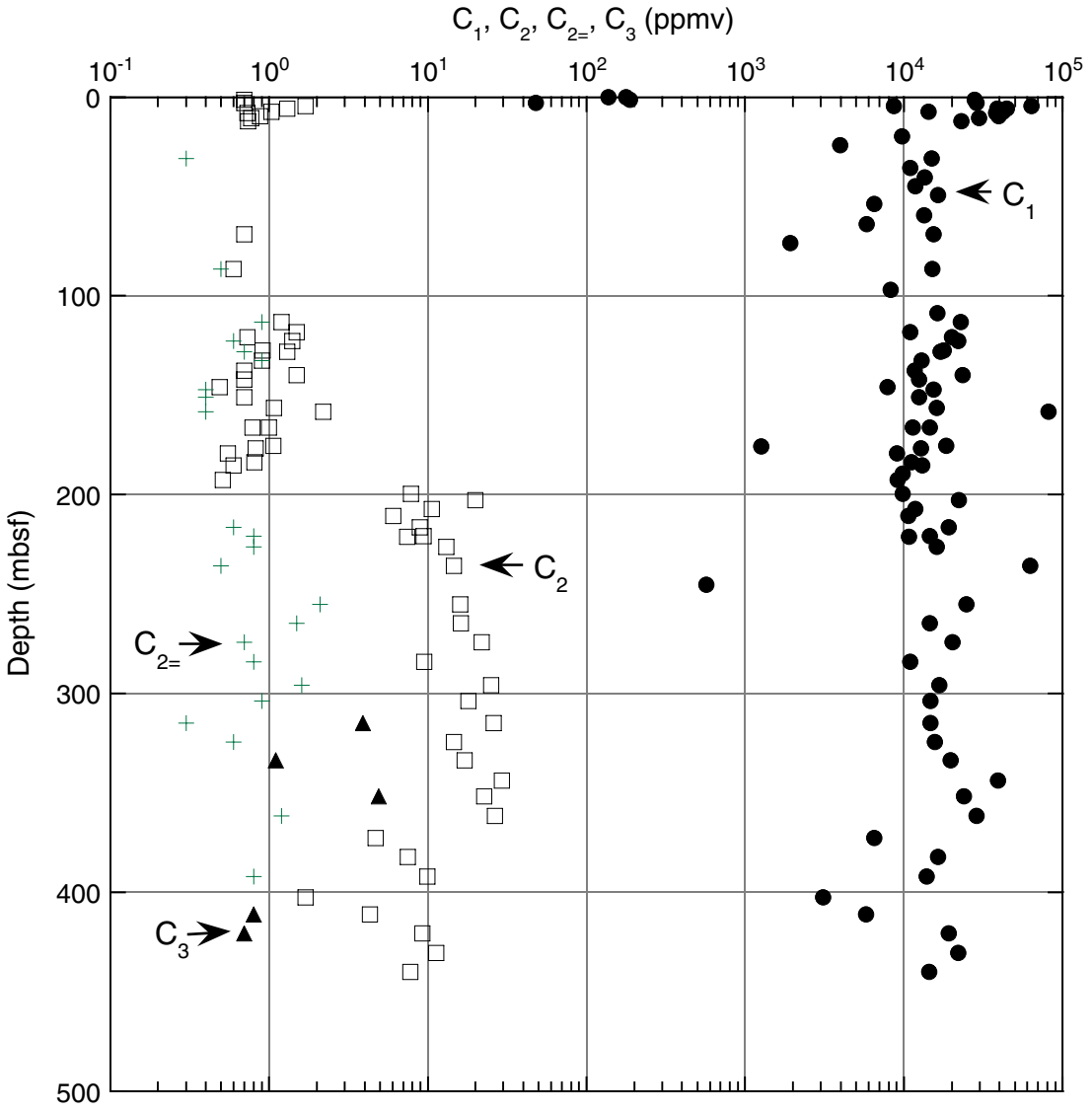

Figure F19. Dissolved residual methane (CH_4) and sulfate (SO_4^{2-}) in pore water. Depths for Hole 1251B have been adjusted downward by 3.7 m to match the methane profile in Hole 1251C. The methane concentration increases at the depth where the sulfate concentration is depleted.

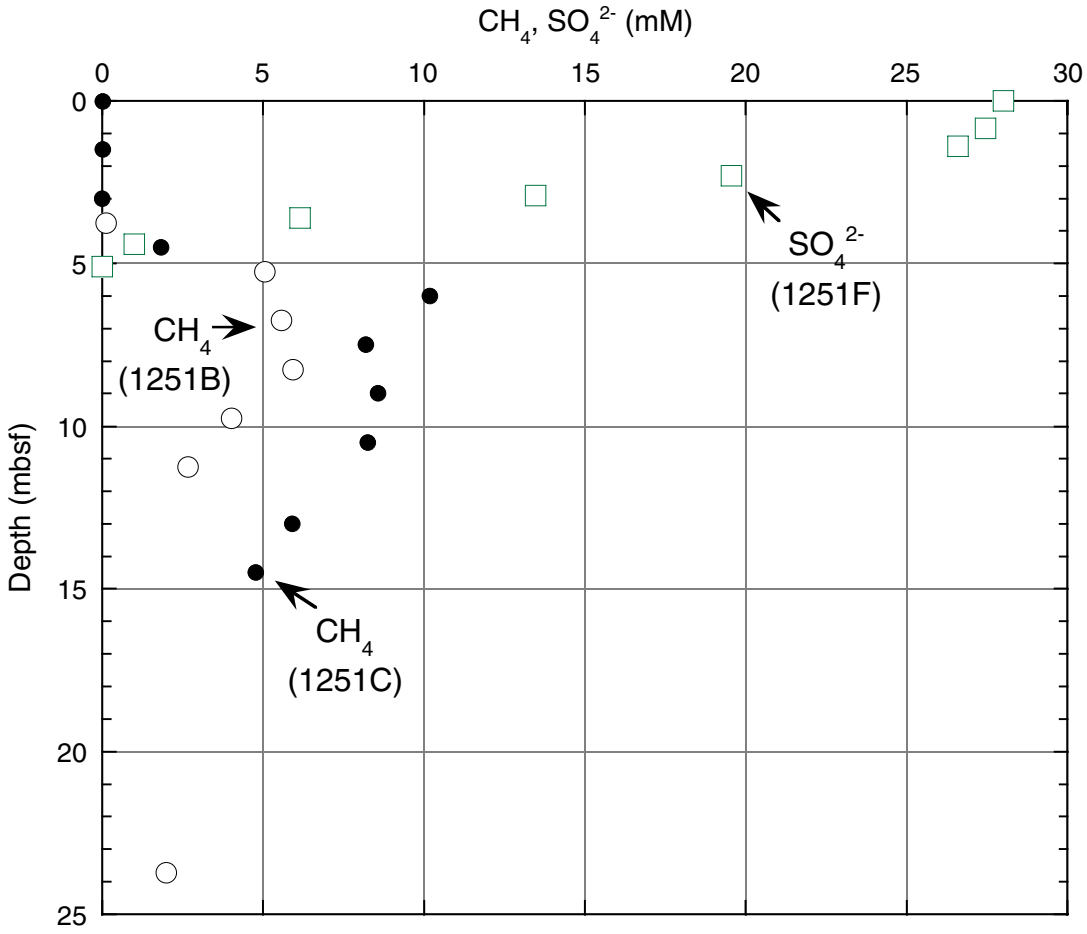

Figure F20. Concentrations of C_1, C_2, C_3, and i-C_4 in core void gas vs. depth for Site 1251. BSR = bottom-simulating reflector.

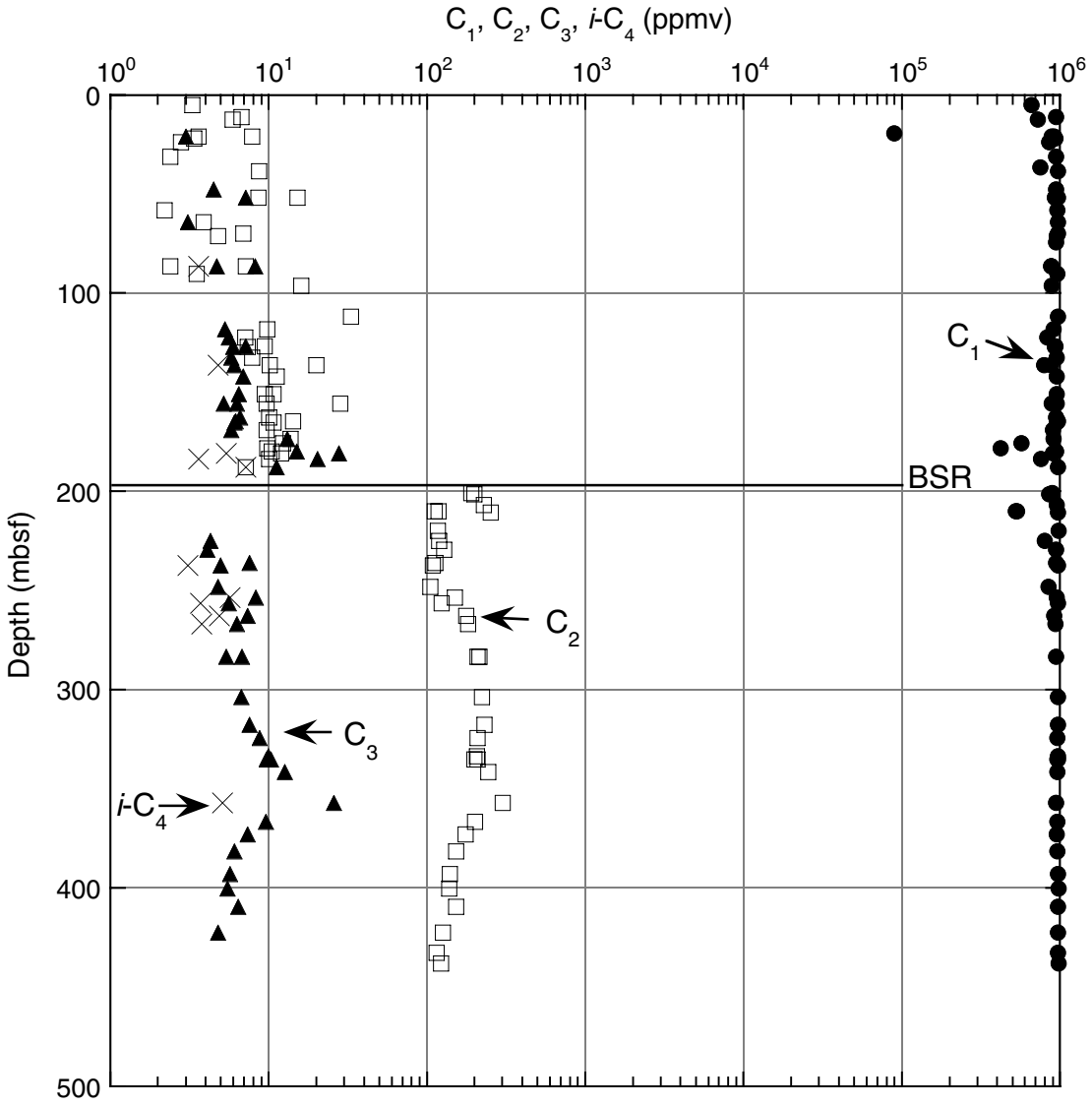

Figure F21. C_1/C_2 ratio vs. depth for Site 1251. HS = headspace gas, PCS = pressure core sampler, BSR = bottom-simulating reflector, VAC = vacutainer.

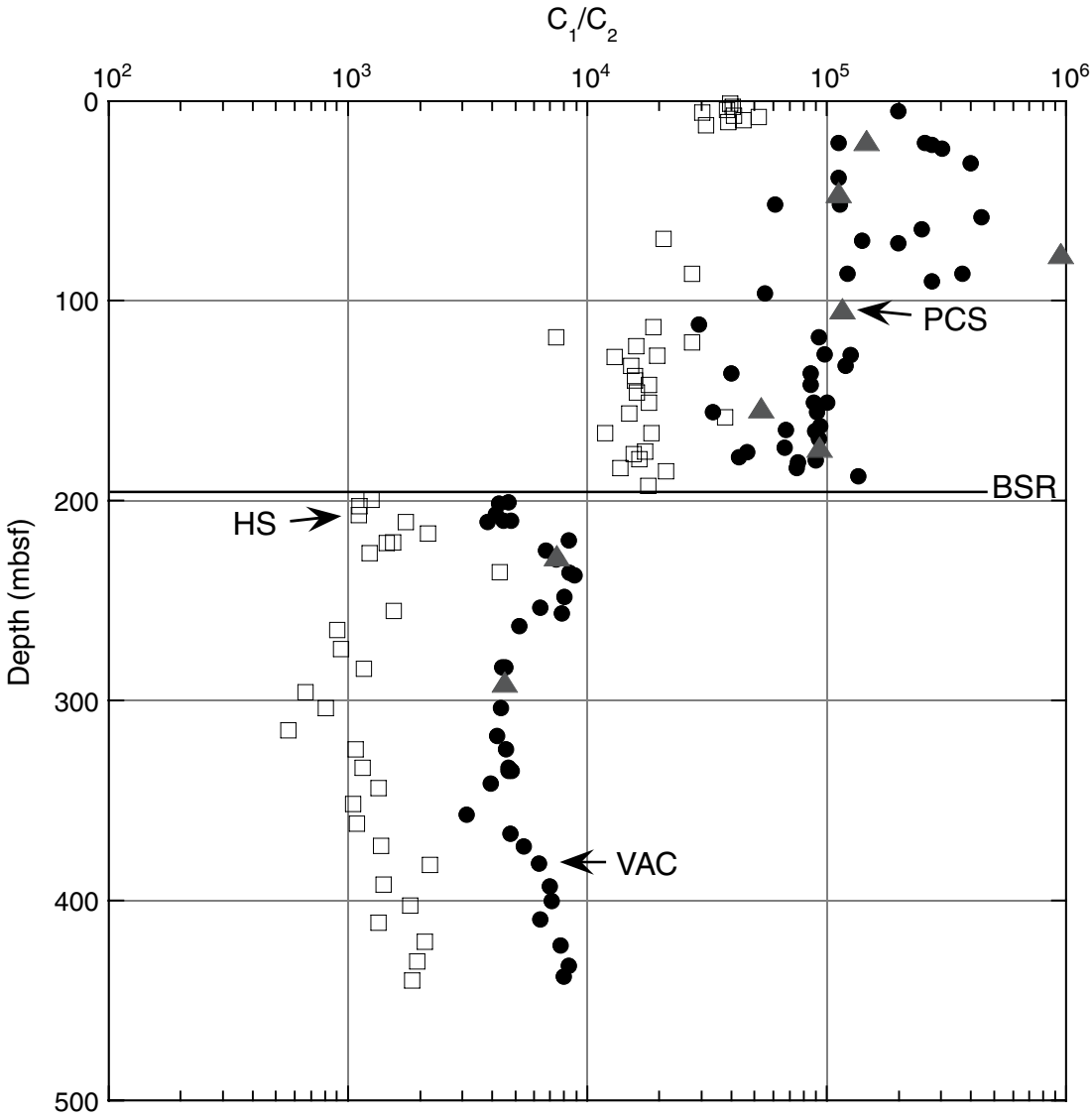

Figure F22. Downhole variation in carbonate carbon (IC), organic carbon (OC), total nitrogen (TN), and total sulfur (TS) and C/N ratios in sediments from Hole 1251B.

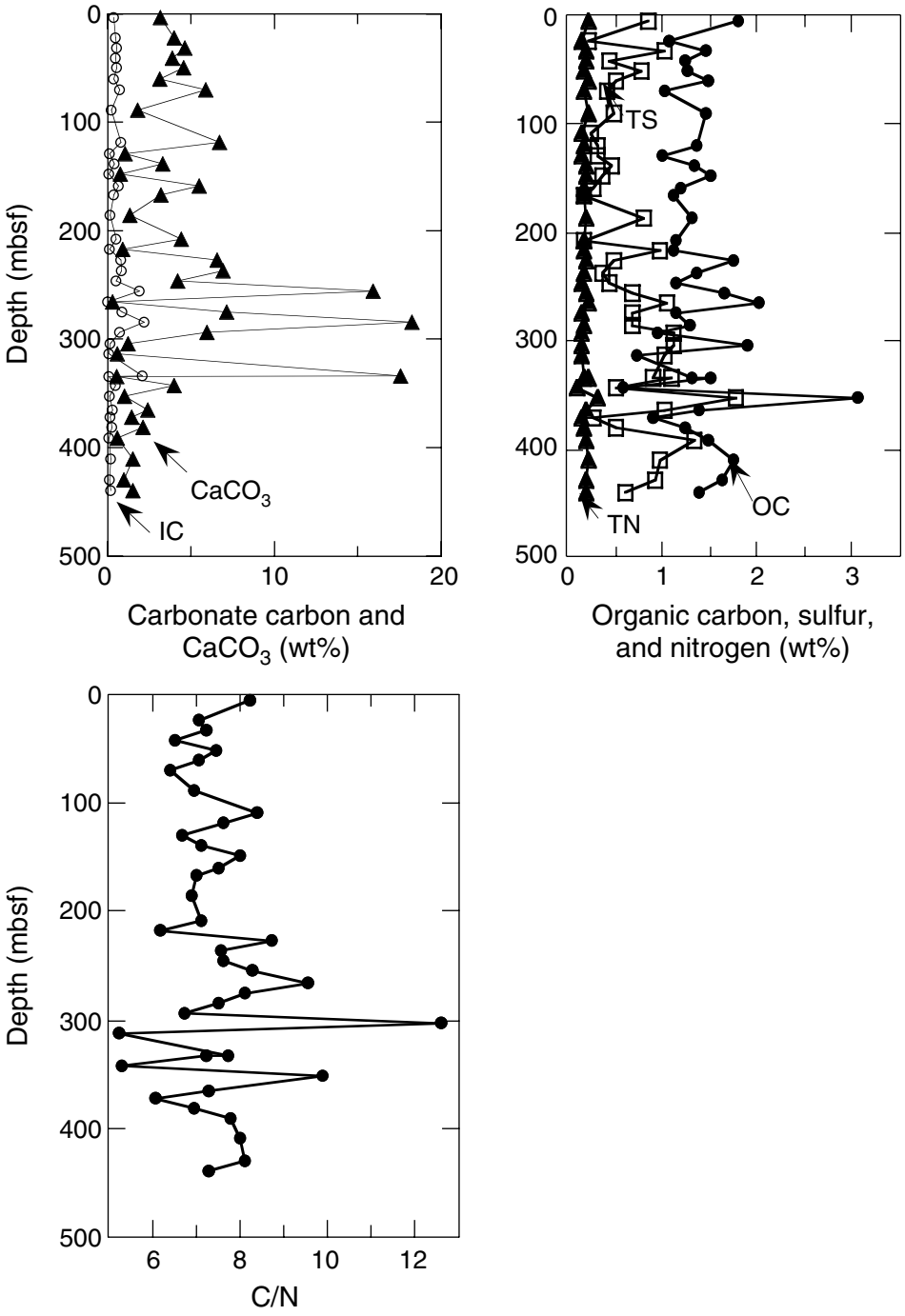

Figure F23. Fluorescence micrograph of "peachy orange slime" from interval 204-1251B-1H-1, 47–48 cm, stained with DAPI (4,6-diamindino-2-phenylindole). Individual cells are 1–2 µm in diameter.

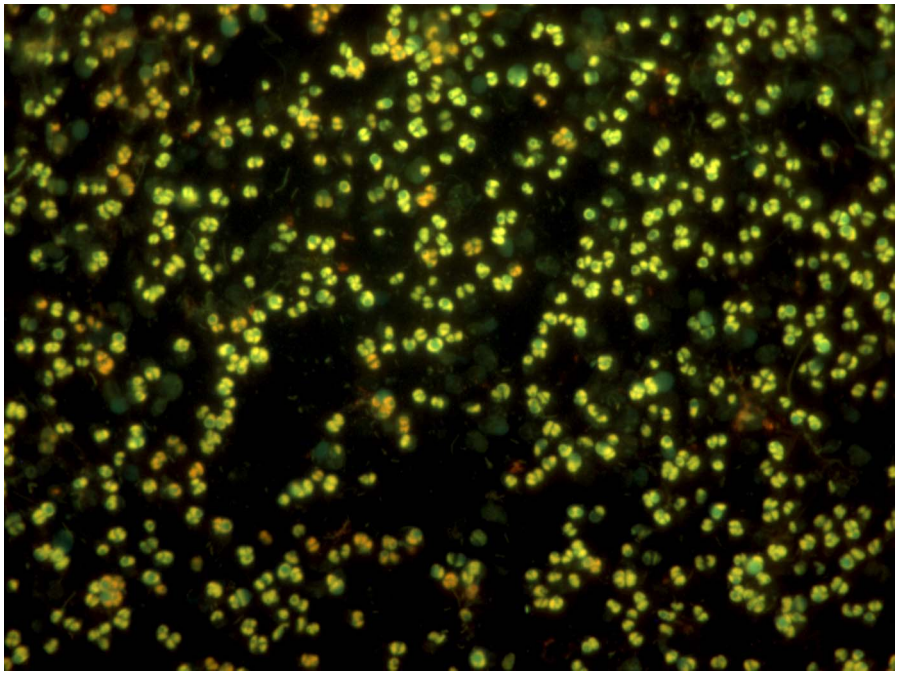

Figure F24. A. Example of a cold anomaly in an IR image associated with disseminated hydrate. **B.** Close-up example of IR images and an associated cold-spot anomaly of $\Delta T = -1.5$°C. The images were taken from Section 204-1251B-22H-4 at 178.4–178.9 mbsf. The ΔT is the difference between an average background temperature and the minimum temperature in the cold-spot anomaly (see Table T12, p. 110).

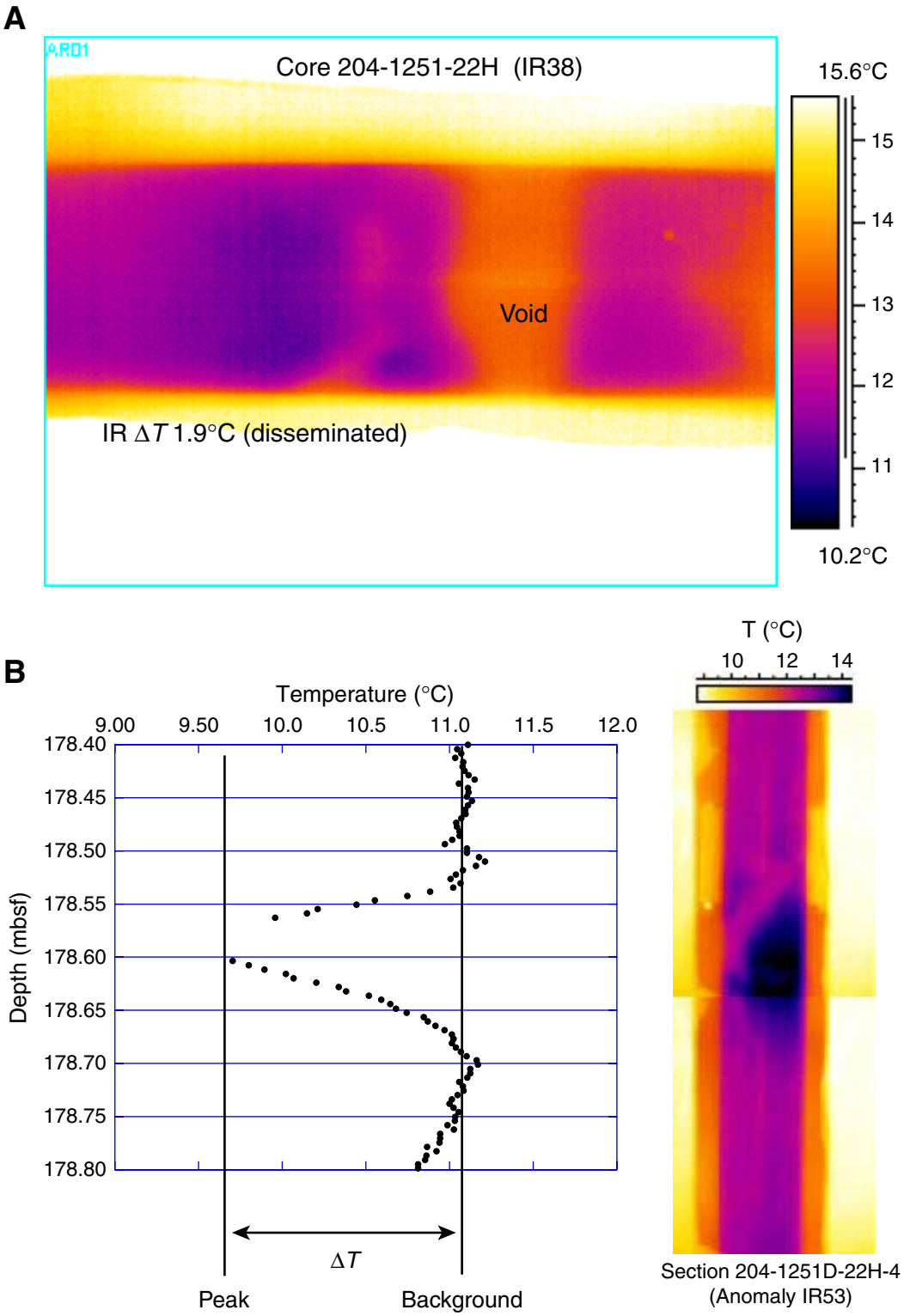

Figure F25. Downcore temperatures from IR scans of Holes 1251B and 1251D. Strong positive anomalies in cores from both holes are sun illumination artifacts. The major negative anomaly in Hole 1251D is from hydrate recovered near the BSR that was not recovered in Hole 1251B (see also Fig. **F26,** p. 67). APC = advanced piston corer, BSR = bottom-simulating reflector, XCB = extended core barrel.

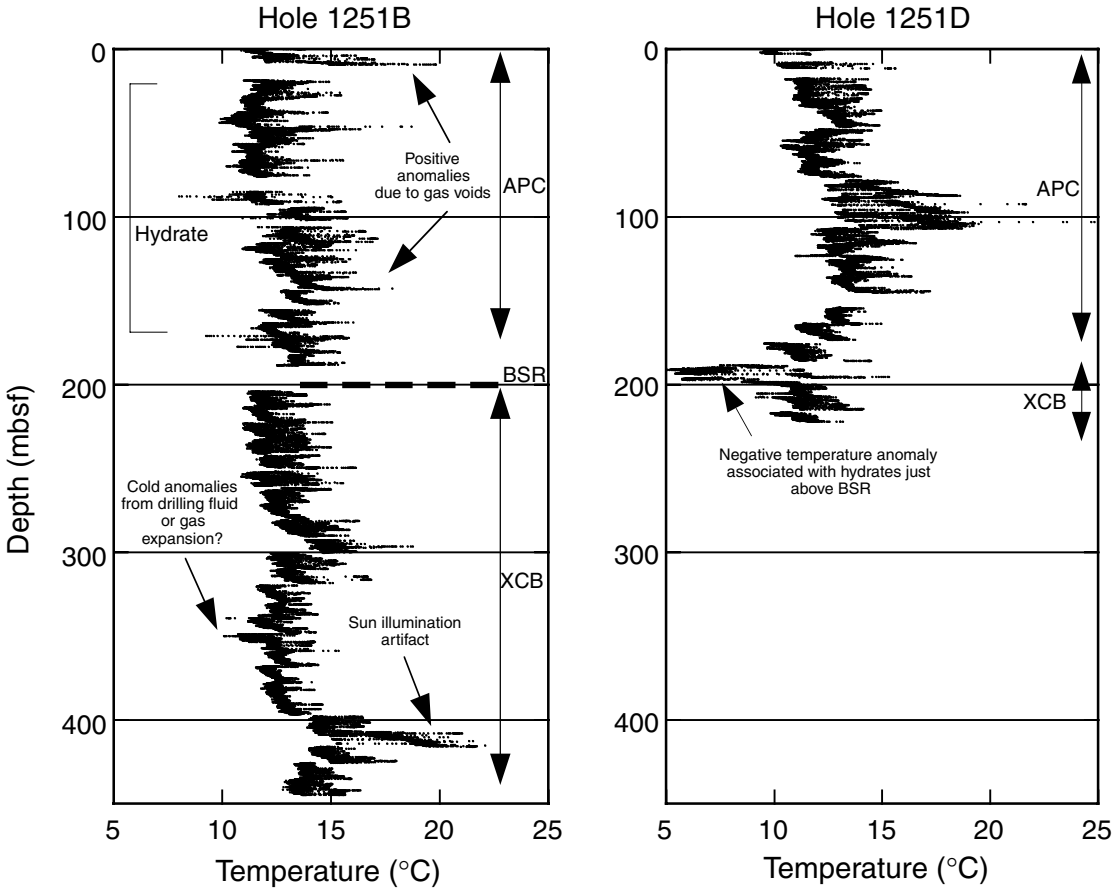

Figure F26. Negative temperature anomalies summarized graphically for Holes 1251B and 1251D. The major anomaly near the bottom-simulating reflector (BSR) in Hole 1251D is not seen in Hole 1251B because no core was recovered from that zone in Hole 1251B.* = locations of suspected hydrate samples

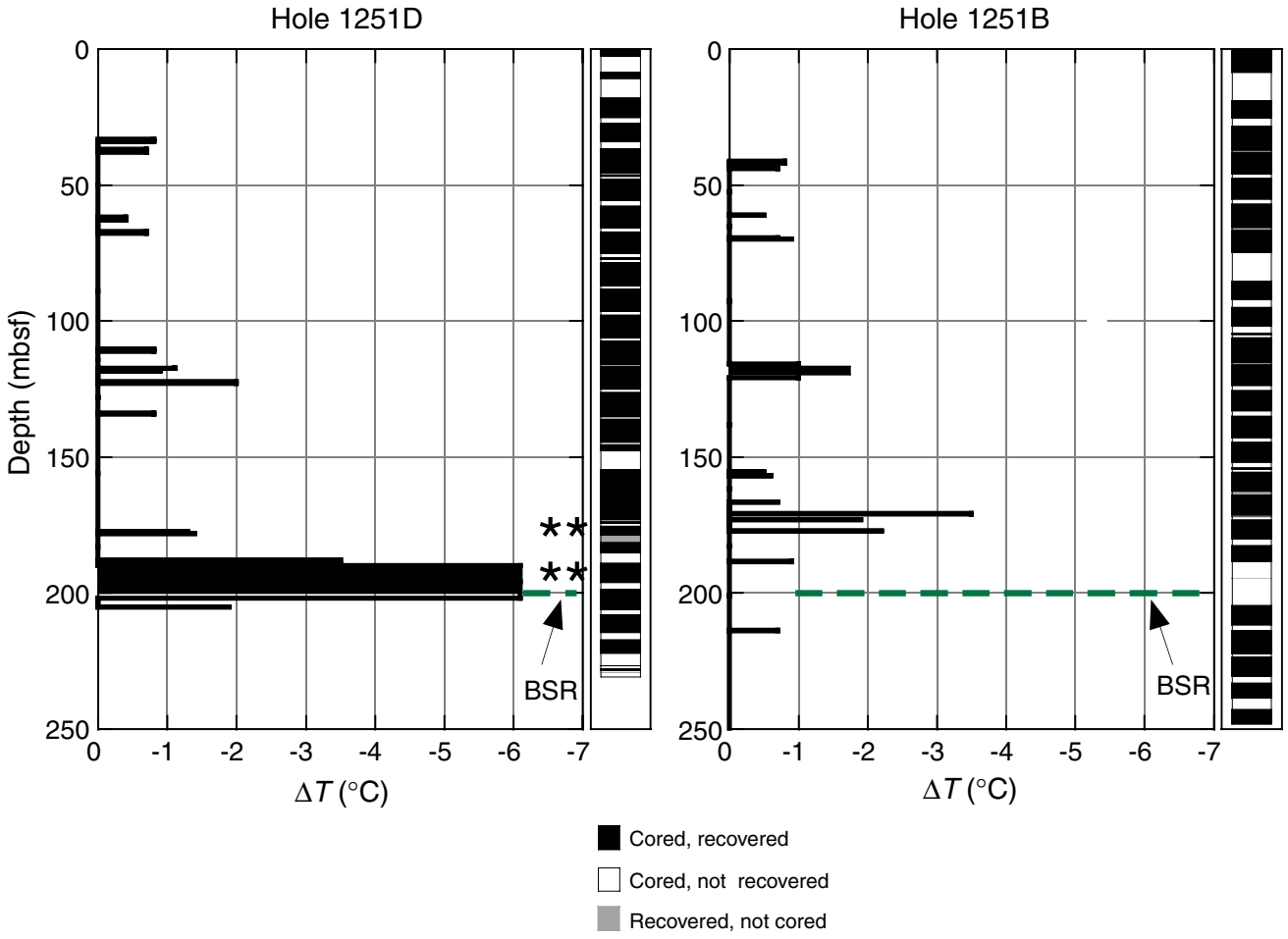

Figure F27. Detailed comparison of downcore temperatures from IR scans of depth intervals cored with the advanced piston corer (APC) (Hole 1251B) and extended core barrel (XCB) (Hole 1251D). XCB temperatures are ~2.5°C lower than the APC temperatures. This difference cannot be explained by differences in ambient catwalk temperature (see **"Infrared Scanner,"** p. 20, for details).

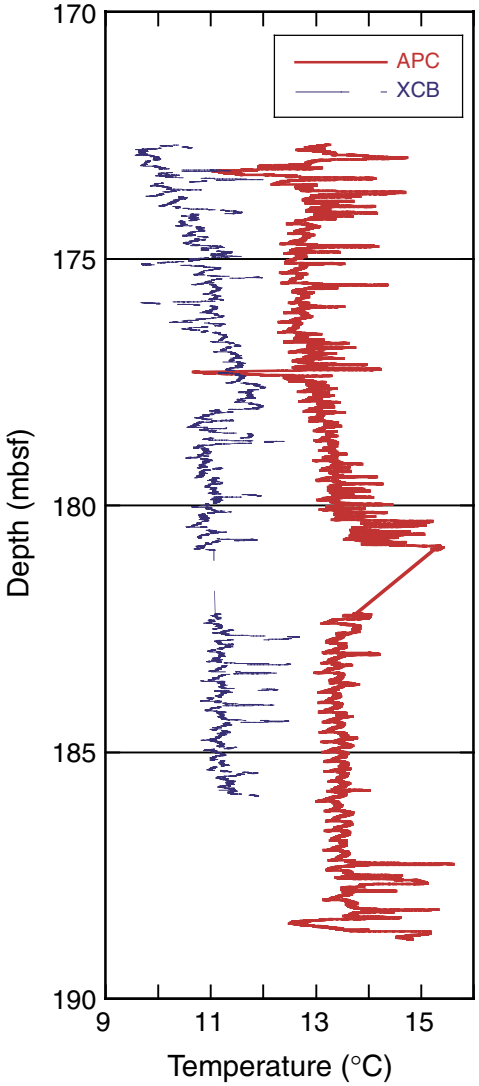

Figure F28. Detailed comparison between downcore temperature from infrared (IR) scans at the bottom-simulating reflector (BSR) and downhole chlorinity values derived from IW samples in Hole 1251D.

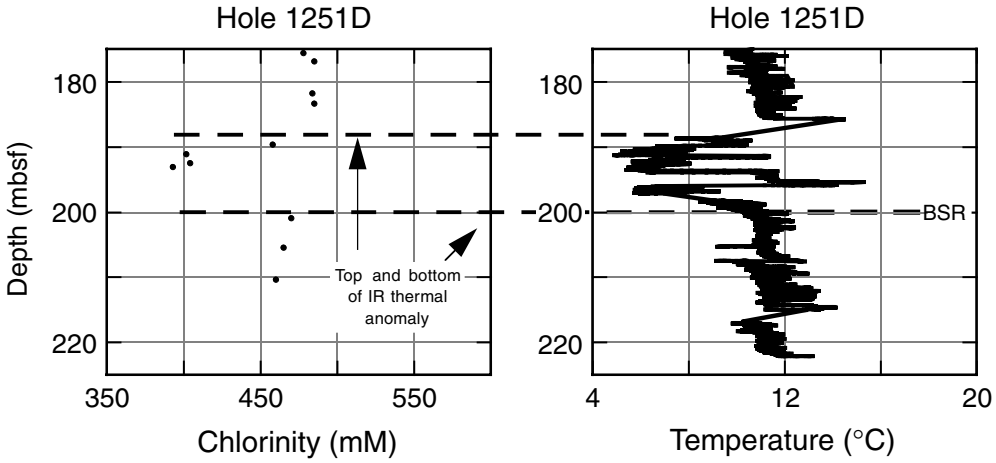

Figure F29. Summary of physical property measurements at Holes 1251B. Lithostratigraphic units are indicated (see **"Lithostratigraphy,"** p. 3). LWD = logging while drilling, GRA = gamma ray attenuation, MAD = moisture and density.

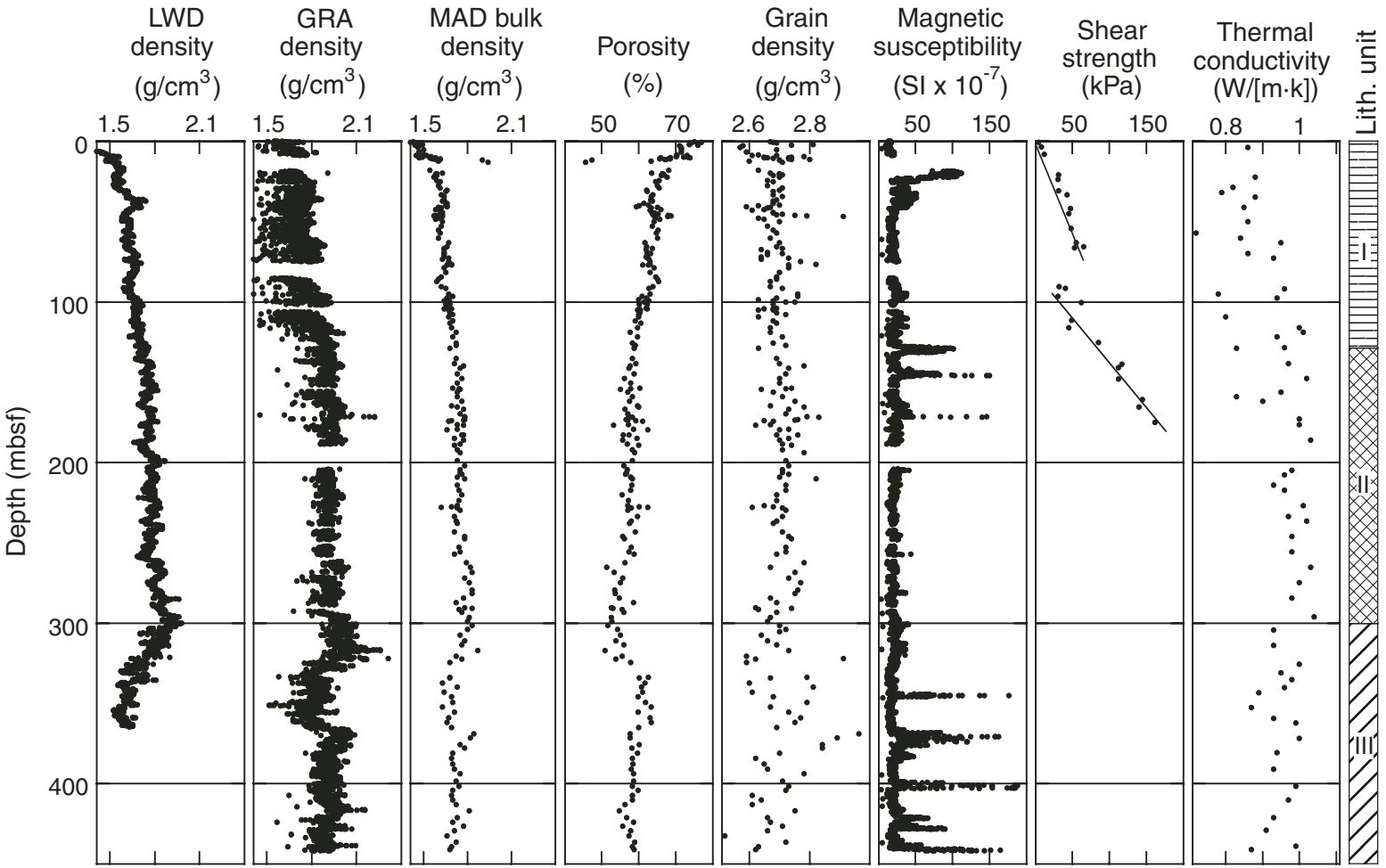

Figure F30. Correlation between the seismic record and physical properties (logging-while-drilling [LWD], MAD, and porosity measurements). Lithostratigraphic Units I–III are indicated.

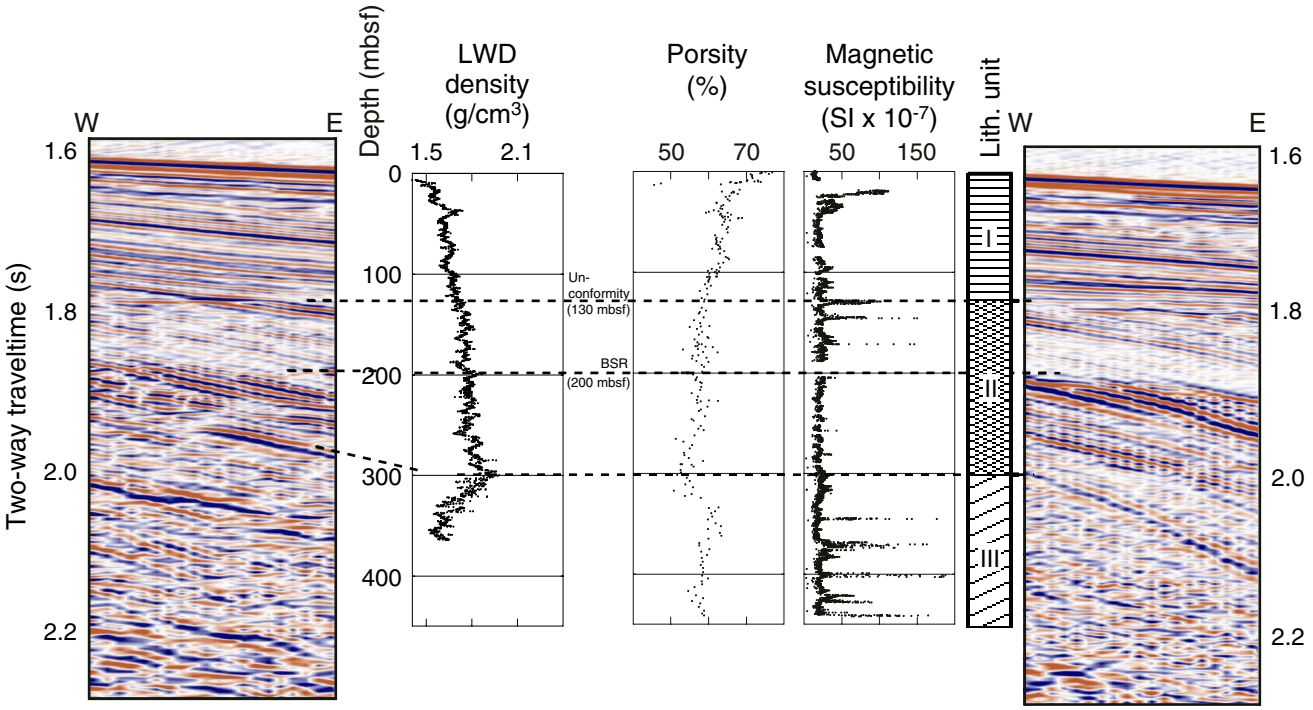

Figure F31. Comparison between the MS measured by the loop sensor on the on the multisensor track (MST) and the higher resolution point sensor in the magnetic susceptibility system field unit (MSF2) for the anomaly at 130 mbsf. The related sedimentological record and several images form the X-ray line scanner (see **"Operations,"** p. 2, in the "Site 1249" chapter).

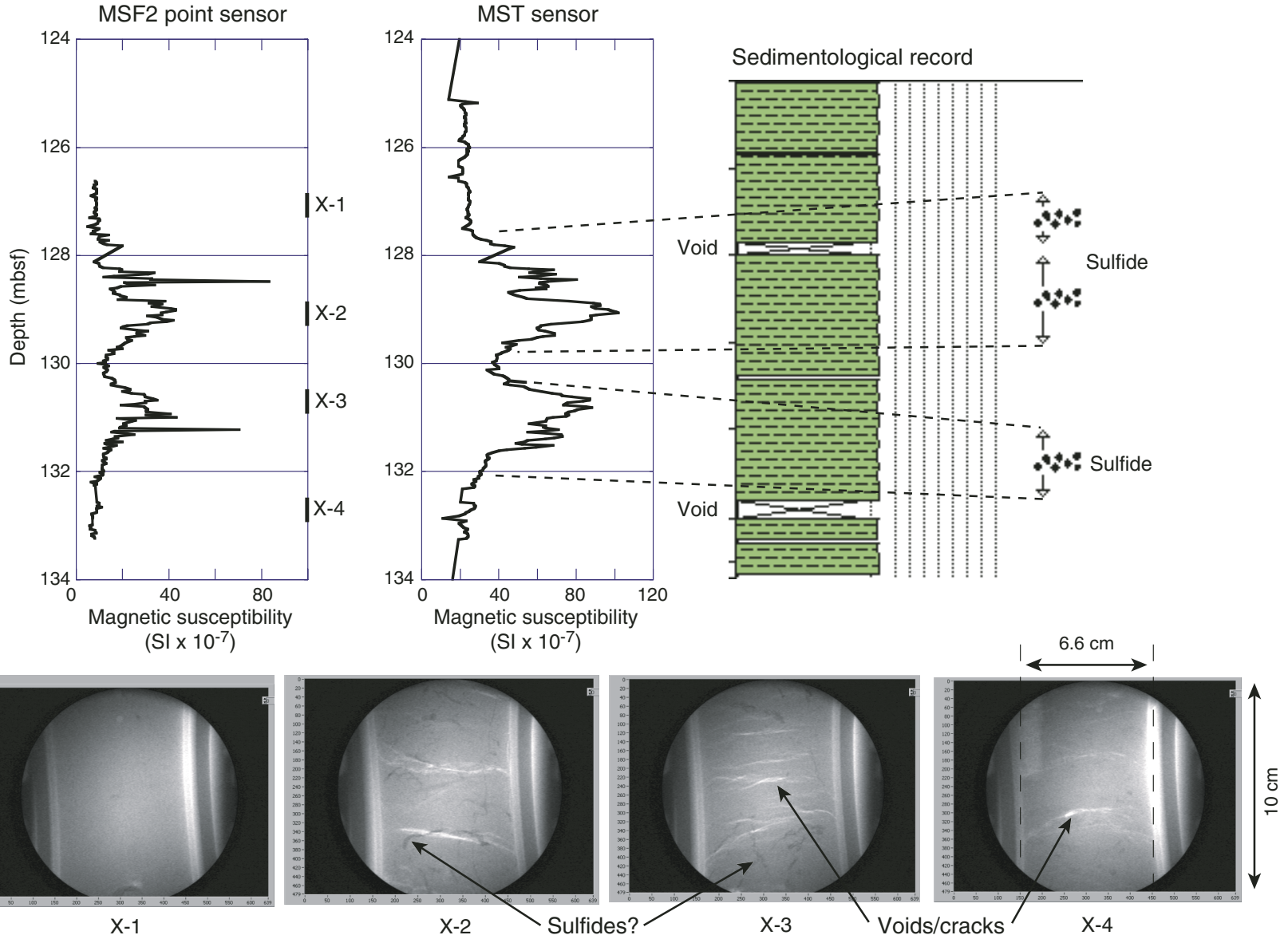

Figure F32. A. Noncontact resistivity (NCR) in Hole 1251B. The large positive excursions are caused by gas cracks. Note that no reliable data are available between 90 and 173 mbsf because the sensor was moved. **B.** NCR data from 0 to 9 mbsf show the effect of crack formation below ~3 mbsf.

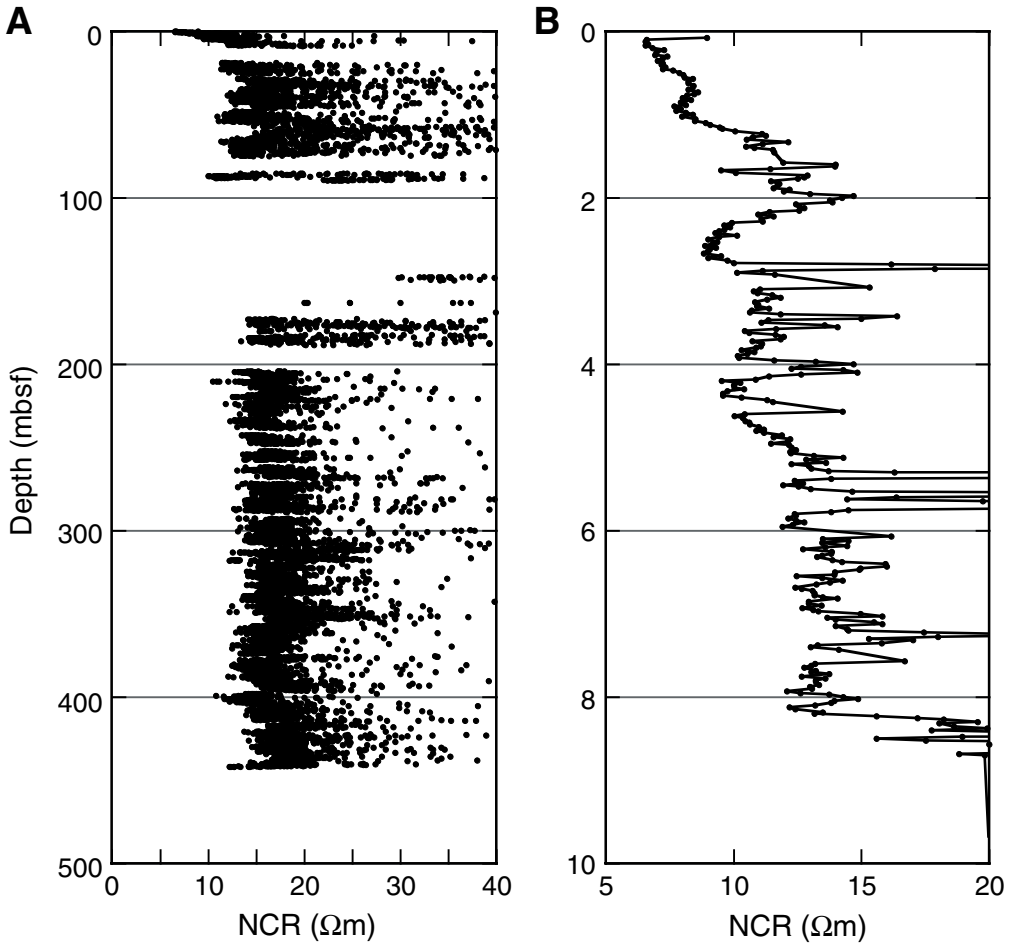

Figure F33. Comparison of normalized bulk density (Norm. BD) and normalized thermal conductivity (Norm. TC).

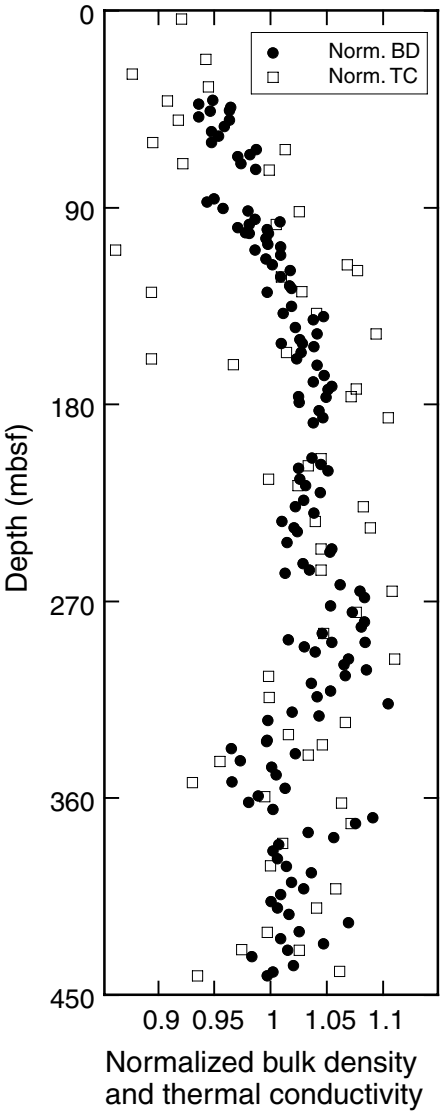

Figure F34. Raw data for estimating in situ temperatures. **A.** APCT tool data. Only the portion of data immediately before, during, and immediately after penetration of the probe into the subsurface is shown. For an example of the entire temperature history of a deployment, see Figure **F15,** p. 82, in the "Explanatory Notes" chapter. For Core 204-1251D-20H, data acquisition stopped while the APCT tool was in the seafloor, so recovery was not recorded. The identification number of the core with which the APCT tool was deployed is indicated in the upper left corner of the graph. (Continued on next page.)

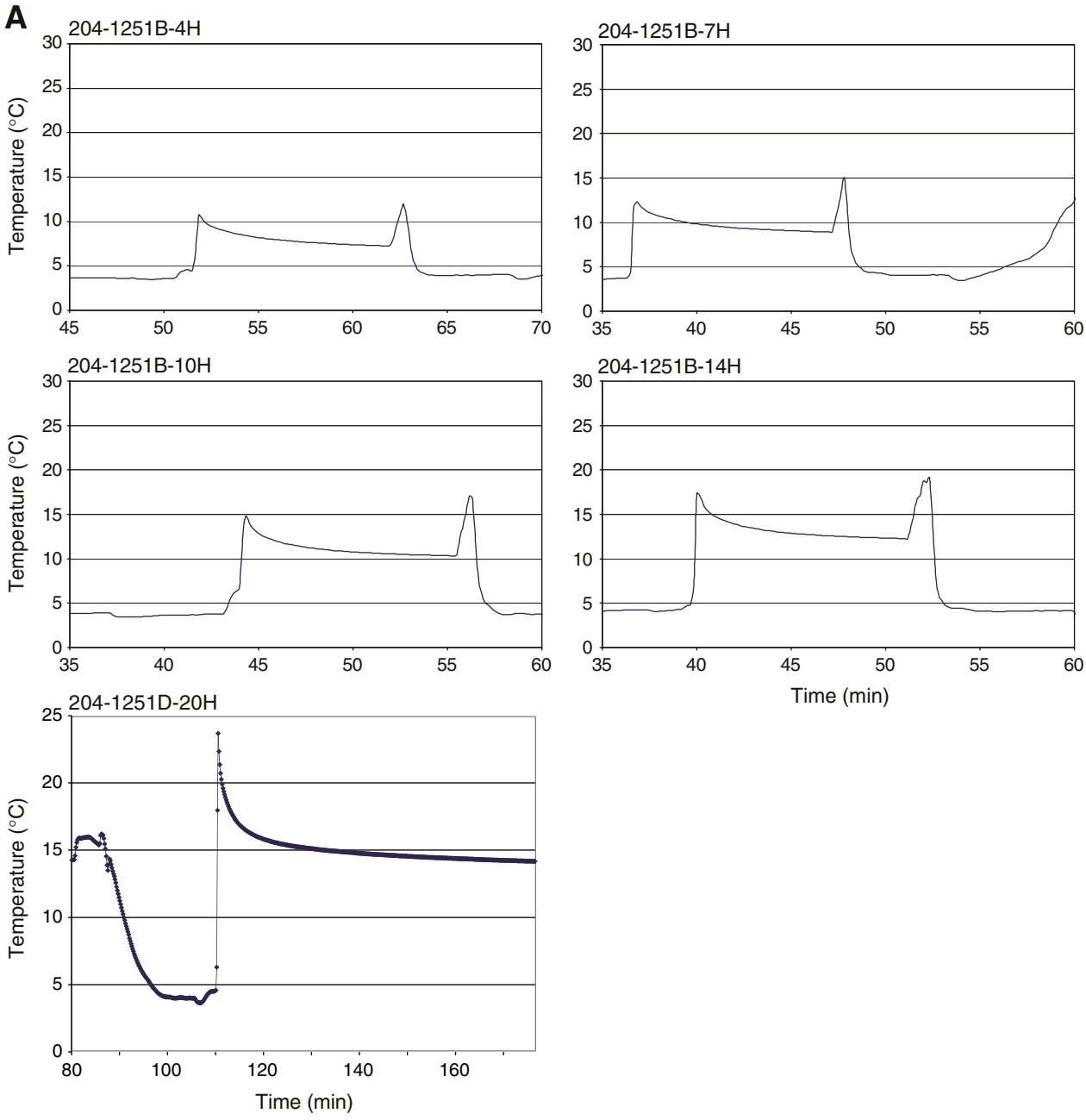

Figure F34 (continued). B. DVTPP temperature and pressure data. The ODP identification for cores preceding and following tool deployment are indicated.

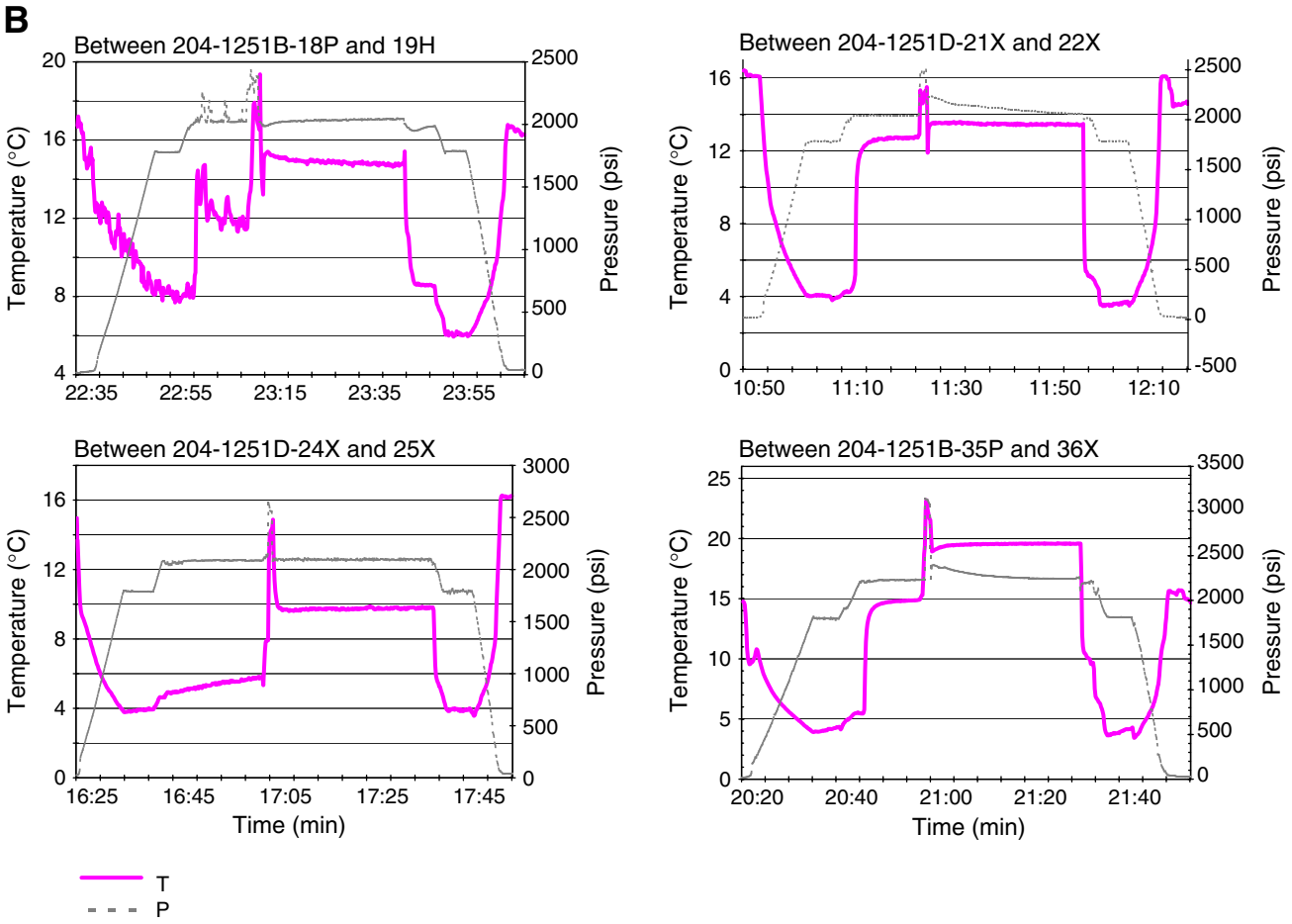

Figure F35. Subsurface temperatures plotted vs. depth beneath the seafloor at Site 1251. Red data points were excluded from calculation of the thermal gradient.

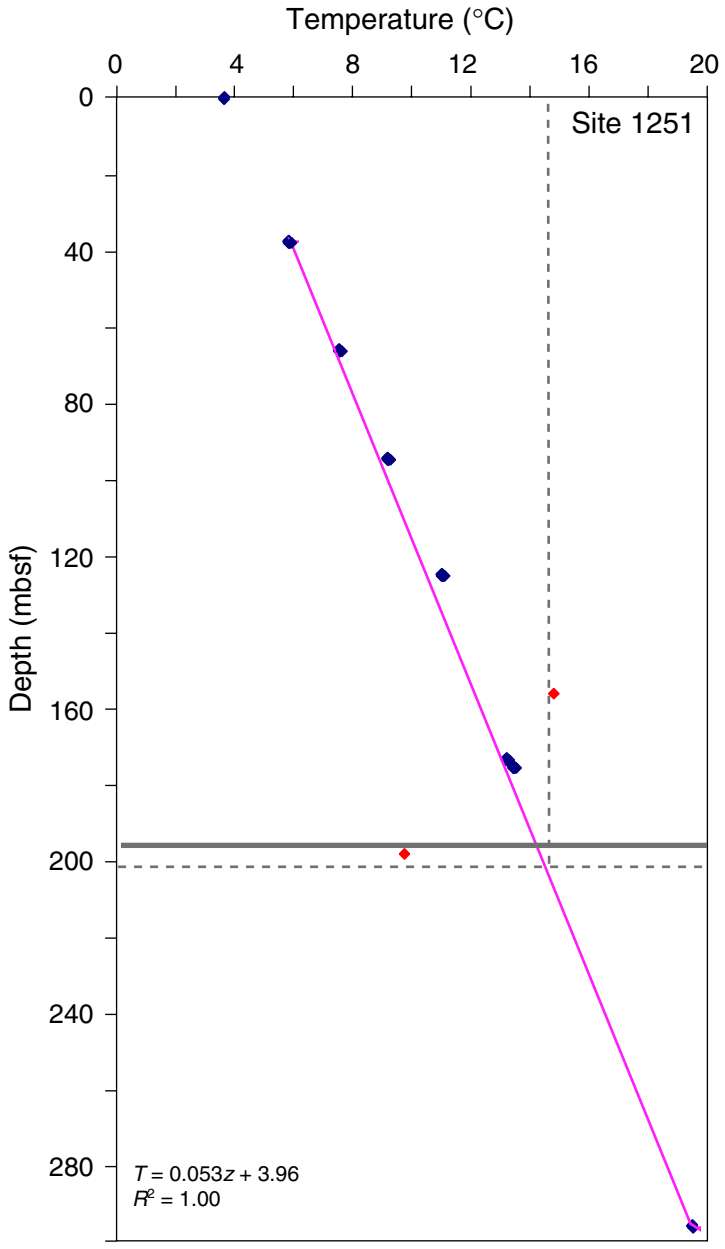

Figure F36. Volume-pressure-time plots for PCS deployed at Site 1251. Note that in Cores 204-1251B-12P and 204-1251D-6P the pressure increased to values equal to or above the pressure obtained in the previous gas release at ~420 and ~650 min of the run, suggesting the decomposition of gas hydrate. (Continued on next page.)

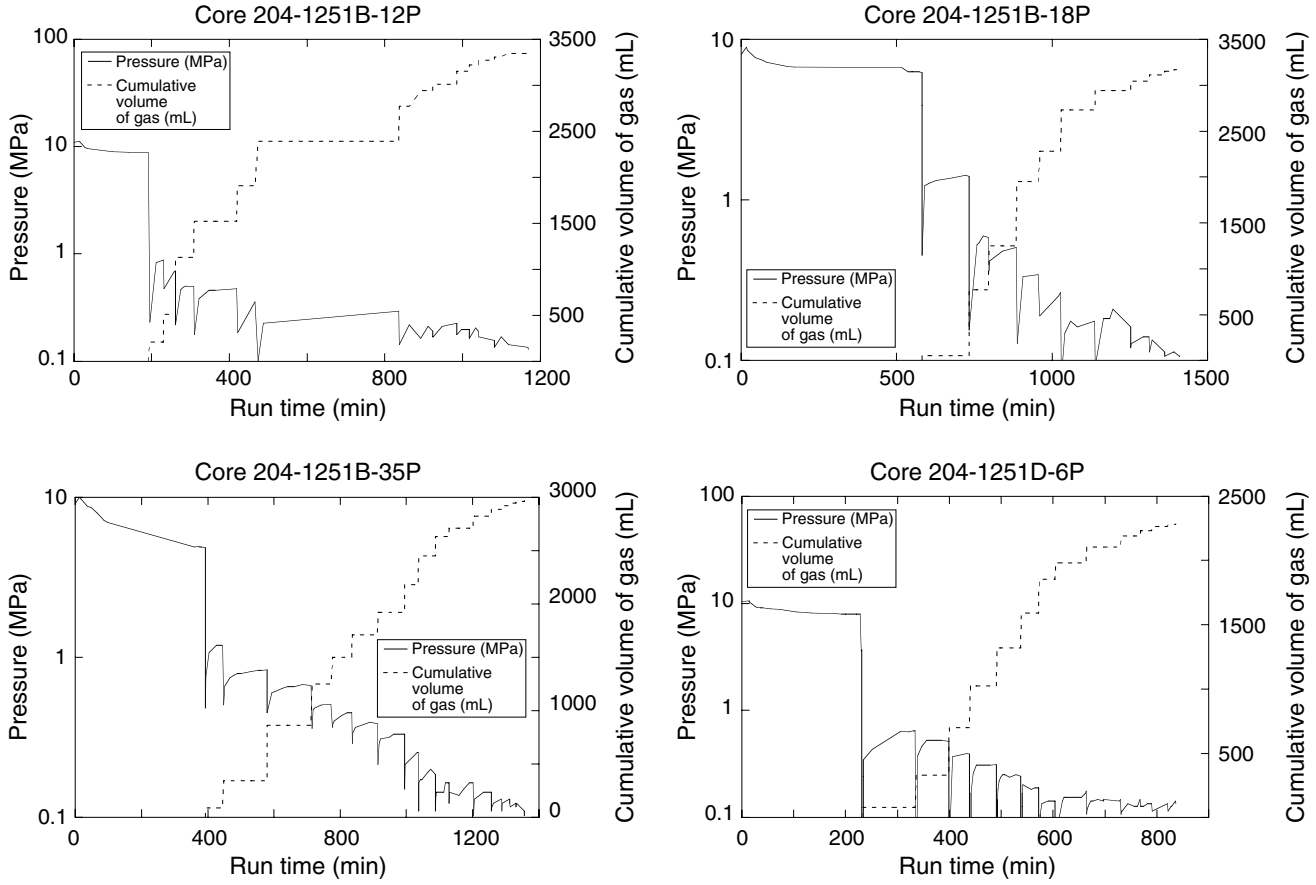

Figure F36 (continued).

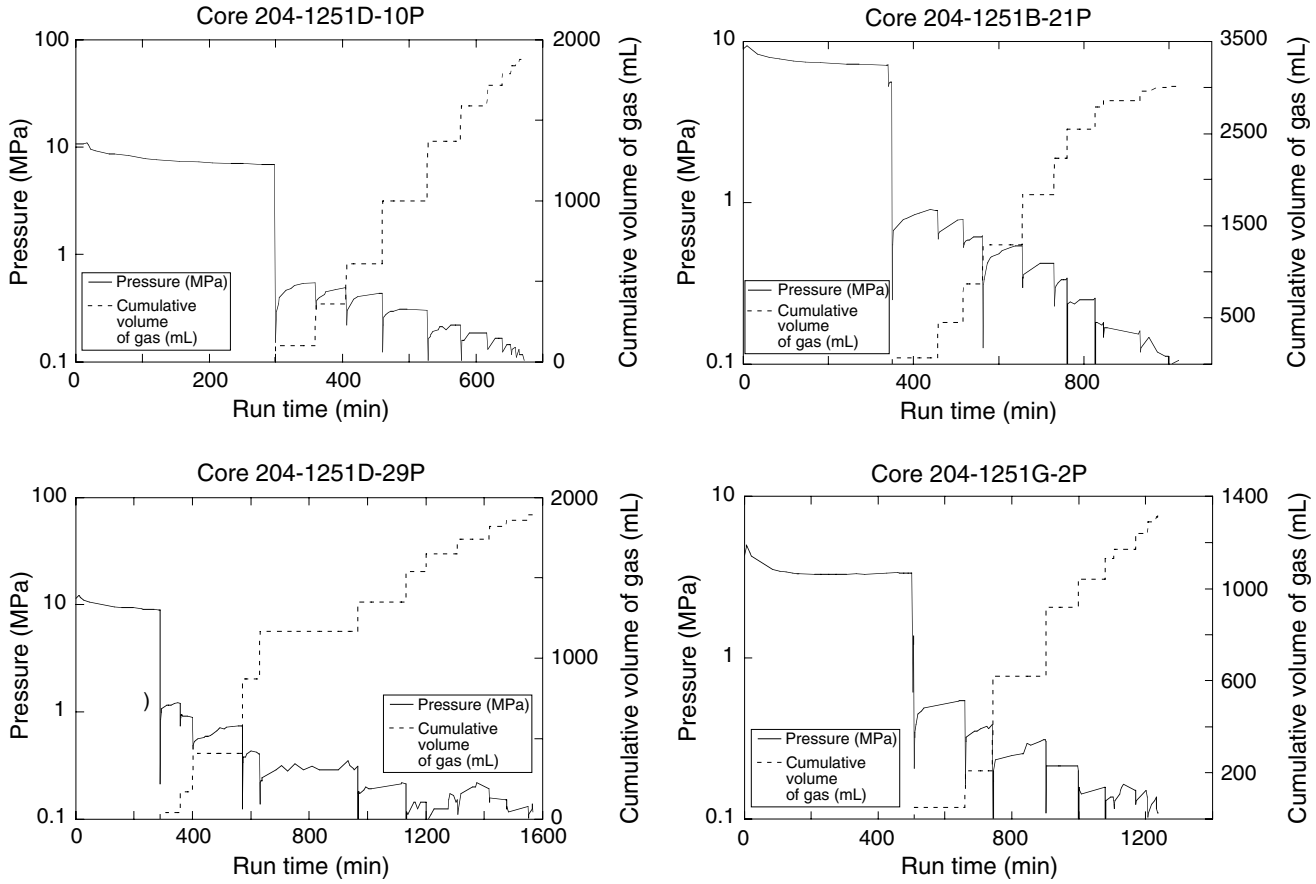

Figure F37. Methane (CH_4) concentration in sediments at Site 1251 based on headspace (HS) and PCS data. Estimated theoretical solubility of methane in pore water (extrapolated from values calculated for higher pressures (depths) (Handa, 1990; Duan et al., 1992) is shown and fields of dissolved methane (D), methane hydrate (H), and free methane (F) are depicted. The gray area indicates the uncertainties in the position of the boundaries. Note that the headspace technique fails to determine accurate concentration values above ~2 mM because methane is relatively abundant in situ and it rapidly escapes from sediments upon core retrieval. PCS = pressure core sampler.

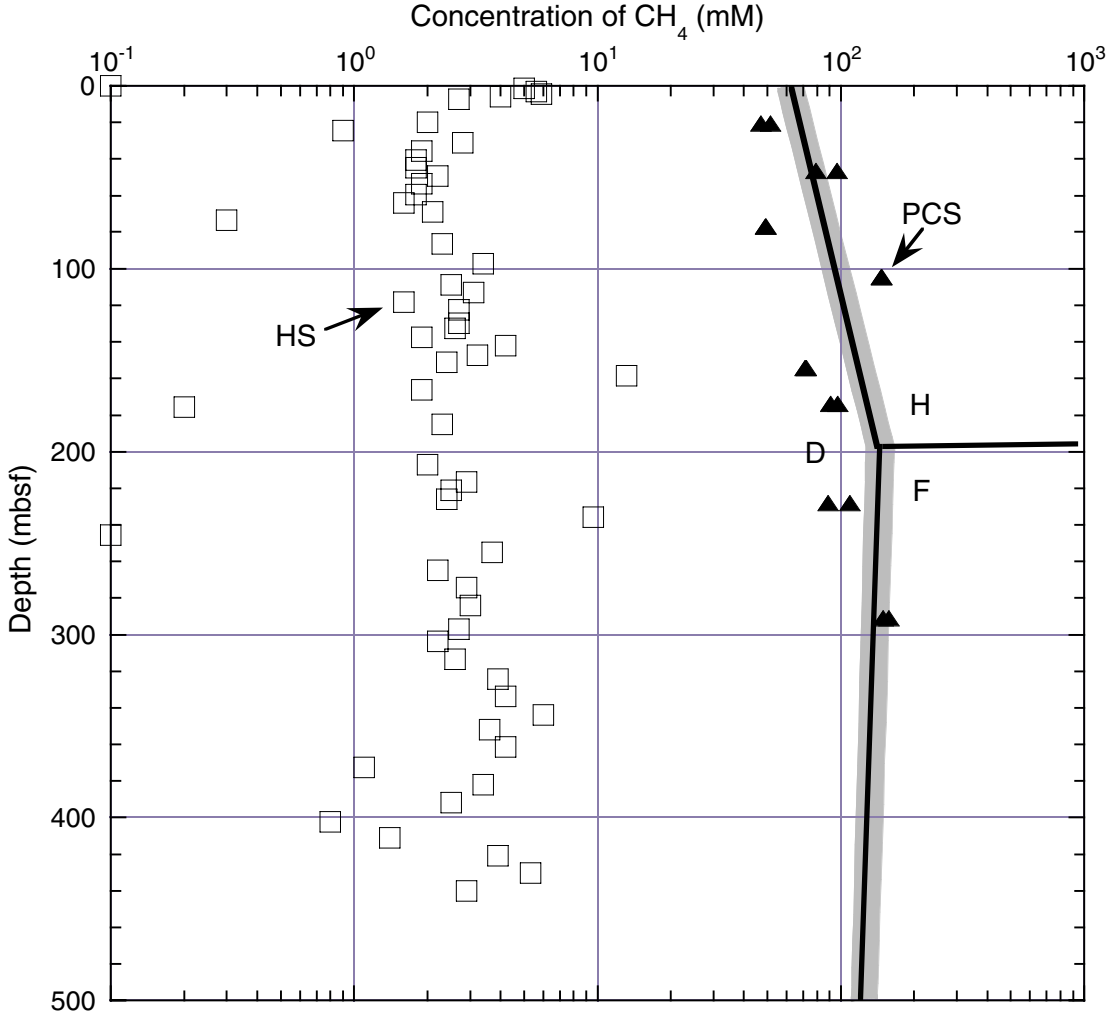

Figure F38. Quality control LWD logs from Hole 1251A. ROP = rate of penetration, TAB = time after bit, Diff. = differential.

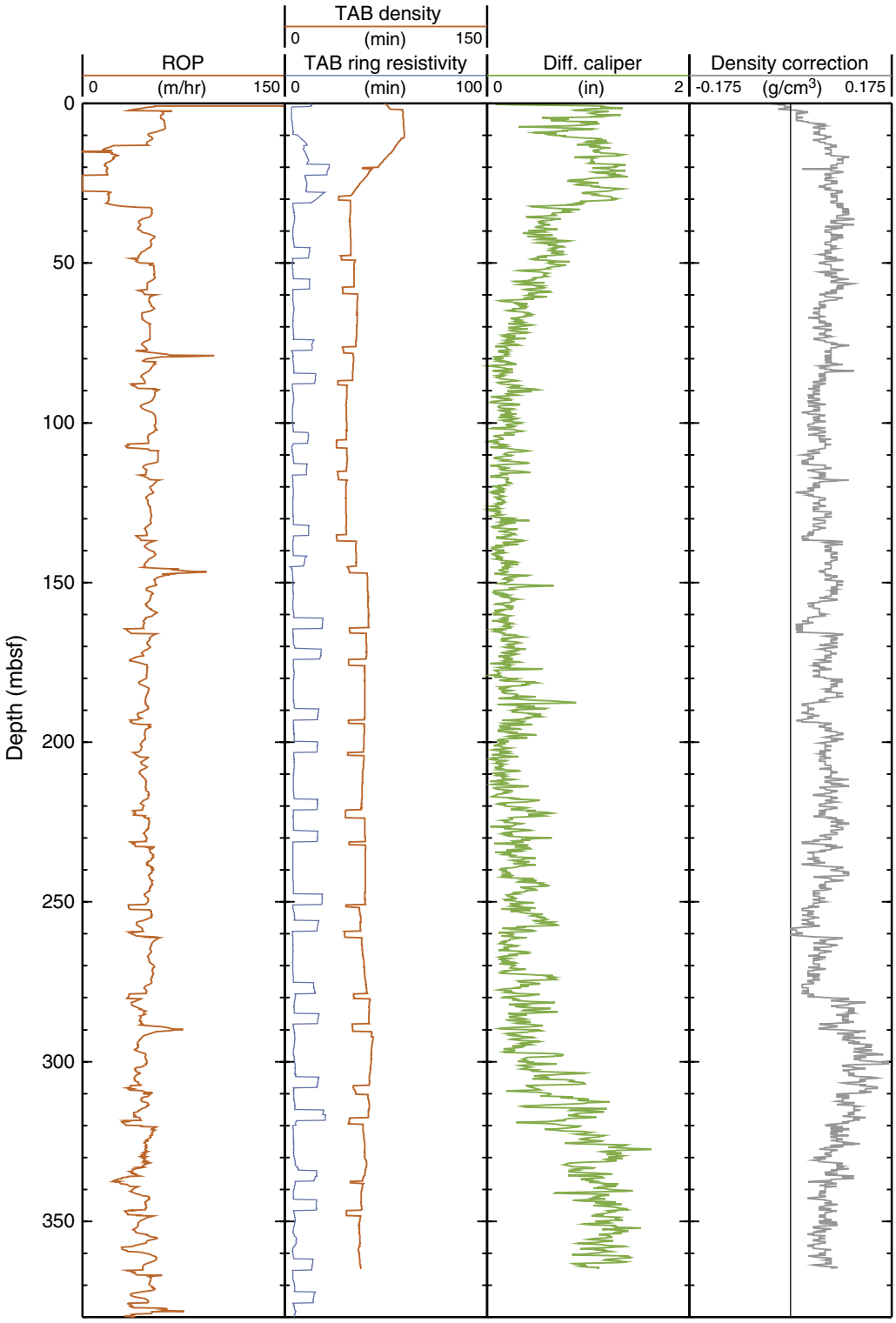

Figure F39. Summary of LWD data from Hole 1251A. gAPI = American Petroleum Institute gamma ray units, PEF = photoelectric effect factor, RAB = resistivity at the bit.

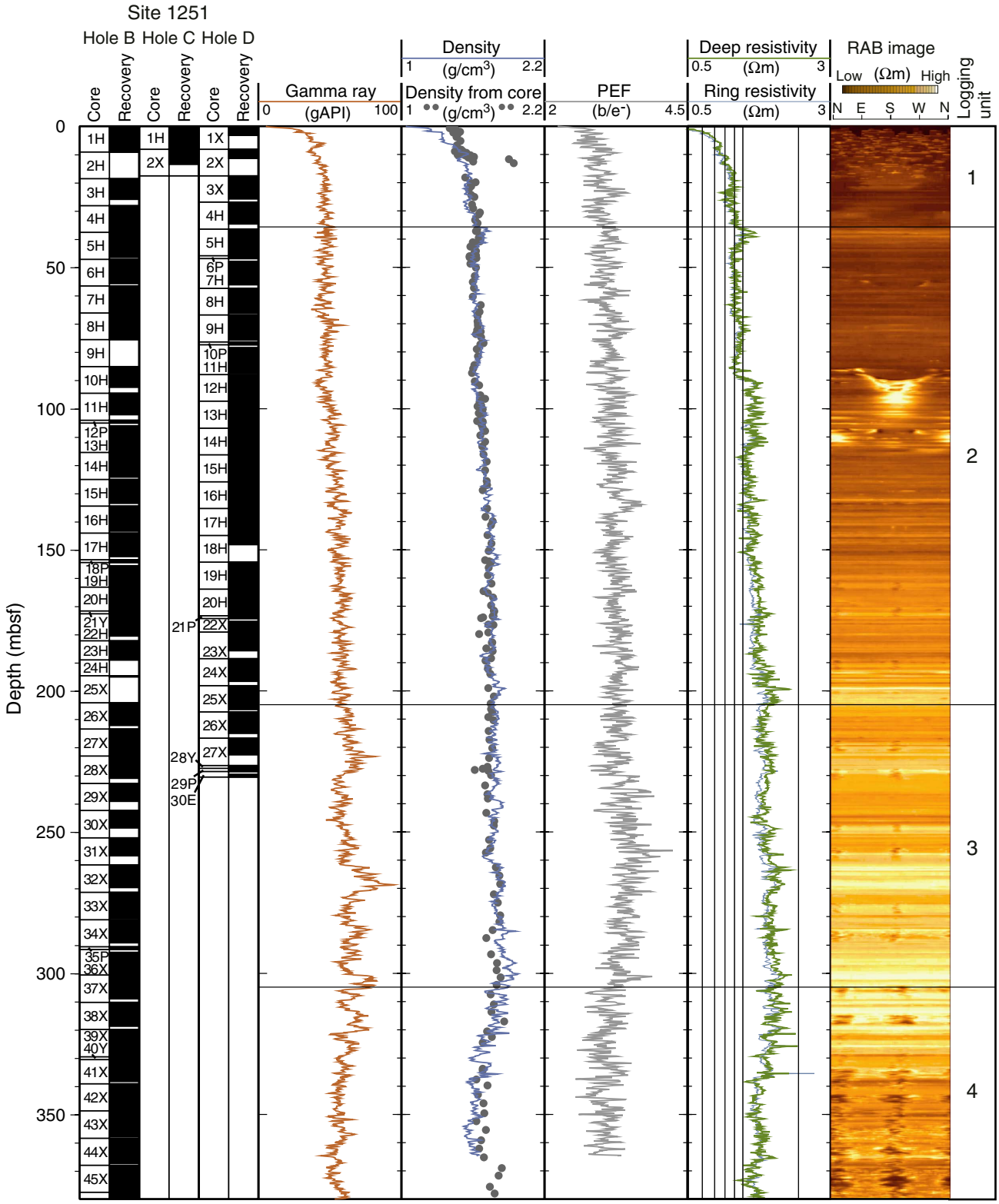

Figure F40. Summary of CWL data from Hole 1251H. gAPI = American Petroleum Institute gamma ray units, PEF = photoelectric effect factor.

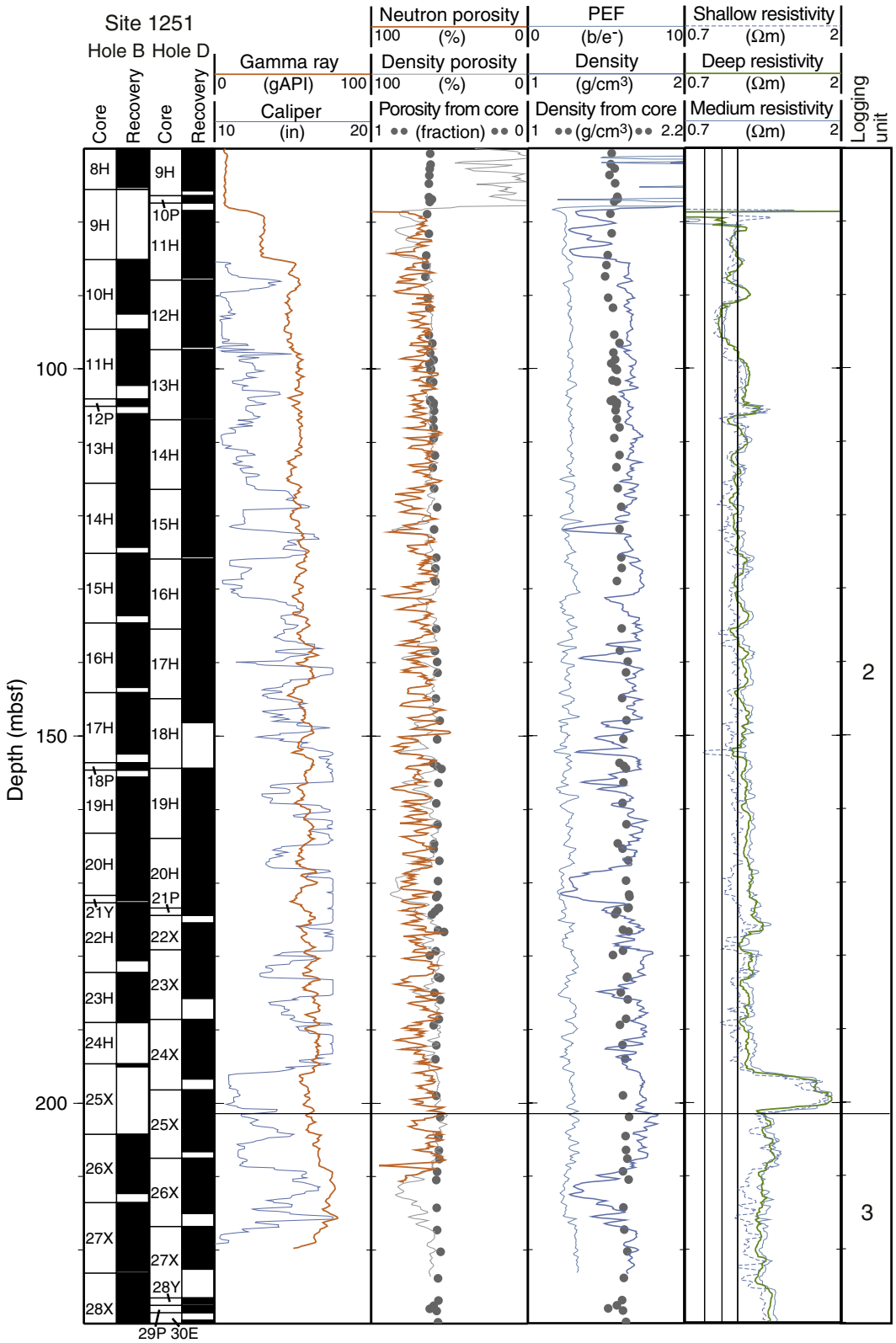

Figure F41. CWL gamma ray logging data from Hole 1251H. FMS = Formation MicroScanner, gAPI = American Petroleum Institute gamma ray units.

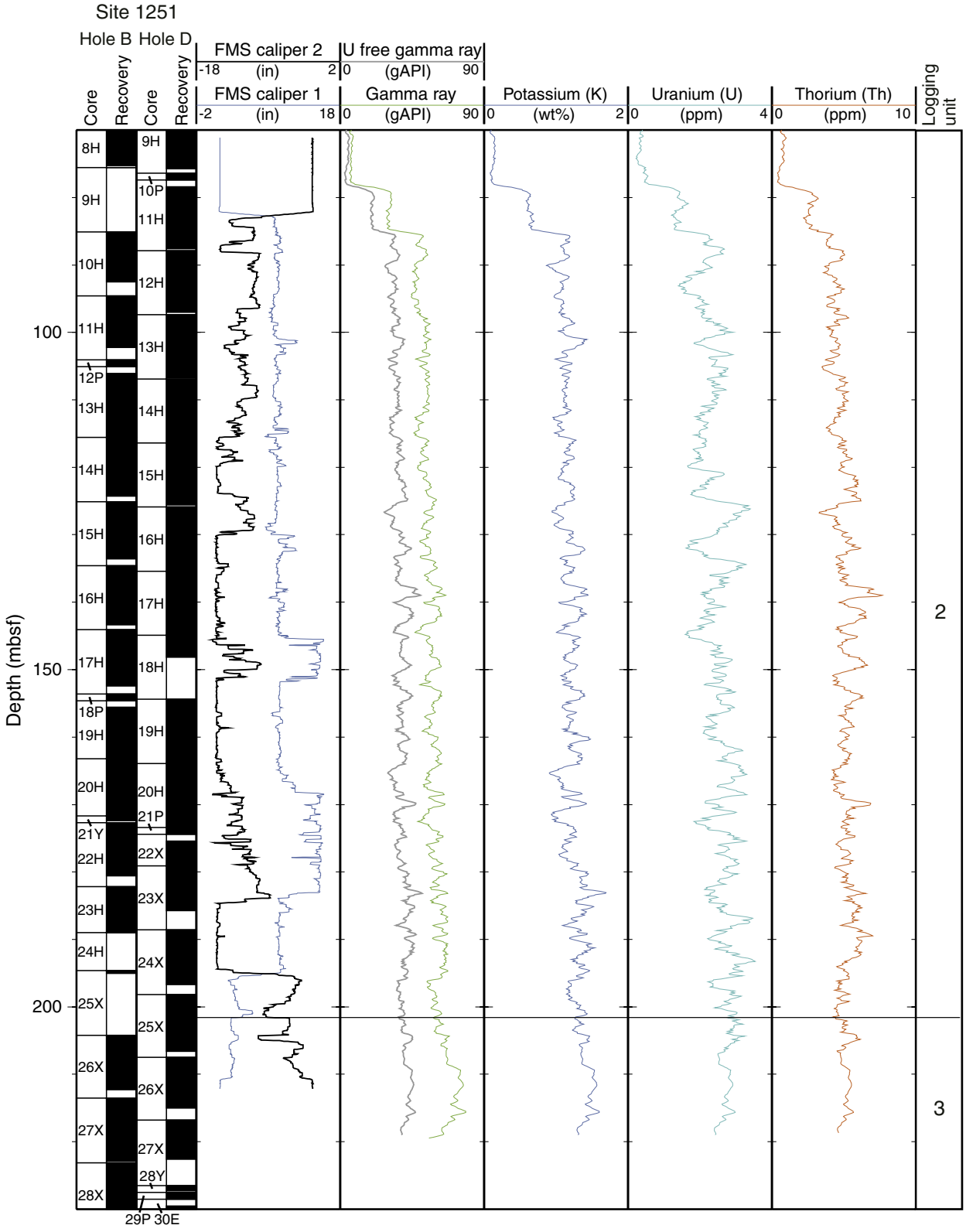

Figure F42. Comparison of LWD and CWL downhole log data from Holes 1251A and 1251H. The logging Unit 2/3 boundary differs in the CWL and LWD data sets. gAPI = American Petroleum Institute gamma ray units, LWD = logging while drilling, por. = porosity, PEF = photoelectric effect factor.

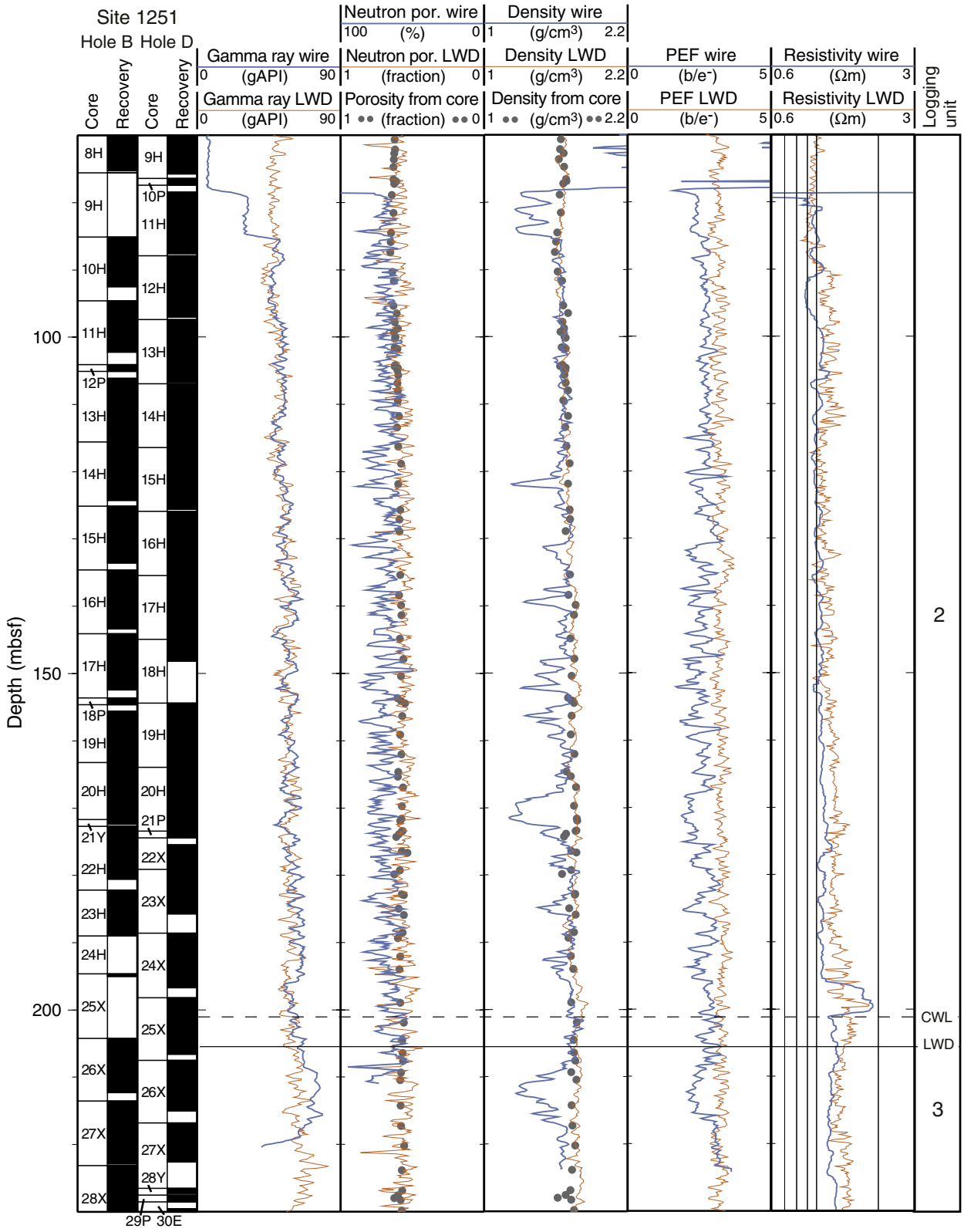

Figure F43. CWL acoustic logging data from Hole 1251H. The resistivity log is used as a reference indicator of the presence of gas hydrate. Low sonic waveform amplitudes are also possible indicators of gas hydrate. Sph. foc. res. = spherically focused resistivity.

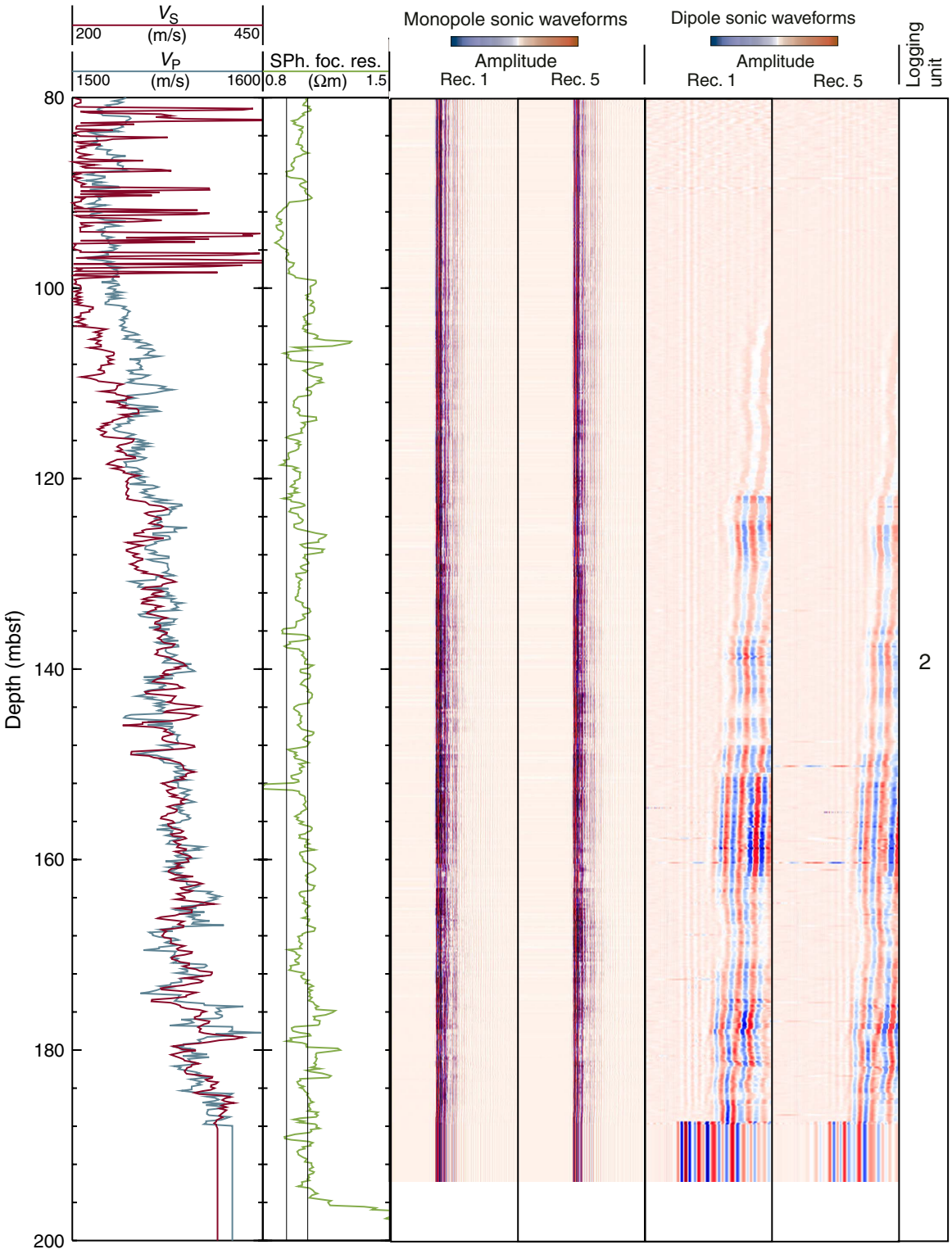

Figure F44. Resistivity-at-the-bit (RAB) image showing borehole breakouts present as irregular, dark, conductive features oriented approximately north-south with depth.

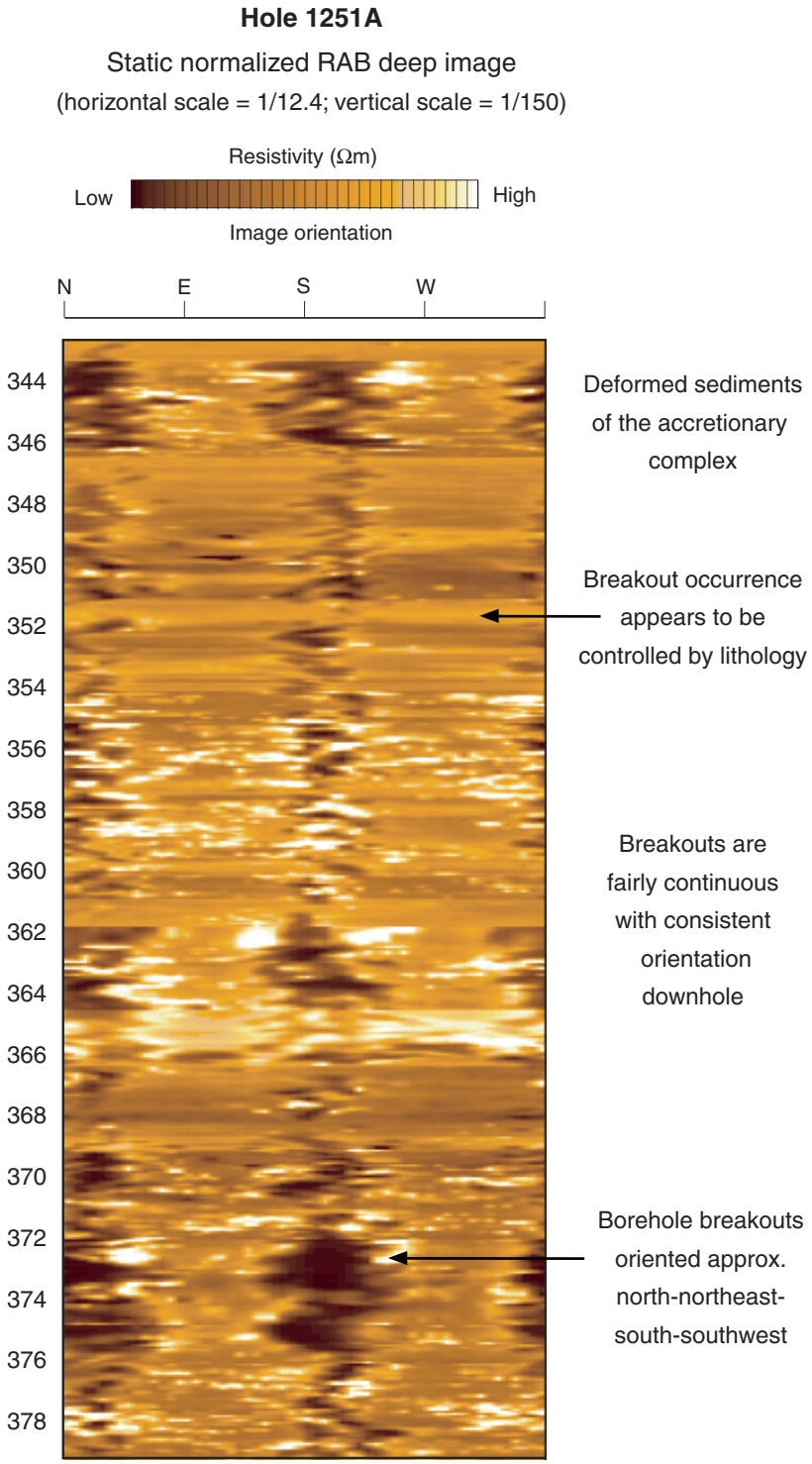

Figure F45. Comparison of LWD- and core-derived porosities from Hole 1251A. NMR-MRP = Nuclear Magnetic Resonance tool, RAB = resistivity-at-the-bit.

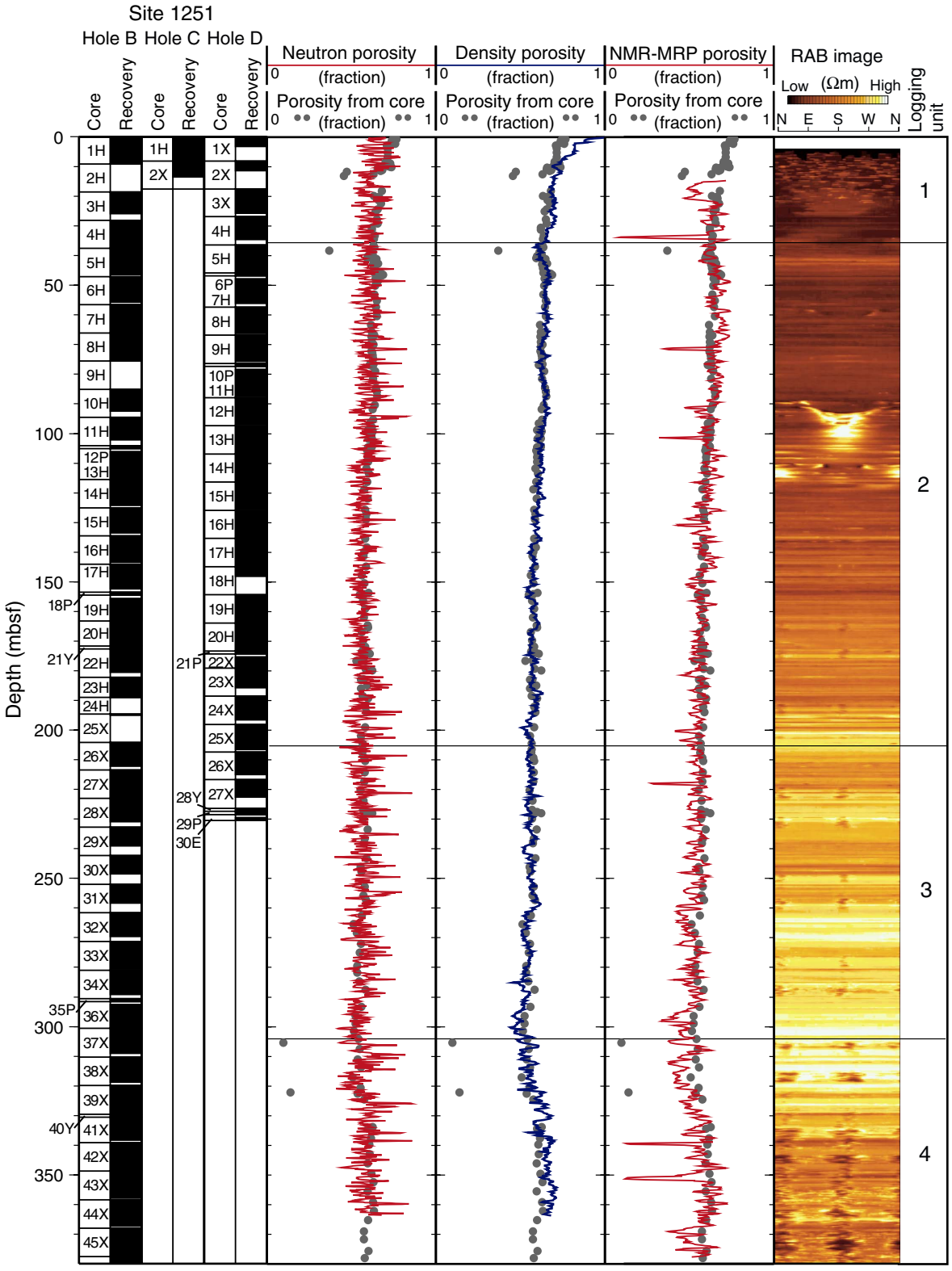

Figure F46. LWD-derived water saturations from Hole 1251A. RAB = resistivity-at-the-bit.

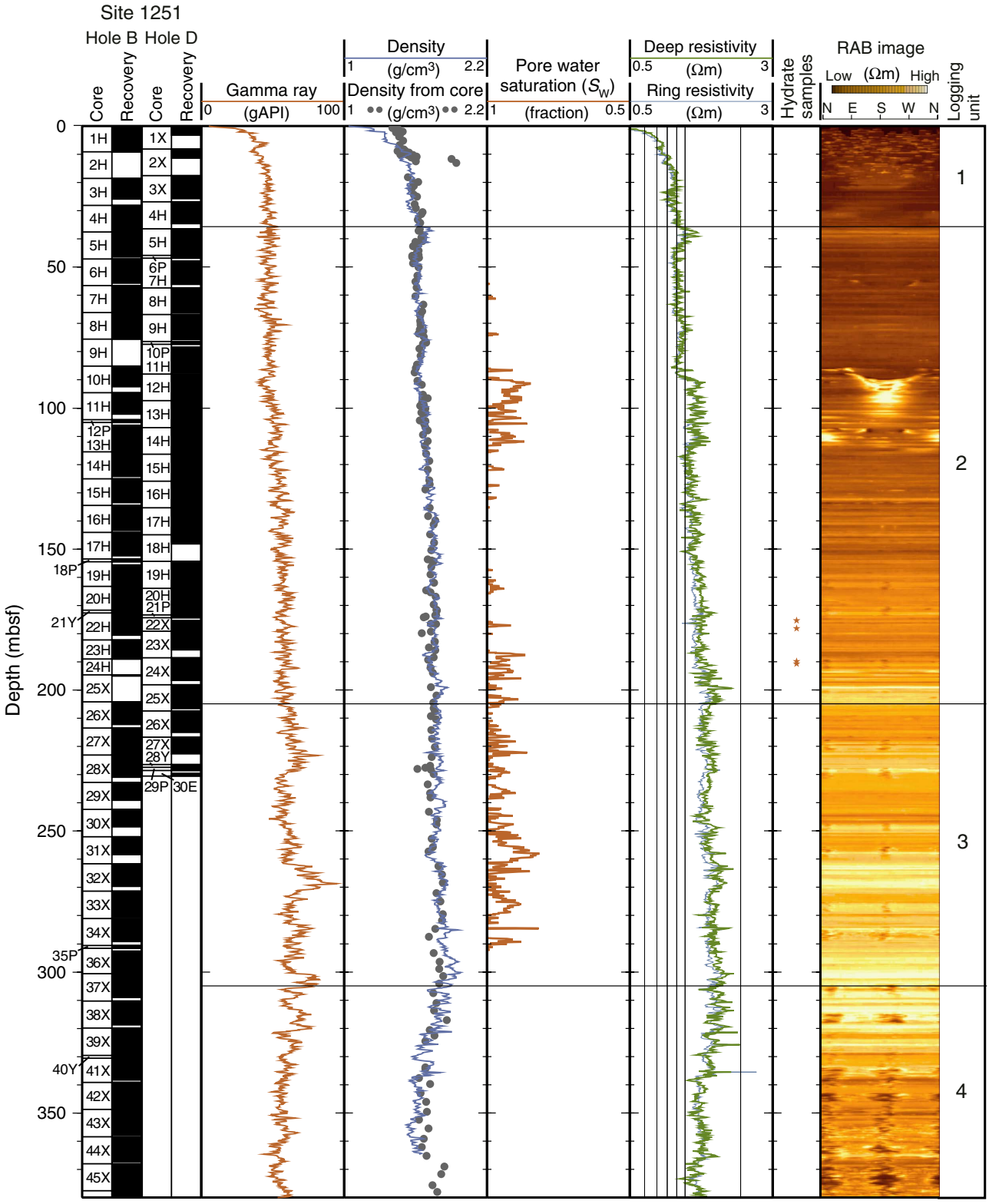

Figure F47. Borehole temperatures recorded with the TAP tool during the down and up pass of the two runs of the triple combo tool string in Hole 1251H.

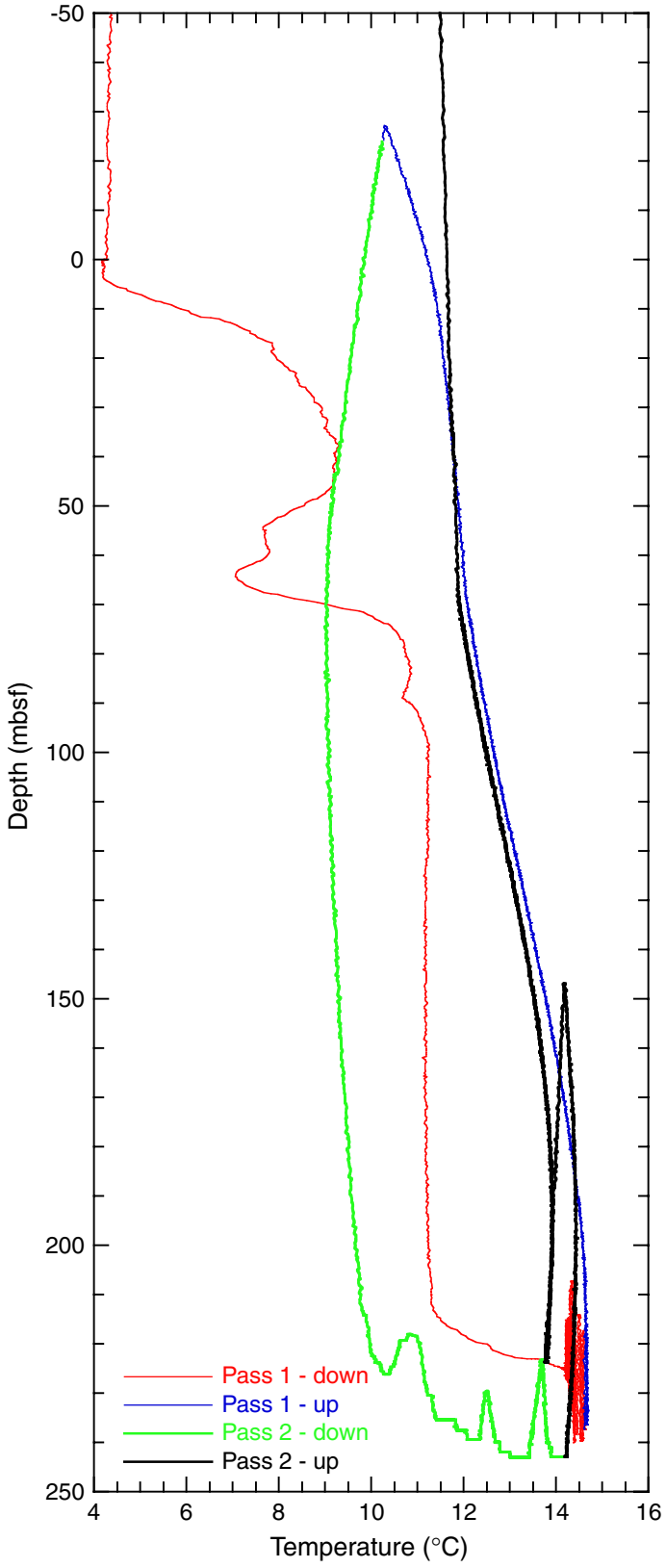

Table T1. Coring summary, Site 1251. (Continued on next three pages.)

Hole 1251A
Latitude: 44°°34.2197′
Longitude: 125°4.4521′
Time on site (hr): 224.25 (1245 hr, 22 Jul–1400 hr, 23 Jul 2002)
Time on hole (hr): 25.25 (1245 hr, 22 Jul–1400 hr, 23 Jul 2002)
Seafloor (drill pipe measurement from rig floor, mbrf): 1228
Distance between rig floor and sea level (m): 11
Water depth (drill pipe measurement from sea level, m): 1217
Total depth (drill pipe measurement from rig floor, mbrf): 1608
Total penetration (meters below seafloor, mbsf): 380
Total number of cores: 0
Total number of drilled intervals: 1
Total length of cored section (m): 0
Total core recovered (m): 0
Core recovery (%): 0

Hole 1251B
Latitude: 44°34.2191′
Longitude: 125°4.4375′
Time on hole (hr): 86.25 (1145 hr, 26 Jul–0200 hr, 30 Jul 2002)
Seafloor (drill pipe measurement from rig floor, mbrf): 1224.4
Distance between rig floor and sea level (m): 11.1
Water depth (drill pipe measurement from sea level, m): 1213.3
Total depth (drill pipe measurement from rig floor, mbrf): 1669.5
Total penetration (meters below seafloor, mbsf): 445.1
Total number of cores: 53
Total number of drilled intervals: 3
Total length of cored section (m): 442.1
Total core recovered (m): 368.56
Core recovery (%): 83.4

Hole 1251C
Latitude: 44°34.2058′
Longitude: 125°4.4366′
Time on hole (hr): 4.5 (0200 hr, 30 Jul–0630 hr, 30 Jul 2002)
Seafloor (drill pipe measurement from rig floor, mbrf): 1221.4
Distance between rig floor and sea level (m): 11.2
Water depth (drill pipe measurement from sea level, m): 1210.2
Total depth (drill pipe measurement from rig floor, mbrf): 123
Total penetration (meters below seafloor, mbsf): 17.6
Total number of cores: 2
Total number of drilled intervals: 0
Total length of cored section (m): 17.6
Total core recovered (m): 13.63
Core recovery (%): 77.4

Hole 1251D
Latitude: 44°34.206′
Longitude: 125°4.4365′
Time on hole (hr): 38.25 (0630 hr, 30 Jul–2045 hr, 31 Jul 2002)
Seafloor (drill pipe measurement from rig floor, mbrf): 1221.4
Distance between rig floor and sea level (m): 11.2
Water depth (drill pipe measurement from sea level, m): 1210.2
Total depth (drill pipe measurement from rig floor, mbrf): 1451.9
Total penetration (meters below seafloor, mbsf): 230.5
Total number of cores: 30
Total number of drilled intervals: 4
Total length of cored section (m): 226.5
Total core recovered (m): 194.4
Core recovery (%): 85.8

Table T1 (continued).

Hole 1251E
Latitude: 44°34.2126′
Longitude: 125°4.4358′
Time on hole (hr): 1.75 (2045 hr, 31 Jul–2230 hr, 31 Jul 2002)
Seafloor (drill pipe measurement from rig floor, mbrf): 1220
Distance between rig floor and sea level (m): 11.2
Water depth (drill pipe measurement from sea level, m): 1208.8
Total depth (drill pipe measurement from rig floor, mbrf): 1229.5
Total penetration (meters below seafloor, mbsf): 9.5
Total number of cores: 1
Total number of drilled intervals: 0
Total length of cored section (m): 9.5
Total core recovered (m): 9.89
Core recovery (%): 104.1

Hole 1251F
Latitude: 44°34.2159′
Longitude: 125°4.4369′
Time on hole (hr): 0.25 (2230 hr, 31 Jul–2245 hr, 31 Jul 2002)
Seafloor (drill pipe measurement from rig floor, mbrf): 1220
Distance between rig floor and sea level (m): 11.2
Water depth (drill pipe measurement from sea level, m): 1208.8
Total depth (drill pipe measurement from rig floor, mbrf): 1229.5
Total penetration (meters below seafloor, mbsf): 9.5
Total number of cores: 1
Total number of drilled intervals: 0
Total length of cored section (m): 9.5
Total core recovered (m): 9.92
Core recovery (%): 104.4

Hole 1251G
Latitude: 44°34.2145′
Longitude: 125°4.4364′
Time on hole (hr): 4.25 (2245 hr, 31 Jul–0300 hr, 1 Aug 2002)
Seafloor (drill pipe measurement from rig floor, mbrf): 1220
Distance between rig floor and sea level (m): 11.2
Water depth (drill pipe measurement from sea level, m): 1208.8
Total depth (drill pipe measurement from rig floor, mbrf): 1241
Total penetration (meters below seafloor, mbsf): 21
Total number of cores: 2
Total number of drilled intervals: 2
Total length of cored section (m): 10.5
Total core recovered (m): 11.11
Core recovery (%): 105.8

Hole 1251H
Latitude: 44°34.2089′
Longitude: 125°4.4514′
Time on hole (hr): 63.75 (0715 hr, 16 Aug–2300 hr, 18 Aug 2002)
Seafloor (drill pipe measurement from rig floor, mbrf): 1220
Distance between rig floor and sea level (m): 11.5
Water depth (drill pipe measurement from sea level, m): 1208.5
Total depth (drill pipe measurement from rig floor, mbrf): 1665
Total penetration (meters below seafloor, mbsf): 445
Total number of cores: 0
Total number of drilled intervals: 1
Total length of cored section (m): 0
Total core recovered (m): 0
Core recovery (%): 0

Core	Date (2002)	Local time (hr)	Depth (mbsf) Top	Depth (mbsf) Bottom	Length (m) Cored	Length (m) Recovered	Recovery (%)
204-1251A-							
			*****Drilled from 0 to 380 mbsf*****				
204-1251B-							
1H	26 Jul	1820	0.0	9.1	9.1	9.10	100.0
2H	26 Jul	1905	9.1	18.6	9.5	0.00	0.0
3H	26 Jul	1940	18.6	28.1	9.5	7.31	76.9
4H	26 Jul	2040	28.1	37.6	9.5	9.62	101.3
5H	26 Jul	2125	37.6	47.1	9.5	8.87	93.4
6H	26 Jul	2155	47.1	56.6	9.5	8.70	91.6

Table T1 (continued).

Core	Date (2002)	Local time (hr)	Depth (mbsf) Top	Depth (mbsf) Bottom	Length (m) Cored	Length (m) Recovered	Recovery (%)
7H	26 Jul	2305	56.6	66.1	9.5	9.75	102.6
8H	26 Jul	2335	66.1	75.6	9.5	9.20	96.8
9H	27 Jul	0010	75.6	85.1	9.5	0.00	0.0
10H	27 Jul	0105	85.1	94.6	9.5	7.41	78.0
11H	27 Jul	0800	94.6	104.1	9.5	7.64	80.4
12P	27 Jul	0955	104.1	105.1	1.0	1.00	100.0
			*****Drilled from 105.1 to 106.1 mbsf*****				
13H	27 Jul	1045	106.1	115.6	9.5	9.64	101.5
14H	27 Jul	1135	115.6	125.1	9.5	8.66	91.2
15H	27 Jul	1215	125.1	134.6	9.5	8.47	89.2
16H	27 Jul	1310	134.6	144.1	9.5	8.77	92.3
17H	27 Jul	1350	144.1	153.6	9.5	8.32	87.6
18P	27 Jul	1510	153.6	154.6	1.0	1.00	100.0
			*****Drilled from 154.6 to 155.6 mbsf*****				
19H	27 Jul	1800	155.6	163.2	7.6	8.09	106.4
20H	27 Jul	1845	163.2	171.7	8.5	8.63	101.5
21Y	27 Jul	2000	171.7	172.7	1.0	0.90	90.0
22H	27 Jul	2055	172.7	182.2	9.5	7.89	83.1
23H	27 Jul	2140	182.2	189.0	6.8	6.79	99.9
24H	27 Jul	2240	189.0	194.6	5.6	0.00	0.0
25X	27 Jul	2350	194.6	204.2	9.6	0.44	4.6
26X	28 Jul	0110	204.2	213.5	9.3	8.09	87.0
27X	28 Jul	0215	213.5	223.1	9.6	9.37	97.6
28X	28 Jul	0335	223.1	232.8	9.7	7.90	81.4
29X	28 Jul	0445	232.8	242.4	9.6	6.38	66.5
30X	28 Jul	0559	242.4	252.1	9.7	6.14	63.3
31X	28 Jul	0750	252.1	261.7	9.6	6.25	65.1
32X	28 Jul	0915	261.7	271.3	9.6	7.89	82.2
33X	28 Jul	1045	271.3	281.0	9.7	9.29	95.8
34X	28 Jul	1210	281.0	290.6	9.6	8.17	85.1
35P	28 Jul	1310	290.6	291.6	1.0	1.00	100.0
			*****Drilled from 291.6 to 292.6 mbsf*****				
36X	28 Jul	1610	292.6	300.6	8.0	8.05	100.6
37X	28 Jul	1740	300.6	310.3	9.7	8.41	86.7
38X	28 Jul	1900	310.3	319.9	9.6	8.44	87.9
39X	28 Jul	2040	319.9	329.6	9.7	9.69	99.9
40Y	28 Jul	2210	329.6	330.6	1.0	0.90	90.0
41X	28 Jul	2355	330.6	339.2	8.6	7.69	89.4
42X	29 Jul	0115	339.2	348.8	9.6	9.23	96.1
43X	29 Jul	0250	348.8	358.4	9.6	9.05	94.3
44X	29 Jul	0405	358.4	368.0	9.6	8.96	93.3
45X	29 Jul	0530	368.0	377.6	9.6	9.65	100.5
46X	29 Jul	0740	377.6	387.3	9.7	9.43	97.2
47X	29 Jul	0935	387.3	396.9	9.6	9.40	97.9
48E	29 Jul	1155	396.9	397.9	1.0	0.00	0.0
49X	29 Jul	1345	397.9	406.5	8.6	8.06	93.7
50X	29 Jul	1530	406.5	416.2	9.7	8.77	90.4
51X	29 Jul	1725	416.2	425.8	9.6	10.01	104.3
52X	29 Jul	1940	425.8	435.5	9.7	8.99	92.7
53X	29 Jul	2235	435.5	445.1	9.6	7.15	74.5
				Cored totals:	442.1	368.56	83.4
				Drilled total:	3.0		
				Total:	445.1		
204-1251C-							
1H	30 Jul	0325	0.0	8.1	8.1	8.18	101.0
2X	30 Jul	0555	8.1	17.6	9.5	5.45	57.4
				Cored totals:	17.6	13.63	77.4
				Drilled total:	0.0		
				Total:	17.6		
204-1251D-							
1X	30 Jul	0725	0.0	8.1	8.1	3.23	39.9
2X	30 Jul	0755	8.1	17.6	9.5	3.35	35.3
3X	30 Jul	0835	17.6	26.9	9.3	8.12	87.3
4H	30 Jul	0905	26.9	36.4	9.5	7.77	81.8
5H	30 Jul	0945	36.4	45.9	9.5	9.67	101.8
6P	30 Jul	1055	45.9	46.9	1.0	1.00	100.0
			*****Drilled from 46.9 to 47.9 mbsf*****				

Table T1 (continued).

Core	Date (2002)	Local time (hr)	Depth (mbsf) Top	Depth (mbsf) Bottom	Length (m) Cored	Length (m) Recovered	Recovery (%)
7H	30 Jul	1135	47.9	57.4	9.5	8.27	87.1
8H	30 Jul	1205	57.4	66.9	9.5	8.90	93.7
9H	30 Jul	1240	66.9	76.4	9.5	8.86	93.3
10P	30 Jul	1405	76.4	77.4	1.0	1.00	100.0
			*****Drilled from 77.4 to 78.4 mbsf*****				
11H	30 Jul	1450	78.4	87.9	9.5	9.18	96.6
12H	30 Jul	1520	87.9	97.4	9.5	9.13	96.1
13H	30 Jul	1555	97.4	106.9	9.5	9.36	98.5
14H	30 Jul	1640	106.9	116.4	9.5	9.68	101.9
15H	30 Jul	1705	116.4	125.9	9.5	9.21	96.9
16H	30 Jul	1800	125.9	135.4	9.5	10.04	105.7
17H	30 Jul	1840	135.4	144.9	9.5	9.90	104.2
18H	30 Jul	1925	144.9	154.4	9.5	3.26	34.3
19H	30 Jul	2145	154.4	163.9	9.5	9.59	100.9
20H	31 Jul	0125	163.9	173.4	9.5	9.67	101.8
21P	31 Jul	0335	173.4	174.4	1.0	1.00	100.0
			*****Drilled from 174.4 to 175.4 mbsf*****				
22X	31 Jul	0610	175.4	179.1	3.7	5.69	153.8
23X	31 Jul	0715	179.1	188.6	9.5	6.66	70.1
24X	31 Jul	0825	188.6	198.2	9.6	8.08	84.2
25X	31 Jul	0930	198.2	207.5	9.3	8.37	90.0
26X	31 Jul	1215	207.5	216.8	9.3	7.50	80.6
27X	31 Jul	1310	216.8	226.5	9.7	5.82	60.0
28Y	31 Jul	1500	226.5	227.5	1.0	0.87	87.0
29P	31 Jul	1640	227.5	228.5	1.0	1.00	100.0
			*****Drilled from 228.5 to 229.5 mbsf*****				
30E	31 Jul	1830	229.5	230.5	1.0	0.22	22.0
			Cored totals:		226.5	194.40	85.8
			Drilled total:		4.0		
			Total:		230.5		
204-1251E-							
1H	31 Jul	2225	0.0	9.5	9.5	9.89	104.1
			Cored totals:		9.5	9.89	104.1
			Drilled total:		0.0		
			Total:		9.5		
204-1251F-							
1H	31 Jul	2250	0.0	9.5	9.5	9.92	104.4
			Cored totals:		9.5	9.92	104.4
			Drilled total:		0.0		
			Total:		9.5		
204-1251G-							
			*****Drilled from 0 to 2.5 mbsf*****				
1H	31 Jul	2320	2.5	12.0	9.5	10.11	106.4
			*****Drilled from 12 to 20 mbsf*****				
2P	1 Aug	0100	20	21.0	1.0	1.00	100.0
			Cored totals:		10.5	11.11	105.8
			Drilled total:		10.5		
			Total:		21.0		
204-1251H-							
			*****Drilled from 0 to 445 mbsf*****				12.6

Table T2. Mineralogic composition of carbonate samples in lithostratigraphic Unit III, Hole 1251B.

Core, section	Depth (mbsf)	Carbonate minerals	Comment
204-1251B-			
37X-4	305.40	Dolomite	Solid
37X-4	305.40	Dolomite	Solid
39X-2	322.08	Dolomite, calcite	Solid
41X-4	336.12	NA	Solid
46X-1	378.56	Calcite	Semiconsolidated
46X-CC	386.77	Calcite	Semiconsolidated
47X-5	394.51	Calcite; two different phases	Semiconsolidated
49X-1	398.76	Calcite, dolomite; three different phases	Semiconsolidated
52X-1	427.12	Calcite	Solid

Note: NA = not applicable.

Table T3. Bioevents, Hole 1251B.

Age (Ma)	Bioevent	Top		Bottom		Average depth (mbsf)	Event number*	Comment
		Core, section, interval (cm)	Depth (mbsf)	Core, section, interval (cm)	Depth (mbsf)			
		204-1251B-		204-1251B-				
0.09	FO *Emiliania huxleyi* acme	1H-CC	9.05	3H-CC	25.85	17.45	1	Nannofossil
0.27	FO *Emiliania huxleyi*	19H-1, 74–75	156.34	19H-CC	163.64	159.99	2	Nannofossil
0.30	LO *Proboscia curvirostris*	19H-CC	163.64	20H-CC	171.76	167.70	3	Diatom
0.46	LO *Pseudoemiliania lacunosa*	23H-CC	188.89	25X-CC	204.10	196.50	4	Nannofossil
1.0	LO *Actinocyclus oculatus*	34X-CC	289.12	39X-6, 57–59	327.99	308.56	5	Diatom
1.0–1.2	FO small *Gephyrocapsa* spp. acme	33X-CC	280.54	34X-CC	289.12	284.83	6	Nannofossil
1.59	FO *Calcydiscus macintyrei*	33X-CC	280.54	34X-CC	289.12	284.83	7	Nannofossil
1.67	FO *Gephyrocapsa lumina*	38X-4, 68	315.48	38X-CC	318.69	317.09	8	Nannofossil
1.6	FO *Proboscia curvirostris*	42X-CC	348.38	43X-CC	357.80	353.09	9	Diatom
1.7	FO medium *Gephyrocapsa* spp.	45X-3, 66–68	371.66	46X-CC	386.98	379.32	10	Nannofossil
2.0	LO *Neodenticula koizumii*	52X-CC	434.69	53X-2, 64–66	437.62	436.16	11	Diatom

Notes: * = number in Figure F11, p. 51. FO = first occurrence, LO = last occurrence.

Table T4. Interstitial water data, Holes 1251B, 1251C, and 1251D. (See table notes. Continued on next two pages.)

Core, section, interval (cm)	Depth (mbsf)	pH	Alkalinity (mM)	Salinity (g/kg)	Cl (mM)	SO_4 (mM)	NH_4 (mM)	PO_4 (µM)	Na (mM)	K (mM)	Mg (mM)	Ca (mM)	B (µM)	Ba (µM)	Fe (µM)	Li (µM)	Mn (µM)	Sr (µM)	DOC (mM)
204-1251B-																			
1H-2, 145–150	2.95	7.84	56.64	35	553	0.7	4.1	228	480	12.2	49.9	3.8	789	10.2	3.4	13.07	0.57	77.33	—
1H-5, 145–150	7.45	7.50	74.96	35	547	0.0	6.2	344	526	12.5	54.0	2.7	935	35.4	3.8	11.43	0.51	71.00	—
3H-2, 140–150	21.43	7.50	107.29	39	544	0.0	9.1	295	501	13.8	62.6	1.9	1050	44.6	88.2	14.20	1.18	68.98	—
3H-4, 140–150	24.41	7.54	105.16	38	544	0.4	9.8	320	505	14.4	61.8	1.6	1057	46.8	17.6	15.41	1.21	65.59	—
4H-2, 140–150	31.00	7.42	111.17	38	544	0.3	10.2	358	509	14.0	62.7	1.3	1149	45.4	45.0	17.15	0.78	62.00	36.37
4H-5, 140–150	35.50	7.45	117.86	38	542	0.0	11.4	357	509	14.1	64.3	1.5	1212	46.1	55.8	15.46	1.05	64.88	—
5H-2, 131–141	40.41	7.51	122.37	39	543	0.0	11.4	369	500	14.0	65.3	2.2	1170	45.8	29.6	15.03	1.26	67.28	—
5H-5, 138–150	44.84	7.65	111.28	39	538	0.0	12.1	362	512	15.2	63.1	1.6	—	—	—	—	—	—	—
6H-2, 130–140	49.22	7.46	111.20	38	533	0.1	11.4	393	508	14.2	61.3	1.7	1158	52.1	12.7	15.85	1.05	67.65	—
6H-5, 131–141	53.61	7.69	108.35	37	531	0.0	11.0	391	504	14.3	57.8	1.9	1198	54.8	31.2	16.51	1.35	65.47	—
7H-2, 140–150	59.50	7.75	—	35	532	0.0	11.9	346	501	15.0	50.7	1.3	1180	56.3	20.8	16.96	1.32	63.33	19.04
7H-5, 140–150	64.00	7.64	92.47	35	529	0.0	11.6	399	498	13.5	49.3	1.1	1094	47.6	11.1	17.45	0.55	56.85	—
8H-2, 140–150	69.00	7.36	94.14	35	520	0.0	12.1	418	502	13.5	—	—	1118	43.1	21.4	18.15	0.60	59.67	—
8H-5, 140–150	73.38	7.53	99.13	36	526	0.1	12.5	334	504	14.8	52.1	1.2	1043	41.4	9.5	18.27	0.53	62.02	—
10H-2, 140–150	88.00	7.41	117.70	36	519	0.0	11.7	397	501	13.2	59.1	2.7	997	52.4	43.9	16.61	1.16	71.76	—
10H-4, 140–150	91.00	7.45	119.72	37	514	0.3	12.9	426	494	13.3	58.3	2.6	1005	56.2	62.8	16.16	1.30	72.01	—
11H-2, 74–94	96.84	7.88	112.96	36	514	0.0	12.8	414	493	13.4	56.1	2.5	881	58.9	29.6	17.95	1.00	70.37	—
11H-5, 70–90	100.61	7.72	116.42	36	511	0.0	12.6	420	498	13.9	55.7	3.2	1006	65.0	26.8	20.53	3.01	71.62	—
13H-2, 130–150	108.55	7.78	111.23	36	509	0.0	11.6	387	493	13.7	54.3	2.0	891	68.4	38.2	18.27	1.08	72.14	—
13H-5, 130–150	112.85	7.77	109.82	35	506	0.0	11.3	390	392	11.2	54.3	2.2	895	68.5	22.0	18.40	0.91	71.89	—
14H-2, 130–150	117.91	7.81	105.25	34	499	0.2	11.6	373	476	13.3	53.6	2.2	882	66.5	16.6	21.08	2.02	70.72	—
14H-5, 130–150	122.41	7.88	106.63	35	498	0.0	10.9	359	491	13.9	53.0	2.2	904	67.6	28.8	21.47	1.05	74.16	—
15H-2, 130–150	127.90	7.55	103.71	34	496	0.0	8.0	352	480	13.6	52.5	2.6	875	65.2	38.0	20.19	1.86	73.55	—
15H-5, 124–144	132.34	7.70	100.39	34	494	0.4	9.3	294	478	13.9	50.5	2.6	765	68.0	25.7	20.16	2.57	74.79	—
16H-2, 130–150	137.40	7.91	102.77	35	492	0.0	10.9	299	476	14.3	50.0	2.3	780	73.8	7.8	21.03	1.09	76.33	34.42
16H-5, 121–141	141.81	7.82	—	34	482	0.2	10.1	295	469	13.9	45.6	3.8	733	67.8	12.1	21.20	0.99	74.15	—
17H-2, 130–150	146.90	8.14	98.03	34	488	0.0	9.0	294	470	13.3	—	—	—	—	—	—	—	—	26.55
17H-5, 80–100	150.90	7.73	—	32	487	0.1	9.6	317	472	13.7	—	—	—	—	—	—	—	—	—
19H-2, 130–150	158.16	7.75	—	33	482	0.0	11.2	327	464	13.0	44.9	2.9	788	72.4	17.9	25.63	0.33	83.86	21.18
19H-4, 130–150	161.08	7.65	92.31	—	480	0.0	10.6	308	462	13.8	44.4	3.4	857	73.6	9.5	26.80	0.46	84.36	—
20H-2, 130–150	165.98	8.08	90.10	32	480	0.0	10.8	127	373	11.6	42.7	2.8	634	80.1	6.2	26.04	0.00	80.54	19.26
20H-5, 130–150	170.48	7.98	80.38	32	482	2.3	10.6	207	457	13.6	42.8	3.4	731	82.0	11.0	26.06	—	88.81	—
22H-2, 130–150	175.50	7.76	90.78	32	476	0.3	10.9	290	466	13.8	42.8	3.7	812	95.8	6.9	28.67	0.86	87.45	20.80
22H-4, 128–148	178.48	7.82	—	32	477	0.0	11.1	249	460	13.5	39.7	3.6	786	100.0	9.1	29.32	0.81	82.48	—
23H-2, 130–150	185.00	7.87	86.29	32	477	0.0	10.3	154	461	15.2	38.0	3.4	672	113.2	7.2	33.20	0.77	85.27	22.61
23H-4, 102–122	187.72	7.85	86.68	32	480	0.0	9.8	209	463	13.6	39.4	4.1	765	111.8	4.6	33.38	1.75	79.94	13.94
26X-2, 130–150	207.00	7.81	—	30	463	0.0	10.8	214	448	12.5	36.0	3.5	746	94.9	7.4	33.75	1.26	80.83	19.05
26X-4, 130–150	209.88	7.79	73.42	30	458	0.4	10.0	224	450	12.6	34.9	3.6	743	95.1	11.2	35.48	1.68	82.08	—
27X-2, 125–150	216.25	7.75	71.86	30	452	0.0	9.1	218	440	12.2	32.8	3.7	756	105.3	16.1	39.38	2.44	80.73	19.05
27X-5, 125–150	220.75	7.74	67.66	30	450	0.5	10.2	216	439	11.8	33.0	3.5	770	93.1	16.4	40.74	2.71	80.78	—
28X-2, 125–150	225.85	7.74	66.94	30	449	0.0	9.7	197	434	11.5	31.5	2.9	801	103.0	20.4	41.17	0.63	80.99	14.10
28X-4, 125–150	228.85	7.79	64.48	30	449	0.0	9.4	183	435	11.2	30.6	2.9	747	97.9	13.2	38.23	0.28	82.67	—
29X-2, 125–150	235.55	7.69	61.77	28	449	0.7	9.7	116	433	11.4	28.6	3.0	756	100.7	13.4	38.15	0.40	85.71	—
30X-2, 125–150	245.15	7.72	59.50	28	448	0.0	9.8	148	431	11.4	26.5	3.2	714	117.3	13.1	38.91	0.48	86.58	14.71
30X-4, 110–135	248.00	7.70	56.48	28	443	0.0	9.5	148	432	11.1	27.2	3.1	748	118.3	8.4	40.98	0.92	88.19	—
31X-2, 116–141	254.76	7.98	54.78	28	445	0.3	9.8	90	429	11.0	25.9	3.0	819	128.6	7.1	47.31	0.46	96.15	5.47
32X-2, 125–150	264.45	7.69	51.76	27	447	0.0	9.5	81	424	10.7	23.9	3.3	849	168.4	7.1	53.60	0.73	103.91	9.05
33X-2, 125–150	274.05	7.68	48.24	27	440	0.5	9.6	57	428	10.6	21.3	3.2	937	189.7	2.5	53.81	0.25	121.91	9.40

Table T4 (continued).

Core, section, interval (cm)	Depth (mbsf)	pH	Alkalinity (mM)	Salinity (g/kg)	Cl (mM)	SO_4 (mM)	NH_4 (mM)	PO_4 (µM)	Na (mM)	K (mM)	Mg (mM)	Ca (mM)	B (µM)	Ba (µM)	Fe (µM)	Li (µM)	Mn (µM)	Sr (µM)	DOC (mM)
33X-5, 125–150	278.55	7.60	46.45	27	438	0.0	9.3	52	423	10.3	20.5	3.0	—	—	—	—	—	—	—
34X-2, 128–148	283.78	7.65	40.23	27	435	1.1	9.0	50	428	9.9	20.4	3.0	—	—	—	—	—	—	—
34X-5, 130–150	288.13	7.60	39.63	27	440	1.8	8.9	40	431	10.3	21.0	3.8	—	—	—	—	—	—	—
36X-2, 130–150	295.40	7.61	42.89	26	436	0.7	8.4	44	424	9.7	19.2	4.0	—	—	—	—	—	—	8.36
36X-5, 80–100	299.40	7.83	41.78	26	437	0.0	9.1	26	423	9.9	18.4	4.1	893	239.6	0.7	63.67	0.41	130.51	—
37X-3, 130–150	304.90	7.52	20.28	26	434	1.0	8.2	40	421	9.2	17.8	4.3	965	193.0	2.7	67.58	0.46	140.32	6.97
38X-3, 130–150	314.60	7.98	39.66	26	433	1.0	8.3	24	423	8.9	16.5	4.5	912	247.8	0.7	68.72	0.64	124.38	7.38
39X-3, 130–150	324.20	7.56	33.79	26	437	4.7	8.3	21	428	8.6	19.6	6.0	942	15.4	0.1	60.81	1.04	164.84	—
41X-2, 130–150	333.40	7.45	36.49	26	435	1.6	8.1	24	427	9.5	14.8	6.1	1309	275.7	2.0	65.93	1.80	171.86	7.74
42X-3, 130–150	343.50	7.49	33.82	26	432	0.6	8.3	21	413	7.8	13.3	6.1	1316	281.6	19.1	67.94	1.86	180.59	6.38
43X-2, 130–150	351.60	7.61	32.64	26	433	1.6	7.9	15	415	7.6	13.2	6.6	1321	258.1	5.5	69.85	2.24	184.51	6.14
44X-3, 130–150	362.70	7.45	30.89	26	434	1.6	7.0	11	404	6.9	12.5	6.6	1323	252.6	1.0	69.52	1.07	183.30	20.71
45X-3, 130–150	372.30	7.57	29.47	26	437	1.9	8.0	9	418	7.2	12.2	7.2	1180	214.3	0.8	69.38	0.54	194.82	5.00
46X-3, 130–150	381.90	7.52	27.77	26	438	—	7.5	1	409	6.6	11.8	7.1	1240	223.1	2.3	74.19	0.90	193.83	4.03
47X-3, 130–150	391.60	7.48	26.57	26	433	0.7	6.9	11	412	6.5	11.9	7.5	1341	174.8	2.4	77.06	1.96	200.68	3.02
49X-3, 130–150	402.20	7.67	23.43	26	437	1.7	6.6	5	425	5.6	11.5	6.7	1179	166.1	0.3	75.72	1.56	201.98	3.12
50X-3, 130–150	410.80	7.78	22.63	26	432	2.4	6.1	7	425	5.6	11.0	6.9	1297	174.8	BDLL	82.06	2.51	211.02	2.89
51X-3, 130–150	420.50	7.79	22.19	25	433	1.8	6.3	5	424	5.1	11.3	7.7	1148	177.7	BDLL	80.76	2.32	205.90	3.36
52X-3, 130–150	430.10	7.74	20.14	25	434	1.5	5.9	5	425	4.8	10.9	7.5	1303	94.1	3.0	84.00	5.14	207.98	—
53X-3, 130–150	439.78	7.79	18.26	26	432	2.4	5.5	3	427	4.6	10.4	7.3	1178	101.7	2.5	83.71	4.31	—	2.81
204-1251C-																			
1H-2, 140–150	2.90	8.30	27.31	35	553	—	1.5	112	—	—	—	—	652	11.4	4.4	20.41	BDL	84.29	—
1H-5, 140–150	7.40	7.91	59.61	35	551	—	4.1	271	—	—	—	—	792	73.9	8.6	13.15	0.51	79.62	—
2X-1, 140–150	9.50	7.72	71.98	36	—	—	5.2	344	—	—	—	—	—	—	—	—	—	—	—
2X-3, 130–150	11.97	7.62	88.49	36	—	—	6.5	290	—	—	—	—	—	—	—	—	—	—	—
204-1251D-																			
1X-1, 140–150	1.40	7.78	30.30	35	553	11.1	1.9	60	486	12.0	—	—	683		BDL	19.52	BDL	79.31	—
1X-2, 90–100	2.40	7.88	48.85	34	551	0.8	2.8	109	486	12.2	—	—	799	37.8	BDL	15.30	BDL	83.79	—
2X-1, 140–150	9.50	7.69	75.43	36	546	1.1	5.7	338	500	12.8	—	—	994	35.3	7.6	11.62	BDL	74.87	—
2X-3, 60–70	11.20	—	—	—	543	—	—	—	—	—	—	—	—	—	—	—	—	—	—
3X-2, 140–150	20.50	7.62	97.21	37	543	0.9	7.8	328	509	13.7	—	—	1083	34.8	48.8	11.71	0.02	73.35	—
3X-4, 140–150	23.50	7.67	101.87	38	—	0.5	8.5	280	511	14.4	—	—	1038	36.9	74.8	12.83	0.17	69.67	—
4H-2, 140–150	29.80	7.58	104.33	38	542	—	9.5	335	—	—	—	—	1086	46.3	18.9	16.04	BDL	63.10	—
4H-4, 140–150	32.75	7.64	105.81	38	542	—	10.4	377	—	—	—	—	1161	46.2	18.9	17.05	BDL	62.08	—
5H-5, 0–10	42.40	7.65	118.58	38	542	—	11.3	360	—	—	—	—	1170	52.7	38.3	15.77	0.83	70.24	—
7H-3, 135–150	52.07	7.70	115.20	38	535	—	12.3	395	—	—	—	—	1211	55.8	35.4	16.29	1.13	70.93	—
8H-5, 135–150	64.75	7.70	96.58	36	528	—	13.6	364	—	—	—	—	1156	48.2	13.7	17.77	0.29	60.16	—
11H-4, 0–15	82.29	7.84	109.65	37	—	—	14.4	391	—	—	—	—	1007	47.7	19.0	18.01	0.61	71.41	—
11H-4, 135–150	83.64	7.72	110.24	36	518	—	14.8	381	—	—	—	—	1039	49.8	12.7	17.18	0.48	71.30	—
13H-6, 0–20	103.67	7.74	116.09	36	510	—	14.5	387	—	—	—	—	1026	64.9	38.3	20.47	1.82	75.23	—
15H-5, 0–15	122.40	8.16	106.29	35	501	—	12.3	356	—	—	—	—	875	69.2	18.9	21.73	1.72	73.66	—
17H-5, 0–15	141.40	7.77	100.94	34	487	—	11.1	356	—	—	—	—	811	74.9	11.1	21.28	1.67	78.85	—
19H-2, 130–150	156.31	8.00	97.36	34	479	—	11.1	340	—	—	—	—	755	71.2	9.0	23.93	1.27	81.67	—
19H-5, 130–150	160.81	7.80	—	34	476	—	11.1	342	—	—	—	—	794	72.8	14.5	25.17	1.29	84.39	—
20H-2, 125–150	166.13	7.46	91.99	33	476	—	11.5	336	—	—	—	—	793	76.0	19.8	26.05	0.79	87.43	—
20H-5, 125–150	170.63	7.61	92.44	34	476	—	12.1	246	—	—	—	—	642	81.2	5.7	24.93	0.46	84.62	—
22X-1, 20–40	175.60	7.37	91.60	34	478	—	11.8	272	—	—	—	—	670	90.8	7.8	24.32	0.81	91.39	—
22X-3, 0–20	178.37	7.47	92.57	34	485	—	12.0	284	—	—	—	—	695	92.2	12.0	24.79	0.90	89.63	—

Table T4 (continued).

Core, section, interval (cm)	Depth (mbsf)	pH	Alkalinity (mM)	Salinity (g/kg)	Cl (mM)	SO_4 (mM)	NH_4 (mM)	PO_4 (µM)	Na (mM)	K (mM)	Mg (mM)	Ca (mM)	B (µM)	Ba (µM)	Fe (µM)	Li (µM)	Mn (µM)	Sr (µM)	DOC (mM)
23X-2, 122–147	181.82	7.44	93.44	34	484	—	11.7	346	—	—	—	—	794	96.8	25.4	26.02	1.77	89.81	—
23X-3, 125–150	183.32	7.56	93.82	34	485	—	11.9	263	—	—	—	—	707	100.0	10.2	27.53	1.38	90.54	—
24X-2, 0–25	189.62	7.58	85.57	30	458	—	11.3	284	—	—	—	—	668	97.2	14.2	26.63	2.05	82.17	—
24X-3, 0–10	191.12	—	—	—	402	—	—	—	—	—	—	—	659	73.7	8.3	25.87	1.96	65.23	—
24X-3, 140–150	192.52	—	—	—	404	—	—	—	—	—	—	—	625	68.5	5.1	26.50	1.15	62.07	—
24X-4, 43–63	193.05	7.53	71.65	27	393	—	10.0	259	—	—	—	—	639	67.8	4.0	28.86	1.28	65.44	—
25X-2, 125–150	200.95	7.51	86.02	32	470	—	12.0	245	—	—	—	—	710	112.3	8.3	32.96	1.50	86.51	—
25X-5, 125–150	205.45	7.56	82.65	32	465	—	11.6	201	—	—	—	—	658	104.6	11.7	32.70	1.19	81.95	—
26X-3, 130–150	210.43	7.55	78.32	32	460	—	11.1	191	—	—	—	—	679	94.0	23.2	33.84	1.76	82.44	—
204-1251E-																			
1H-1, 85–95	0.85	7.82	5.80	35	551	27.5	0.2	19	484	12.1	—	—	—	—	—	—	—	—	—
1H-1, 140–150	1.40	7.61	7.50	34	548	26.6	0.5	50	487	12.4	—	—	588	4.0	2.1	23.98	0.33	83.74	—
1H-2, 80–90	2.30	7.61	16.81	35	549	19.6	1.5	38	482	12.1	—	—	613	2.1	3.0	22.08	0.50	83.25	—
1H-2, 140–150	2.90	7.68	26.88	35	550	13.5	2.5	69	486	12.0	—	—	677	3.3	0.9	21.11	0.13	81.27	—
1H-3, 60–70	3.60	7.79	37.47	34	551	6.2	3.1	71	484	12.0	—	—	671	4.8	1.7	18.02	0.13	83.08	—
1H-3, 140–150	4.40	7.65	47.10	34	553	1.0	4.0	119	484	11.8	—	—	713	31.7	2.9	15.61	0.18	81.51	—
1H-4, 60–70	5.10	7.60	50.63	34	551	0.0	4.5	81	486	12.1	—	—	707	72.9	2.6	13.60	0.26	83.17	—
1H-4, 140–150	5.90	7.58	52.81	34	553	0.5	4.4	154	486	11.8	—	—	707	75.3	7.4	13.00	0.20	82.46	—

Notes: DOC = dissolved organic carbon. — = no sample was available. BDL = below detection limit.

Table T5. Concentrations of methane, ethane, ethylene, and propane in headspace gas, Holes 1251B, 1251C, and 1251D. (See table note. Continued on next page.)

Core, section, interval (cm)	Depth (mbsf)	C_1 (ppmv)	C_2 (ppmv)	$C_{2=}$ (ppmv)	C_3 (ppmv)	C_1/C_2	C_1 (mM)
204-1251B-							
1H-1, 0–5	0.00	178					0.1
1H-2, 0–5	1.50	28,058	0.7			39,518	5.0
1H-3, 0–5	3.00	28,800	0.7			40,563	5.6
1H-4, 0–5	4.50	63,765	1.7			38,413	5.9
1H-5, 0–5	6.00	39,020	1.3			30,248	4.0
1H-6, 0–5	7.50	14,283					2.7
3H-2, 0–5	20.03	9,728					2.0
3H-5, 0–5	24.51	3,973					0.9
4H-3, 0–5	31.10	14,966		0.3			2.8
4H-6, 0–5	35.60	10,984					1.9
5H-3, 0–5	40.51	13,538					1.8
5H-6, 0–5	44.96	11,843					1.8
6H-3, 0–5	49.32	16,360					2.2
6H-6, 0–5	53.71	6,506					1.9
7H-3, 0–5	59.60	13,459					1.8
7H-6, 0–5	64.10	5,868					1.6
8H-3, 0–5	69.10	15,398	0.7			20,808	2.1
8H-6, 0–5	73.48	1,926					0.3
10H-2, 0–5	86.60	15,072	0.6	0.5		27,404	2.3
11H-3, 0–5	97.04	8,259					3.4
13H-3, 0–5	108.75	16,337					2.5
13H-6, 0–5	113.05	22,896	1.2	0.9		18,922	3.1
14H-3, 0–5	118.11	11,008	1.5			7,388	1.6
14H-6, 0–5	122.61	22,061	1.4	0.6		15,986	2.7
15H-3, 0–5	128.10	16,986	1.3	0.7		12,966	2.7
15H-6, 0–5	132.54	12,950	0.9	0.9		15,235	2.6
16H-3, 0–5	137.60	11,679	0.7			15,782	1.9
16H-6, 0–5	142.01	12,477	0.7			18,083	4.2
17H-3, 0–5	147.10	15,445		0.4			3.2
17H-6, 0–5	151.10	12,477	0.7	0.4		18,083	2.4
19H-3, 0–5	158.36	81,577	2.2	0.4		37,593	13.2
20H-3, 0–5	166.18	11,398	1.0			11,873	1.9
22H-3, 0–5	175.70	1,266					0.2
23H-3, 0–5	185.20	13,044	0.6			21,384	2.3
26X-3, 0–5	207.20	11,765	10.6			1,110	2.0
27X-3, 0–5	216.50	19,214	8.9	0.6		2,159	2.9
27X-6, 0–5	221.00	14,570	9.4	0.8		1,550	2.5
28X-3, 0–5	226.10	16,110	13.1	0.8		1,230	2.4
29X-3, 0–5	235.80	62,691	14.6	0.5		4,294	9.6
30X-3, 0–5	245.40	568					0.1
31X-3, 0–5	255.01	24,794	16.0	2.1		1,552	3.7
32X-3, 0–5	264.70	14,622	16.2	1.5		902	2.2
33X-3, 0–5	274.30	20,345	21.8	0.7		932	2.9
34X-3, 0–5	283.98	11,035	9.5	0.8		1,166	3.0
36X-3, 0–5	295.60	16,685	25.1	1.6		666	2.7
37X-3, 0–5	303.60	14,719	18.1	0.9		811	2.2
38X-4, 0–5	314.80	14,707	26.1	0.3	3.9	563	2.6
39X-4, 0–5	324.40	15,703	14.6	0.6		1,077	3.9
41X-3, 0–5	333.60	19,691	17.1		1.1	1,153	4.2
42X-4, 0–5	343.70	39,152	29.2			1,341	6.0
43X-3, 0–5	351.80	23,779	22.6		4.9	1,052	3.6
44X-3, 0–5	361.40	28,771	26.5	1.2		1,086	4.2
45X-4, 0–5	372.50	6,510	4.7			1,373	1.1
46X-4, 0–5	382.10	16,505	7.5			2,204	3.4
47X-4, 0–5	391.80	13,957	9.9	0.8		1,411	2.5
49X-4, 0–5	402.40	3,099	1.7			1,823	0.8
50X-4, 0–5	411.00	5,756	4.3		0.8	1,342	1.4
51X-4, 0–5	420.70	19,309	9.2		0.7	2,092	3.9
52X-4, 0–5	430.30	22,026	11.3			1,951	5.3
53X-4, 0–5	439.98	14,457	7.8			1,851	2.9
204-1251C-							
1H-1, 0–5	0.00	138					0.0
1H-2, 0–5	1.50	188					0.0
1H-3, 0–5	3.00	48					0.0
1H-4, 0–5	4.50	8,669					1.8

Table T5 (continued).

Core, section, interval (cm)	Depth (mbsf)	C_1 (ppmv)	C_2 (ppmv)	$C_{2=}$ (ppmv)	C_3 (ppmv)	C_1/C_2	C_1 (mM)
1H-5, 0–5	6.00	44,809					10.2
1H-6, 0–5	7.50	42,241	1.03			41,011	8.2
2X-1, 0–5	8.10	38,017	0.73			52,078	8.6
2X-2, 0–5	9.60	39,561	0.88			44,956	8.3
2X-3, 0–5	10.67	29,845	0.77			38,760	5.9
2X-4, 0–5	12.17	23,092	0.74			31,205	4.8
204-1251D-							
15H-4, 0–5	120.90	19,997	0.73			27,393	
16H-2, 0–5	127.40	17,853	0.91			19,619	
17H-4, 0–5	139.90	23,582	1.49			15,827	
18H-2, 0–5	145.94	7,873	0.49			16,067	
19H-3, 0–5	156.51	16,220	1.08			15,019	
20H-3, 0–5	166.38	14,670	0.79			18,570	
22H-1, 0–5	175.40	18,489	1.06			17,442	
22H-2, 0–5	176.87	12,822	0.82			15,637	
23H-1, 0–5	179.10	9,073	0.55			16,496	
23H-4, 0–5	183.57	11,167	0.81			13,786	
24H-2, 0–5	189.62	9,844					
24H-4, 0–5	192.62	9,139	0.51			17,920	
25H-2, 0–5	199.70	9,810	7.84			1,251	
25H-4, 0–5	202.70	22,295	19.92			1,119	
26H-4, 0–5	210.63	10,633	6.10			1,743	
27H-4, 0–5	221.30	10,805	7.44			1,452	

Note: C_1 = methane, C_2 = ethane, $C_{2=}$ = ethylene, C_3 = propane.

Table T6. Concentration of light hydrocarbon and nonhydrocarbon gases in VAC samples of core gas voids, Holes 1251B, 1251C, and 1251D. (**See table note.** Continued on next page.)

Core, section, interval (cm)	Depth (mbsf)	C_1 (ppmv)	C_2 (ppmv)	C_3 (ppmv)	*i*-C_4 (ppmv)	H_2S (ppmv)	CO_2 (ppmv)	O_2 (ppmv)	N_2 (ppmv)	C_1/C_2
204-1251B-										
1H-4, 68–69	5.18	663,474	3.3			610	15,090	60,042	251,629	198,645
3H-1, 82–83	19.42	90,017					806	20,744	79,400	
3H-2, 120–121	21.23	887,044	7.9	3.0						112,426
3H-2, 120–121	21.23	922,877	3.6				44,734	4,086	16,097	257,787
3H-3, 51–52	22.04	939,078	3.4				40,518	1,474	5,746	274,584
3H-4, 102–103	24.03	854,363	2.8				30,037	23,025	88,085	302,966
4H-3, 20–21	31.30	942,068	2.4				32,903	1,741	8,495	399,181
4H-7, 16–17	36.60	751,581					44,141	40,789	159,897	
5H-1, 95–96	38.55	971,173	8.7				14,439	170	1,203	111,886
6H-2, 5–6	47.97	940,826		4.5			36,295	1,160	7,280	
6H-4, 101–102	51.83	971,082	8.6	7.2			13,931	1,001	1,294	113,444
6H-4, 101–102	51.83	928,978	15.2							60,957
7H-1, 149–150	58.09	959,879	2.2				25,512	82	1,066	442,341
7H-6, 33–34	64.43	967,618	3.9	3.1			16,904	1,521	1,593	250,030
8H-3, 82–83	69.92	973,448	6.9				9,621	677	1,509	140,672
8H-4, 82–83	71.42	956,153	4.8				23,575	2,320	5,648	199,614
8H-6, 93–94	74.41	943,218					43	811	1,380	
10H-1, 149–150	86.59	878,158	7.2	8.2						122,136
10H-1, 149–150	86.59	887,884	2.4	4.7	3.6		79,191	6,296	23,172	368,417
10H-4, 87–88	90.47	964,826	3.5				19,575	964	1,456	274,879
11H-2, 32–33	96.42	889,260	16.1				29,308	15,561	57,521	55,406
13H-5, 37–38	111.92	975,681	33.2				7,364	1,965	1,552	29,370
14H-3, 33–34	118.44	909,774	9.8	5.3			14,615	14,253	55,463	93,119
14H-5, 129–130	122.40	826,336	7.1	5.6			16,433			117,211
15H-2, 27–28	126.87	933,370	9.5	7.2			41,174	2,401	12,142	98,249
15H-6, 14–15	132.68	950,428	7.9	5.8			17,900	2	31	120,307
16H-2, 42–43	136.52	796,595	19.9				17,777	36,970	141,455	40,070
16H-6, 16–17	142.17	958,899	11.2	6.9			18,876	1,524	1,280	85,616
17H-5, 100	151.10	957,977	10.8	6.5			21,651	1,138	1,050	88,374
17H-6, 0–1	151.10	956,395	9.5	6.5			22,253	1,643	1,226	100,462
19H-1, 17–18	155.77	954,905	28.4	5.2			26,445	96	1,333	33,576
19H-6, 17–18	162.89	949,159	10.1	6.6			31,665	89	1,165	93,976
20H-2, 1–2	164.69	966,145	14.3	6.2			17,470	60	1,333	67,563
20H-5, 142–143	170.60	960,576	50.7				5,810	4,330	11,484	18,931
22H-1, 93–94	173.63	913,661	13.7	13.1			47,231	2,501	26,262	66,788
22H-5, 120–121	179.88	943,382	10.5	15.1			35,737	1,216	9,815	89,846
23H-4, 122–123	187.92	975,814	7.2	11.2	7.2		12,005	90	1,272	135,718
26X-2, 119–120	206.89	950,476	229							4,158
26X-5, 10–11	210.18	536,925	112							4,796
26X-5, 10–11	210.18	523,622	118				18,324	90,961	355,053	4,456
27X-5, 35–36	219.85	980,448	117				9,849	52	517	8,394
28X-2, 41–42	225.01	801,069	119	4.3			15,094	37,474	142,865	6,732
28X-5, 27–28	229.37	943,040	128	4.1						7,391
29X-3, 17–18	235.97	949,286	113	7.6						8,423
29X-4, 13–14	237.43	969,628	109	5.0	3.1		15,376	1,130	1,019	8,879
30X-4, 130–131	248.20	844,973	105	4.8			22,404	26,534	100,864	8,017
31X-2, 0–1	253.60	959,192	150	8.3	5.7		25,175	2,329	1,534	6,378
31X-4, 0–1	256.51	968,414	124	5.6	3.7		7,167	2,298	1,532	7,810
32X-1, 106–107	262.76	922,295	177	7.4	4.9		24,549	6,933	35,744	5,216
32X-4, 84–85	267.04	934,760	182	6.3	3.8		17,646	5,310	33,176	5,129
34X-2, 102–103	283.52	943,070	214	5.4						4,415
34X-2, 102–103	283.52	947,467	209	6.8			12,320	6,227	17,602	4,536
37X-3, 2–3	303.62	973,461	223	6.7			10,603	84	858	4,362
38X-6, 5–6	317.74	967,284	231	7.6			13,257	1,157	1,147	4,196
39X-3, 140–141	324.30	959,930	209	8.8			7,574	88	847	4,583
41X-2, 140–141	333.50	968,896	207	10.0			7,783	93	1,049	4,690
41X-4, 5–6	335.15	973,624	208	10.4						4,685
41X-4, 5–6	335.15	965,021	200	9.7			5,985	1,337	1,162	4,832
42X-2, 75–76	341.45	964,647	244	12.6			1,586	73	952	3,960
43X-6, 82–83	357.09	946,324	303	25.8	5.1		27,602	1,938	3,826	3,126
44X-6, 55–56	366.45	965,649	202	9.6			10,514	2,654	3,161	4,788
45X-4, 52–53	373.02	957,343	176	7.4			14,978	2,566	6,344	5,436
46X-3, 100–101	381.61	965,019	153	6.1		13	9,516	1,564	2,278	6,301
47X-4, 124–125	393.04	973,548	139	5.7			6,816	1,242	1,209	7,000
49X-2, 102–103	400.42	976,573	138	5.5			10,120	1,664	1,349	7,095

Table T6 (continued).

Core, section, interval (cm)	Depth (mbsf)	C_1 (ppmv)	C_2 (ppmv)	C_3 (ppmv)	*i*-C_4 (ppmv)	H_2S (ppmv)	CO_2 (ppmv)	O_2 (ppmv)	N_2 (ppmv)	C_1/C_2
50X-3, 5–6	409.55	973,932	153	6.4			13,600	1,061	1,111	6,360
51X-5, 44–45	422.57	971,211	126	4.8			5,018	61	779	7,733
52X-5, 98–99	432.78	967,073	115				3,435	1,419	1,302	8,393
53X-2, 112–113	438.10	976,937	123				4,715	72	795	7,962
204-1251C-										
2X-3, 75–76	11.42	945964	6.7				25674	1420	11260	140,559
2X-4, 33–34	12.50	725956	5.9				3771789	46154	185664	122,215
204-1251D-										
16H-1, 135–136	127.25	930,682	7.4	6.0			26,115	1,725	31,136	126,109
17H-1, 120–121	136.60	876,006	10.2	6.1	4.8		26,897	2,418	18,369	85,883
19H-2, 67–68	155.68	888,442	9.7	6.3			24,231	1,235	4,410	91,403
20H-2, 26–27	165.14	959,098	10.7	6.1			21,338	1,552	4,421	89,552
20H-4, 119–120	169.07	900,003	9.7	5.8			16,903	15,785	62,050	92,976
22X-1, 20–21	175.60	569,189	12.3				32,858	75,155	287,021	46,464
22X-2, 123–124	178.10	421,803	9.8				28,072	106,458	382,854	43,085
23X-2, 15–16	180.75	907,069	12.0	27.9	5.4		59,313	6,528	22,411	75,842
23X-4, 4–5	183.61	758,762	10.1	20.4	3.6		39,935	41,418	162,255	74,902
25X-2, 106–107	200.76	896,623	191				28,505	15,542	55,790	4,691
25X-3, 33–34	201.53	850,938	199				29,838	26,389	100,125	4,275
26X-4, 14–15	210.79	968,426	253				14,592	91	3,301	3,830

Note: C_1 = methane, C_2 = ethane, C_3 = propane, *i*-C_4 = isobutane, H_2S = hydrogen sulfide, CO_2 = carbon dioxide, O_2 = oxygen, N_2 = nitrogen.

Table T7. Composition of gas samples from PCS experiments, Hole 1251B. (See table note. Continued on next page.)

Sample	Volume (mL)	C_1 (ppm)	C_2 (ppm)	C_3 (ppm)	*i*-C_4 (ppm)	*n*-C_4 (ppm)	*i*-C_5 (ppm)	*n*-C_5 (ppm)	*i*-C_6 (ppm)	*n*-C_6 (ppm)	O_2 (ppm)	N_2 (ppm)	CO_2 (ppm)	C_1/C_2
204-1251B-12P (104.1 mbsf)														
G1	82	295,864									104,746	566,687	2,076	116,187
G2	250	639,002									37,576	317,158	1,847	
G3	370	793,304	7.1								17,591	186,025	1,307	
G4	320	856,824	7.2								11,295	125,628	2,094	
G5	300	801,367	8.3								26,732	169,437	2,413	
G6	270	874,737	9.2								7,709	107,910	2,882	
G7	260	802,375	7.9								15,074	176,272	2,993	
G8	130	790,145	7.0								10,996	137,263	4,705	
G9	120	820,597	9.0								12,470	121,605	5,814	
G10	90	856,143	8.7								13,386	117,831	5,940	
G11	90	863,230	10.0								11,784	114,719	3,740	
204-1251B-18P (153.6 mbsf)														
G1	50	155,702	235	13.7							131,665	674,054		53,157
G2	720	2,160									162,203	755,124		
G3	480	631,817	7.3								43,457	319,953		
G4	700	645,220	7.7								48,878	301,381		
G5	330	695,500	8.6	4.6							27,596	271,077	87	
G6	450	667,863	8.4	4.7							37,676	286,628	3,615	
G7	210	177,590	10.2	5.7							136,930	628,167	1,921	
G8	100	583,013	10.6	5.8							52,821	350,407	3,410	
G9	70	657,093	12.4	6.7							34,011	299,197	3,881	
G10	40	512,848	10.5	6.3							63,808	406,256	2,325	
204-1251B-35P (290.6 mbsf)														
G1	90	732,487	164	6.4	3.8						48,965	210,751	1,150	4,522
G2	250	951,616	240	6.2	3.4						2,372	7,773	393	
G3	520	957,270	211	4.7							1,516	1,641	311	
G4	390	963,141	203	4.8							3,789	12,340	313	
G5	250	976,460	206	5.1	3.1						1,185	3,182	683	
G6	210	976,898	206	5.1	3.1						47	1,348	612	
G7	210	969,366	204	5.0							2,755	12,022	567	
G8	260	965,775	206	5.1	3.1						2,225	11,069	883	
G9	270	937,510	213	5.7	3.6						9,686	44,536	1,472	
G10	180	954,744	220	6.3	3.8						2,020	18,323	2,182	
G11	80	951,742	228	6.6	3.9						2,698	22,180	2,221	
G12	110	954,567	230	7.2	4.6						1,689	19,088	2,303	
G13	70	893,409	219	5.7	4.3						15,153	74,360	1,838	
204-1251D-6P (45.9 mbsf)														
G1	82	295,864				3.6					104,746	566,687	2,076	112,169
G2	250	639,002				5.6					37,576	317,158	1,847	
G3	370	793,304	7.1		4.3						17,591	186,025	1,307	
G4	320	856,824	7.2		3.3						11,295	125,628	2,094	
G5	300	801,367	8.3								26,732	169,437	2,413	
G6	270	874,737	9.2		3.5						7,709	107,910	2,882	
G7	260	802,375	7.9		5.8						15,074	176,272	2,993	
G8	130	790,145	7.0		4.6						10,996	137,263	4,705	
G9	120	820,597	9.0		4.8						12,470	121,605	5,814	
G10	90	856,143	8.7		6.0						13,386	117,831	5,940	
G11	90	863,230	10.0		9.0						11,784	114,719	3,740	
204-1251D-10P (76.4 mbsf)														
G1	100	221,832									106,621	625,188	2,091	949,503
G2	260	672,836									27,736	294,695	2,649	
G4	390	671,452	2.6								30,119	239,599	2,007	
G5	370	532,450									51,074	361,618	3,355	
G6	220	686,354									16,299	239,209	5,394	
G7	130	679,171		4.1							29,654	281,706	7,476	
G8	160	1,024									162,670	753,067	629	
204-1251D-21P (173.4 mbsf)														
G1	70	218,474												93,206
G2	380	604,862	6.3								49,439	336,870	2,090	
G3	420	644,367												
G4	420	658,762	6.8	4.1							35,850	296,267	1,580	
G5	550	660,133	6.9	4.6							33,157	298,931	2,332	
G6	390	604,888	5.5	4.6				4.3			42,991	339,496	2,658	
G7	320	605,531												
G8	240	612,495	7.7	5.7							32,154	342,556	4,621	

Table T7 (continued).

Sample	Volume (mL)	C_1 (ppm)	C_2 (ppm)	C_3 (ppm)	*i*-C_4 (ppm)	*n*-C_4 (ppm)	*i*-C_5 (ppm)	*n*-C_5 (ppm)	*i*-C_6 (ppm)	*n*-C_6 (ppm)	O_2 (ppm)	N_2 (ppm)	CO_2 (ppm)	C_1/C_2
G9	70	606,590	8.5	6.0							29,179	351,755	3,960	
G10	100	577,879	8.1	6.3							30,296	377,080	4,516	
204-1251D-29P (227.5 mbsf)														
G1	40	253,845	26.0		13.5						125,463	576,408	727	7,440
G2	130	904,356	136		5.4						12,628	69,959	1,212	
G3	240	973,108	144								82	6,867	1,119	
G4	460	954,272	125								3,880	22,050	1,171	
G5	300	945,082	119		5.6						2,808	33,448	1,814	
G6	180	932,570	116		7.2						2,181	48,406	1,401	
G7	190	794,189	104	3.2	8.8						1,339	39,380	1,520	
G8	110	893,346	122		11.2						1,680	40,386	1,991	
G9	90	919,112	127		13.6						4,100	60,543	2,221	
G10	165	929,229	135		14.4						2,878	47,674	2,744	
204-1251G-2P (20.0 mbsf)														
G1	50	86,051									137,326	709,128	897	146,828
G2	160	739,362	4.6	9.1							10,339	148,463	1,367	
G3	410	886,951	6.0								1,775	85,326	3,329	
G4	300	825,237	4.6								18,671	141,710	6,051	
G5	10	868,271	6.3								2,424	115,019	5,661	
G6	10	843,117	6.2								3,325	140,325	5,275	
G7	10	803,068	6.2								9,357	178,823	3,689	

Note: C_1 = methane, C_2 = ethane, C_3 = propane, *i*-C_4 = isobutane, *n*-C_4 = normal butane, *i*-C_5 = isopentane, *n*-C_5 = normal pentane, *i*-C_6 = isohexane, *n*-C_6 = normal hexane, O_2 = oxygen, N_2 = nitrogen, CO_2 = carbon dioxide.

Table T8. Carbonate carbon, calcium carbonate, total carbon, organic carbon, total nitrogen, and total sulfur contents and C/N ratios, Hole 1251B.

Core, section, interval (cm)	Depth (mbsf)	Carbonate carbon (wt%)	$CaCO_3$ (wt%)	Total carbon (wt%)	Organic carbon (wt%)	Total nitrogen (wt%)	Total sulfur (wt%)	C/N
204-1251B-								
1H-3, 76–77	3.76	0.38	3.17	2.19	1.81	0.22	0.84	8.23
3H-3, 74–75	22.27	0.48	3.98	1.54	1.06	0.15	0.21	7.07
4H-3, 74–75	31.84	0.56	4.64	2.01	1.45	0.20	1.01	7.25
5H-3, 58–59	41.09	0.47	3.90	1.71	1.24	0.19	0.43	6.53
6H-3, 75–76	50.07	0.55	4.55	1.82	1.27	0.17	0.77	7.47
7H-3, 75–76	60.35	0.38	3.13	1.86	1.48	0.21	0.50	7.05
8H-3, 87–88	69.97	0.71	5.88	1.73	1.02	0.16	0.41	6.38
10H-3, 77–78	88.87	0.22	1.83	1.68	1.46	0.21	0.48	6.95
11H-3, 77–78	97.81	NA	NA	1.26	NA	0.15	0.24	8.40
14H-3, 76–77	118.87	0.81	6.72	2.18	1.37	0.18	0.32	7.61
15H-3, 82–83	128.92	0.13	1.05	1.13	1.00	0.15	0.31	6.67
16H-3, 79–80	138.39	0.40	3.31	1.75	1.35	0.19	0.46	7.11
17H-3, 76–77	147.86	0.09	0.78	1.61	1.52	0.19	0.37	8.00
19H-3, 75–76	159.11	0.66	5.50	1.86	1.20	0.16	0.27	7.50
20H-3, 76–77	166.94	0.38	3.20	1.50	1.12	0.16	0.17	7.00
23H-3, 75–76	185.95	0.16	1.35	1.47	1.31	0.19	0.80	6.89
26X-3, 38–39	207.58	0.53	4.40	1.67	1.14	0.16	0.18	7.13
27X-3, 77–78	217.27	0.11	0.92	1.22	1.11	0.18	0.97	6.17
28X-3, 76–77	226.86	0.79	6.56	2.54	1.75	0.20	0.49	8.75
29X-3, 78–79	236.58	0.83	6.94	2.19	1.36	0.18	0.37	7.56
30X-3, 77–78	246.17	0.50	4.19	1.64	1.14	0.15	0.45	7.60
31X-3, 77–78	255.78	1.91	15.92	3.57	1.66	0.20	0.69	8.30
32X-3, 77–78	265.47	0.04	0.30	2.05	2.01	0.21	1.05	9.57
33X-3, 77–78	275.07	0.86	7.13	2.00	1.14	0.14	0.68	8.14
34X-3, 70–71	284.68	2.19	18.27	3.47	1.28	0.17	0.69	7.53
36X-3, 88–89	296.48	0.72	5.97	1.66	0.94	0.14	1.13	6.71
37X-3, 54–55	304.14	0.15	1.23	2.04	1.89	0.15	1.11	12.6
38X-3, 36–37	313.66	0.07	0.59	0.80	0.73	0.14	1.02	5.21
41X-3, 18–19	333.78	2.11	17.57	3.42	1.31	0.17	0.90	7.71
41X-3, 75–76	334.35	0.07	0.57	1.59	1.52	0.21	1.09	7.24
42X-3, 80–81	343.00	0.48	4.00	1.06	0.58	0.11	0.52	5.27
43X-3, 68–69	352.48	0.12	1.02	3.18	3.06	0.31	1.77	9.87
44X-3, 73–74	362.13	0.29	2.39	1.67	1.38	0.19	1.01	7.26
45X-3, 67–68	371.67	0.17	1.43	1.08	0.91	0.15	0.27	6.07
46X-3, 69–70	381.29	0.26	2.13	1.51	1.25	0.18	0.52	6.94
47X-3, 89–90	391.19	0.07	0.59	1.55	1.48	0.19	1.33	7.79
50X-3, 81–82	410.31	0.18	1.50	1.94	1.76	0.22	0.97	8.00
52X-3, 71–72	429.51	0.12	0.96	1.74	1.62	0.20	0.92	8.10
53X-3, 111–112	439.59	0.18	1.51	1.56	1.38	0.19	0.61	7.26

Note: NA = not analyzed.

Table T9. Rock-Eval pyrolysis of samples, Hole 1251B.

Core, section, interval (cm)	Depth (mbsf)	Organic carbon (wt%)	S_1 (mg/g)	S_2 (mg/g)	Production index ($S_1/[S_1+S_2]$)	Hydrogen index (mg S_2/g C)	T_{max} (°C)
204-1251B-							
1H-3, 76–77	3.76	1.81	0.62	3.59	0.15	198	401
10H-3, 77–78	88.87	1.46	0.40	2.10	0.16	144	395
17H-3, 76–77	147.86	1.52	0.37	2.15	0.15	141	401
28X-3, 76–77	226.86	1.75	0.40	2.75	0.13	157	413
32X-3, 77–78	265.47	2.01	0.00	0.12	0.00	6	539
42X-3, 80–81	343.00	0.58	0.00	0.49	0.00	84	NA
52X-3, 71–72	429.51	1.62	0.29	1.85	0.14	114	398

Note: NA = not analyzed.

Table T10. Intervals sampled for microbiology, Holes 1251B, 1251D, and 1251E.

Core, section, interval (cm)	Depth (mbsf)
204-1251B-	
1H-1, 50–51	0.50
28X-4, 15–125	227.75
33X-5, 20–125	277.50
39X-3, 0–130	322.90
45X-5, 0–150	374.00
51X-3, 0–130	419.20
204-1251D-	
3X-4, 0–140	22.10
4H-4, 0–140	31.35
5H-5, 10–150	42.50
8H-5, 0–135	63.40
11H-4, 77–135	83.06
13H-6, 105–150	104.72
15H-5, 53–150	122.93
17H-5, 60–150	142.00
20H-5, 25–125	169.63
22X-3, 20–55	178.57
22X-3, 80–110	179.17
25X-5, 0–125	204.20
204-1251E-	
1H-1, 0–85	0.00
1H-1, 95–140	0.95
1H-2, 0–80	1.50
1H-2, 90–140	2.40
1H-3, 0–60	3.00
1H-3, 70–140	3.70
1H-4, 0–60	4.50
1H-4, 70–140	5.20

Table T11. Core quality indicators in intervals sampled for microbiology, Holes 1251C, 1251D, and 1251E.

Core, section, interval (cm)	Depth (mbsf)	PFT per sample (ag)		Microspheres per gram	
		Inside core	Outer edge	Inside core	Outer edge
204-1251B-					
28X-4, 120–130	228.80	NS	NS	BDL	43,900
33X-5, 130–140	278.60	NS	NS	BDL	330,000
39X-3, 130–140	324.20	NS	NS	BDL	27,400
45X-5, 130–140	375.30	NS	NS	BDL	6,320
51X-3, 130–140	420.50	NS	NS	BDL	26,600
204-1251C-					
2X-3, 120–130	11.87	BDL	0.000053	UD	UD
204-1251D-					
3X-4, 120–130	23.30	0.0091	BDL	NS	NS
4H-4, 120–130	32.55	0.024	25	NS	NS
5H-5, 130–140	43.70	0.00022	0.0017	NS	NS
8H-5, 129–139	64.69	0.0075	0.00011	BDL	2,930
11H-4, 100–110	83.29	NS	NS	643	20,100
13H-6, 140–150	105.07	0.00088	0.027	BDL	384
17H-5, 120–130	142.60	0.00052	0.0026	46	1,840
20H-5, 115–125	170.53	0.015	0.0085	BDL	NS
22X-3, 30–40	178.67	0.28	BDL	BDL	275
204-1251E-					
1H-3, 20–30	3.20	BDL	4.6	UD	UD
1H-4, 50–60	5.00	BDL	BDL	UD	UD

Notes: PFT = perfluorocarbon tracer. ag = attograms. NS = not sampled, BDL = below detection limit, UD = unsuccessful deployment.

Table T12. Presence of gas hydrate based on infrared images of cores in liners, Holes 1251B and 1251D.

Core, section	ΔT (°C)	Gas hydrate texture*	Depth interval (mbsf)† Top	Depth interval (mbsf)† Bottom	Anomaly designation‡	Sampled interval Top (cm)	Sampled interval Bottom (cm)	Sampled interval Depth (mbsf)
204-1251B-								
5H	0.80	Disseminated	41.30	42.00	IR28			
5H	0.70	Disseminated	43.00	44.00	IR29			
7H	0.50	Disseminated	61.20	61.30	IR30			
8H	0.70	Disseminated	69.60	69.70	IR31			
8H	0.90	Disseminated	69.90	70.00	IR32			
14H	1.00	Disseminated; possible 5-m-thick zone	116.00	121.00	IR33			
19H	0.50	Disseminated	155.60	155.70	IR34			
19H	0.60	Disseminated	157.00	157.10	IR35			
20H	0.70	Disseminated	166.70	166.80	IR36			
20H	3.50	Disseminated	171.00	171.20	IR37			
22H		Disseminated	173.10	173.20	IR38			
22H		Disseminated	177.30	177.40	IR39			
23H	0.90	Disseminated	188.50	188.60	IR40			
27X	0.70	Disseminated	213.80	214.10	IR41			
43X	0.90	Drilling fluid core or gas expansion? Core cooler from 349.0 to 353.5; typical of XCB?	350.10	350.10	IR42			
204-1251D-								
4H	0.80	Disseminated	33.20	34.20	IR43			
5H	0.70	Disseminated	37.00	38.10	IR44			
8H	0.40	Disseminated	62.00	63.10	IR45			
9H	0.70	Disseminated	67.30	68.00	IR46			
14H	0.80	Disseminated	110.50	111.30	IR47			
15H	1.10	Disseminated	117.40	117.51	IR48			
15H	0.90	Disseminated; possible 5-m-thick zone	118.50	118.60	IR49			
15H	2.00	Disseminated; possible vein	122.50	123.20	IR50			
16H	0.80	Disseminated	134.40	134.50	IR51			
22X-1	1.30	Vein	177.60	177.70	IR52	0	20	175.40
22X-2	1.40	Vein	178.55	178.70	IR53	124	147	178.11
24X-2	3.50	Massive hydrate mixed with sediment?	188.00	189.50	IR54	25	54	189.87
24X-2	6.10	Complex concentrated hydrate with disseminated zone on bottom; sediment in concentrated zone. ΔT is the maximum observed. Average ΔT is ~4°C.	190.00	202.00	IR55	110	150	190.72
25X	1.90	Vein	205.20	205.30	IR56			

Notes: * = from anomaly characteristics and core description, if available. † = from uncut core liner. ‡ = used for reference to specific anomalies in text and figures. The difference between these depth intervals and the equivalent curated section depth intervals is typically <1 m.

Table T13. Moisture and density, Holes 1251B, 1251C, 1251D, and 1251G. (Continued on next page.)

Core, section, interval (cm)	Depth (mbsf)	Density (g/cm³)		Porosity (%)
		Bulk	Grain	
204-1251B-				
5H-1, 74–76	38.34	2.803	3.849	37.0
5H-3, 58–60	41.09	1.601	2.672	65.0
5H-4, 68–70	42.64	1.580	2.654	65.9
5H-5, 74–76	44.20	1.628	2.677	63.5
5H-6, 74–76	45.70	1.626	2.687	63.8
6H-1, 68–70	47.78	1.597	2.633	64.4
6H-2, 74–76	48.66	1.580	2.645	65.7
6H-3, 74–76	50.06	1.626	2.703	64.2
6H-5, 74–76	53.04	1.618	2.658	63.7
6H-7, 48–50	55.19	1.599	2.679	65.2
7H-1, 74–76	57.34	1.610	2.692	64.8
7H-3, 74–76	60.34	1.599	2.674	65.1
7H-5, 74–76	63.34	1.667	2.700	61.7
7H-7, 40–42	65.67	1.657	2.694	62.1
8H-1, 74–76	66.84	1.639	2.711	63.6
8H-3, 84–86	69.94	1.644	2.708	63.2
8H-5, 74–76	72.72	1.666	2.733	62.5
10H-1, 80–82	85.90	1.603	2.685	65.1
10H-2, 82–84	87.42	1.593	2.671	65.4
10H-4, 74–76	90.34	1.617	2.667	63.9
10H-5, 60–62	91.70	1.654	2.714	62.7
11H-1, 74–76	95.34	1.665	2.757	63.0
11H-2, 38–40	96.48	1.702	2.761	60.9
11H-3, 74–76	97.78	1.656	2.692	62.1
11H-4, 74–76	99.28	1.639	2.678	62.8
11H-5, 13–15	100.04	1.683	2.754	61.9
11H-6, 64–66	101.45	1.650	2.682	62.3
12P-1, 10–12	104.20	1.656	2.685	62.0
12P-1, 48–50	104.58	1.685	2.679	60.1
12P-1, 88–90	104.98	1.681	2.683	60.4
13H-1, 77–79	106.87	1.684	2.689	60.3
13H-2, 74–76	107.99	1.703	2.722	60.0
13H-3, 74–76	109.49	1.665	2.627	60.0
13H-5, 20–22	111.75	1.703	2.682	59.1
13H-6, 40–42	113.45	1.681	2.689	60.6
14H-1, 70–72	116.30	1.691	2.673	59.6
14H-3, 74–76	118.85	1.718	2.666	57.7
14H-5, 74–76	121.85	1.703	2.709	59.7
15H-1, 60–62	125.70	1.717	2.681	58.2
15H-2, 50–52	127.10	1.720	2.718	59.0
15H-3, 80–82	128.90	1.683	2.625	58.8
16H-1, 74–76	135.34	1.719	2.687	58.2
16H-3, 76–78	138.36	1.707	2.703	59.3
16H-4, 74–76	139.84	1.768	2.783	57.7
16H-5, 74–76	141.34	1.752	2.732	57.4
17H-1, 74–76	144.84	1.725	2.719	58.7
17H-3, 74–76	147.84	1.758	2.699	56.2
17H-5, 33–35	150.43	1.732	2.702	57.8
18P-1, 9–11	153.69	1.704	2.739	60.3
18P-1, 48–50	154.08	1.736	2.715	57.9
18P-1, 86–88	154.46	1.753	2.643	55.0
19H-1, 74–76	156.34	1.734	2.675	57.0
19H-3, 74–76	159.10	1.727	2.713	58.3
19H-5, 74–76	162.02	1.758	2.748	57.5
20H-3, 74–76	166.92	1.769	2.729	56.3
20H-5, 58–60	169.76	1.752	2.720	57.1
21-Y-1, 20–22	171.90	1.780	2.831	58.2
22H-1, 68–70	173.38	1.775	2.756	56.6
22H-3, 74–76	176.44	1.730	2.674	57.2
22H-3, 98–100	176.68	1.772	2.622	53.2
22H-5, 57–59	179.25	1.731	2.730	58.6
23H-1, 74–76	182.94	1.761	2.693	55.8
23H-3, 74–76	185.94	1.767	2.701	55.7
23H-5, 58–60	188.50	1.752	2.710	56.8
26X-1, 34–36	204.54	1.751	2.710	56.9
26X-3, 38–40	207.58	1.764	2.725	56.5
26X-4, 73–75	209.31	1.730	2.697	57.8
26X-5, 35–37	210.43	1.775	2.820	58.2
27X-1, 74–76	214.24	1.732	2.715	58.1
27X-3, 74–76	217.24	1.741	2.721	57.8
27X-5, 74–76	220.24	1.763	2.686	55.5
28X-1, 74–76	223.84	1.738	2.691	57.2
28X-3, 74–76	226.84	1.725	2.654	57.0
28X-5, 74–76	229.84	1.753	2.722	57.1
29X-1, 74–76	233.54	1.705	2.714	59.7
29X-3, 74–76	236.54	1.723	2.691	58.0
29X-4, 80–82	238.10	1.728	2.679	57.5
30X-1, 74–76	243.14	1.713	2.707	59.1
30X-3, 74–76	246.14	1.780	2.727	55.6
30X-4, 74–76	247.64	1.777	2.738	56.1
31X-1, 74–76	252.84	1.737	2.722	58.0
31X-3, 74–76	255.75	1.746	2.718	57.3
31X-4, 74–76	257.25	1.710	2.687	58.7
32X-1, 74–76	262.44	1.793	2.784	56.3
32X-3, 74–76	265.44	1.823	2.665	51.3
32X-5, 74–76	268.33	1.829	2.750	53.4
33X-1, 78–80	272.08	1.778	2.726	55.7
33X-3, 74–76	275.04	1.811	2.773	55.0
33X-6, 74–76	279.54	1.829	2.755	53.5
34X-1, 76–78	281.76	1.825	2.750	53.6
34X-3, 71–73	284.69	1.766	2.666	54.8
34X-5, 69–71	287.52	1.715	2.692	58.6
35P-1, 13–15	290.73	1.780	2.617	52.6
35P-1, 49–51	291.09	1.830	2.739	53.0
35P-1, 89–91	291.49	1.739	2.632	55.5
36X-1, 74–76	293.34	1.755	2.687	56.0
36X-3, 86–88	296.46	1.805	2.672	52.6
36X-5, 36–38	298.96	1.799	2.662	52.7
37X-1, 90–92	301.50	1.832	2.697	51.7
37X-3, 54–56	304.14	1.800	2.721	54.3
37X-4, 30–32	305.40	2.529	2.695	10.0
37X-5, 86–88	307.46	1.749	2.637	55.0
38X-1, 74–76	311.04	1.778	2.662	53.9
38X-3, 36–38	313.66	1.758	2.689	55.9
38X-5, 78–80	317.08	1.865	2.734	50.8
39X-1, 76–78	320.66	1.721	2.588	55.5
39X-2, 70–72	322.10	2.645	2.910	14.0
39X-2, 111–113	322.51	1.761	2.619	53.8
39X-4, 15–17	324.55	1.684	2.591	57.9
41X-3, 18–20	333.78	1.683	2.786	62.6
41X-3, 74–76	334.34	1.682	2.674	60.1
41X-5, 98–100	337.58	1.629	2.603	61.7
42X-1, 60–62	339.80	1.725	2.814	60.8
42X-3, 79–81	342.99	1.643	2.611	61.0
42X-5, 82–84	346.02	1.690	2.682	59.8
43X-1, 73–75	349.53	1.697	2.790	61.9
43X-3, 67–69	352.47	1.630	2.672	63.3
43X-5, 72–74	355.49	1.710	2.730	59.8
44X-1, 72–74	359.12	1.669	2.767	63.0
44X-3, 73–75	362.13	1.655	2.746	63.4
44X-5, 77–79	365.17	1.692	2.693	60.0
45X-1, 108–110	369.08	1.842	2.955	57.6
45X-3, 66–68	371.66	1.816	2.890	57.6
45X-6, 14–16	375.64	1.745	2.836	60.2
46X-1, 36–38	377.96	1.783	2.836	58.1
46X-3, 68–70	381.28	1.700	2.696	59.6
46X-5, 66–68	384.26	1.692	2.621	58.2
47X-1, 62–64	387.92	1.698	2.645	58.4
47X-3, 88–90	391.18	1.712	2.662	58.0
47X-5, 78–80	394.08	1.749	2.775	58.6
49X-1, 66–68	398.56	1.720	2.707	58.6
49X-3, 63–65	401.53	1.738	2.734	58.3
49X-5, 42–44	404.32	1.703	2.715	59.8
50X-1, 100–102	407.50	1.689	2.613	58.2
50X-3, 80–82	410.30	1.698	2.640	58.3
50X-5, 70–72	413.20	1.716	2.606	56.3
51X-1, 74–76	416.94	1.805	2.747	54.7

Table T13 (continued).

Core, section, interval (cm)	Depth (mbsf)	Density (g/cm³) Bulk	Density (g/cm³) Grain	Porosity (%)
51X-4, 59–61	421.29	1.731	2.657	56.7
51X-6, 59–61	424.22	1.703	2.666	58.6
52X-1, 90–92	426.70	1.768	2.705	55.7
52X-3, 71–73	429.51	1.714	2.657	57.8
52X-5, 74–76	432.54	1.660	2.516	57.4
53X-1, 108–110	436.58	1.722	2.721	58.9
53X-3, 111–113	439.59	1.692	2.628	58.3
53X-5, 50–52	441.21	1.683	2.623	58.8
204-1251C-				
1H-1, 74–76	0.74	1.407	2.679	76.9
1H-2, 74–76	2.24	1.437	2.743	76.0
1H-3, 74–76	3.74	1.463	2.567	71.5
1H-4, 74–76	5.24	1.497	2.686	71.5
1H-5, 74–76	6.74	1.468	2.589	71.6
2X-1, 20–22	8.30	1.502	2.633	70.3
2X-1, 74–76	8.84	1.517	2.686	70.3
2X-1, 128–130	9.38	1.548	2.778	70.1
2X-2, 30–32	9.90	1.478	2.651	72.1
2X-2, 58–60	10.18	1.472	2.732	73.8
2X-2, 74–76	10.34	1.581	2.664	66.0
2X-2, 94–96	10.54	1.549	2.680	68.3
2X-3, 50–52	11.17	1.606	2.795	67.1
2X-3, 75–77	11.42	1.582	2.735	67.4
2X-3, 102–104	11.69	1.904	2.698	47.4
2X-4, 40–42	12.57	1.603	2.604	63.3
2X-4, 91–93	13.08	1.942	2.713	45.6
204-1251D-				
1X-1, 40–42	0.40	1.434	2.671	75.1
1X-1, 109–111	1.09	1.455	2.687	74.1
1X-2, 49–51	1.99	1.492	2.806	73.7
1X-3, 30–32	2.80	1.474	2.579	71.1
2X-1, 70–72	8.80	1.451	2.608	73.0
2X-2, 33–35	9.93	1.485	2.742	73.2
2X-2, 71–73	10.31	1.535	2.654	68.6
2X-3, 20–22	10.80	1.611	2.735	65.7
2X-3, 47–49	11.07	1.563	2.733	68.4
3X-1, 52–54	18.12	1.536	2.634	68.2
3X-2, 74–76	19.84	1.625	2.672	63.5
3X-3, 68–70	21.28	1.587	2.684	66.1
3X-4, 28–30	22.38	1.566	2.702	67.7
3X-5, 76–78	24.36	1.586	2.660	65.6
3X-6, 50–52	25.10	1.612	2.681	64.5
4H-1, 80–82	27.70	1.595	2.660	65.1
4H-2, 78–80	29.18	1.605	2.712	65.6
4H-3, 74–76	30.59	1.661	2.702	62.1
4H-3, 140–142	31.25	1.650	2.680	62.2
4H-5, 42–44	33.27	1.619	2.675	63.9
4H-6, 54–56	34.39	1.639	2.705	63.4
5H-1, 20–22	36.60	1.636	2.687	63.2
5H-1, 74–76	37.14	1.626	2.678	63.6
5H-2, 74–76	38.64	1.663	2.680	61.4
5H-3, 20–22	39.60	1.649	2.696	62.6
5H-3, 74–76	40.14	1.663	2.625	60.1
5H-3, 144–146	40.84	1.659	2.589	59.4
5H-4, 74–76	41.64	1.624	2.656	63.3
5H-5, 50–52	42.90	1.611	2.610	63.0
5H-6, 92–94	44.82	1.614	2.675	64.3
5H-740–42	45.38	1.613	2.714	65.2
6P-1, 9–11	45.99	1.575	2.745	68.0
6P-1, 50–52	46.40	1.574	2.785	68.8
6P-1, 77–79	46.67	1.630	2.905	67.8
9H-1, 40–42	67.30	1.640	2.644	62.0
9H-2, 74–76	69.14	1.641	2.656	62.2
9H-3, 74–76	70.64	1.642	2.661	62.2
9H-4, 74–76	72.14	1.638	2.640	62.0
9H-5, 82–84	73.60	1.627	2.639	62.7
9H-6, 48–50	74.76	1.670	2.768	63.0
10P-1, 17–19	76.57	1.686	2.821	63.1
10P-1, 47–49	76.87	1.690	2.733	61.0
10P-1, 81–83	77.21	1.663	2.734	62.6
11H-1, 50–52	78.90	1.635	2.729	64.2
11H-3, 74–76	81.53	1.645	2.700	63.0
11H-5, 74–76	84.53	1.615	2.693	64.6
13H-2, 100–102	98.74	1.670	2.634	59.9
13H-3, 74–76	99.98	1.673	2.717	61.6
13H-4, 109–111	101.76	1.684	2.680	60.2
13H-6, 70–72	104.37	1.638	2.651	62.3
13H-750–52	105.01	1.674	2.633	59.6
20H-1, 74–76	164.64	1.689	2.673	59.7
20H-2, 49–51	165.37	1.726	2.778	60.0
20H-6, 74–76	171.62	1.776	2.789	57.4
21P-1, 8–10	173.48	1.766	2.754	57.1
21P-1, 49–51	173.89	1.687	2.650	59.2
21P-1, 88–90	174.28	1.670	2.684	61.1
23X-1, 74–76	179.84	1.655	2.704	62.4
23X-3, 74–76	182.81	1.765	2.761	57.3
23X-5, 39–41	184.96	1.714	2.727	59.5
24X-1, 74–76	189.34	1.708	2.735	60.0
24X-3, 94–96	192.06	1.728	2.708	58.2
24X-5, 74–76	193.99	1.746	2.781	58.9
25X-1, 74–76	198.94	1.731	2.719	58.3
25X-3, 74–76	201.94	1.777	2.731	55.9
25X-6, 74–76	206.44	1.754	2.709	56.7
29P-1, 8–10	227.58	1.685	2.682	60.1
29P-1, 51–53	228.01	1.617	2.607	62.5
29P-1, 78–80	228.28	1.731	2.708	58.0
204-1251G-				
2P-1, 8–10	20.08	1.587	2.703	66.4
2P-1, 50–52	20.50	1.583	2.703	66.7
2P-1, 82–84	20.82	1.584	2.708	66.7

Table T14. Compressional wave velocity measurements, Hole 1251B.

Core, section, interval (cm)	Depth (mbsf)	Velocity (m/s)
204-1251B-		
1H-1, 47.5	0.47	1539.8
1H-1, 50.0	0.50	1536.0
1H-1, 52.5	0.52	1528.6
1H-1, 55.0	0.55	1528.1
1H-1, 57.1	0.57	1557.0
23X-2, 70.0	184.40	3913.0

Table T15. Thermal conductivity, Holes 1251B, 1251C, and 1251D.

Core, section, interval (cm)	Depth (mbsf)	Thermal conductivity (W/[m·K])	Individual measurements (W/[m·K])		
204-1251B-					
1H-3, 75	3.75	0.859	0.878	0.853	0.845
3H-3, 75	22.28	0.879	0.874	0.898	0.866
4H-1, 75	28.85	0.818	0.809	0.794	0.850
4H-3, 75	31.85	0.788	0.790	0.782	0.792
4H-5, 75	34.85	0.881	0.904	0.849	0.889
5H-3, 75	41.26	0.847	0.841	0.865	0.836
6H-3, 75	50.07	0.856	0.852	0.850	0.866
7H-1, 75	57.35	0.721	0.725	0.715	0.724
7H-3, 75	60.35	0.835	0.836	0.818	0.850
7H-5, 75	63.35	0.945	0.949	0.912	0.973
8H-3, 75	69.85	0.860	0.874	0.852	0.853
8H-5, 75	72.73	0.932	0.917	0.930	0.949
10H-3, 75	88.85	0.934	0.943	0.923	0.937
10H-5, 75	91.85	0.957	0.980	0.938	0.954
11H-3, 75	97.79	0.938	0.943	0.931	0.941
13H-3, 75	109.50	0.804	0.796	0.815	0.802
14H-1, 50	116.10	0.997	1.004	1.011	0.975
14H-3, 72	118.83	1.005	0.987	0.995	1.033
14H-5, 65	121.76	0.942	0.951	0.952	0.924
15H-3, 50	128.60	0.998	1.055	0.960	0.979
16H-3, 75	138.35	0.931	0.939	0.933	0.921
17H-3, 75	147.85	1.044	1.058	1.045	1.029
19H-1, 60	156.20	0.995	0.988	1.000	0.997
19H-3, 75	159.11	0.833	0.841	0.838	0.819
19H-5, 69	161.97	0.854	0.844	0.864	0.855
22H-1, 30	173.00	1.032	1.049	1.058	0.989
22H-3, 69	176.39	0.968	0.987	0.952	0.966
23H-3, 75	185.95	1.042	1.081	1.040	1.004
26X-1, 75	204.95	0.993	1.006	0.976	0.997
26X-3, 75	207.95	0.962	0.965	0.970	0.952
27X-1, 75	214.25	0.937	0.953	0.933	0.925
27X-3, 75	217.25	0.943	0.969	0.934	0.925
28X-3, 75	226.85	1.011	1.009	1.029	0.994
29X-1, 75	233.55	0.941	0.936	0.935	0.953
29X-3, 75	236.55	1.031	1.022	1.036	1.035
30X-3, 72	246.12	0.997	0.977	0.995	1.018
31X-3, 75	255.76	0.922	0.911	0.942	0.914
32X-3, 72	265.42	1.053	1.070	1.050	1.039
33X-3, 75	275.05	1.013	1.013	1.032	0.993
34X-3, 70	284.68	0.965	0.986	0.967	0.943
36X-3, 75	296.35	1.044	1.022	1.035	1.076
37X-3, 75	304.35	0.971	0.998	0.960	0.956
38X-3, 75	314.05	0.875	0.876	0.873	0.877
39X-4, 120	325.60	1.033	1.047	1.020	1.031
41X-1, 50	331.10	0.926	0.933	0.927	0.918
41X-4, 40	335.50	0.983	1.000	0.958	0.991
42X-1, 110	340.30	0.983	0.980	0.986	0.983
42X-3, 110	343.30	0.914	0.923	0.914	0.906
43X-3, 100	352.80	0.841	0.853	0.832	0.837
44X-1, 100	359.40	0.918	0.934	0.897	0.924
44X-3, 90	362.30	0.963	0.962	0.970	0.957
45X-3, 70	371.70	1.036	1.048	1.018	1.043
46X-3, 114	381.74	0.946	0.938	0.940	0.961
47X-3, 67	390.97	0.932	0.929	0.956	0.921
49X-3, 74	401.64	0.987	0.995	0.960	1.005
50X-3, 78	410.28	0.971	0.967	0.986	0.960
51X-4, 66	421.36	0.930	0.945	0.904	0.940
52X-3, 38	429.18	0.909	0.900	0.893	0.933
53X-3, 75	439.23	0.990	1.016	0.977	0.978
53X-5, 50	441.21	0.872	0.889	0.867	0.861
204-1251C-					
1H-3, 75	3.75	0.932	0.950	0.896	0.949
204-1251D-					
1X-2, 45	1.95	0.846	0.855	0.845	0.837

Table T16. Shear strength values, Hole 1251B.

Core, section, interval (cm)	Depth (mbsf)	Torvane size	Shear strength (kPa)
204-1251B-			
1H-1, 69–71	0.70	L	4
1H-3, 63–67	3.65	L	8
1H-6, 66–70	8.18	L	11
3H-2, 80–82	20.84	M	31
3H-4, 63–67	23.66	M	30
4H-2, 118–120	30.79	M	31
4H-4, 60–62	33.21	M	43
5H-3, 120–122	41.72	M	47
5H-6, 30–32	45.27	M	45
6H-6, 59–61	54.31	M	48
7H-5, 60–62	63.21	M	55
7H-7, 54–56	65.82	M	65
8H-1, 30–32	66.41	M	53
10H-4, 70–72	90.31	M	32
10H-5, 30–32	91.41	M	40
11H-2, 26–28	96.37	M	30
11H-5, 55–57	100.60	M	62
13H-4, 121–123	111.47	M	49
14H-1, 40–42	116.01	M	45
15H-1, 40–42	125.51	M	85
16H-3, 110	138.70	S	117
16H-5, 30	140.90	S	112
17H-3, 86	147.96	S	112
19H-4, 109	160.87	S	145
19H-4, 75	174.95	S	162
20H-2, 63	165.31	S	140

Note: L = large, M = medium, S = small.

Table T17. Temperature measurements at Site 1251.

Hole, core	Depth (mbsf)	Temperature (°C)	Thermal conductivity (W/[m·K])	Tool ID
204-				
1251B-4H	37.6	5.84	0.88	12
1251B-7H	66.1	7.53	0.94	12
1251B-10H	94.6	9.18	0.96	12
1251B-14H	125.1	11.02	0.94	12
1251D-20H	173.4	13.21	0.95	12
1251B-18P–19H	155.6	14.80	—	3*
1251D-21X–22X	175.4	13.43	—	2
1251D-24X–25X	198.6	9.75	—	2*
1251B-35P–36X	292.6	19.50	—	2

Notes: Measurements for which two core numbers are given (e.g., Section 204-1251B-18P-19) were made with the DVTPP between these two cores. APCT measurements were made at the core catcher of the core listed. No thermal conductivity values are given for the DVTPP data because no extrapolation was done. For APCT measurements, thermal conductivity represents the average of the nine measurements taken in the adjacent core. A star in the last column indicates that this measurement was not used in the calculation of subsurface thermal gradient. ID = identification.

Table T18. Results from degassing experiments, Holes 1251B, 1251D, and 1251G.

Core	Depth (mbsf) Top	Depth (mbsf) Bottom	Run time (min)	Total volume (mL)*	Volume (mL)† $O_2 + N_2$	Volume (mL)† C_1	Volume (mL)† CO_2	Volume (mL)† C_{2+}	Concentration (%)‡ $O_2 + N_2$	Concentration (%)‡ C_1	Concentration (%)‡ CO_2	Concentration (%)‡ C_{2+}	Core length (m)	Porosity (%)	C_1 (mM)**
204-1251B-															
12P	104.1	105.1	1169	3365	144.9	3194.8	25.2	0.05	4.3	94.9	0.7	0.002	0.99–1.00	61	146.3–147.8
18P	153.6	154.6	1411	3180	1692.6	1479.0	8.4	0.04	53.2	46.5	0.3	0.001	0.99–1.00	58	71.4–72.1
35P	290.6	291.6	1357	2975	79.3	2892.3	2.7	0.67	2.7	97.2	0.1	0.022	0.95–1.00	54	149.7–157.6
204-1251D-															
6P	45.9	46.9	837	2282	466.1	1809.6	6.3	0.03	20.4	79.3	0.3	0.001	0.82–1.00	64	79.2–96.6
10P	76.4	77.4	672	1890	779.0	1105.1	6.0	0.00	41.2	58.5	0.3	0.000	0.99–1.00	63	49.0–49.5
21P	173.4	174.4	1023	3015	1134.3	1874.8	5.9	0.03	37.6	62.2	0.2	0.001	0.94–1.00	57	91.0–96.8
29P	227.5	228.5	1567	1905	102.9	1798.7	3.1	0.25	5.4	94.4	0.2	0.013	0.81–1.00	57	88.6–109.4
204-1251G-															
2P	20	21	1237	1320	219.7	1094.7	5.6	0.01	16.6	82.9	0.4	0.001	0.91–1.00	66	46.9–51.5

Notes: * = volume of gas released. † = volume of components released. ‡ = concentration of components released. ** = concentration in situ. Core length is reported as measured after the core was degassed and split (i.e., curator length) and as cored in subsurface.

Table T19. HYACINTH pressure coring summary, Holes 1251B and 1251D.

Core	Deployment number	Date (Jul 2002)	Local time (hr)	Depth Water (mbsl)	Depth Core (mbsf)	BSR (mbsf)	Lithology	Core recovered (cm)	Pressure (kbar)	Comments
204-1251B-										
21Y	FPC 1	27	2000	1224	171	193	Lightly indurated silty clay	71 (0 curated)	0	20 m above BSR; full stroke, no retraction; core exploded on deck; DSA and FPC logger did not function correctly.
40Y	FPC 2	28	2210	1224	329	193	Well indurated silty clay	0	0	250 m below BSR; full retraction; internal implosion of liner; lower valve failed to seal; DSA and FPC logger did not function correctly.
48E	HRC 1	29	1155	897	397	193	Stiff indurated silty clay	0	0	Tool diassembled vertically; end of stroke not reached; core liner broken; no retraction.
204-1251D-										
28Y	FPC 3	31	1500	1224	226	193	Moderately indurated silty clay	78	0	Cut good core upper seal dislodged; no retraction; DSA logger worked partially; FPC logger functioned correctly.
30E	HRC 2	31	1830	897	229	193	Moderately indurated silty clay	22	20 0	Full retraction; sealed; stuck in transfer chamber.

Note: BSR = bottom-simulating reflector, DSA = drill string acceleration tool, FPC = Fugro Pressure Corer.

Table T20. Conventional wireline logging operations summary, Hole 1251H.

Date (Aug 2002)	Local time (hr)	Tool depth (mbsf)	Remarks
17	0115		Drilling completed
17	0115–0130	445.0	Hole swept with sepiolite mud
17	0130–1015		Wiper trip up to 80 mbsf; back down to 440 mbsf
17	1200–1230	414.8	Hole displaced with sepiolite mud
17	1230–1415		Set back top drive; bottom of pipe put at 94.5 mbsf
17	1415		Start logging rig-up
17	1630		Start going down the triple combination (TAP/DIT/HLDT/APS/HNGS/QSST) tool string
17	1730	0.0	Stop 5 min at mudline for temperature calibration
17	1800	240.5	Tool at TD; start logging-up pass at 900 ft/hr
17	1910	78.5	Tool back into pipe; speed up to 1500 ft/hr to log mudline
17	1920	0.0	End of pass 1
17	1935	225.5	Tool at TD for QSST checkshot survey
17	2015	225.5	Tool at TD; start logging-up pass 2 at 900 ft/hr
17	2045	78.5	Tool back in pipe; end of pass 2
17	2120		Tool back on rig floor
17	2245		Finish rig down
17	2245		Start logging rig-up
17	2345		Start going down with the FMS-sonic (FMS/DSI/SGT) tool
18	0055	207.5	Tool at TD; start logging-up pass at 900 ft/hr
18	0125	78.5	Tool back into pipe; end of pass 1
18	0145	209.5	Tool at TD; start logging-up pass 2 at 900 ft/hr
18	0215	78.5	Tool back into pipe; end of pass 2
18	0245		Tool back on rig floor
18	0345		Finish rig-down

Note: TD = total depth. See Table **T8,** p. 102, in the "Explanatory Notes" chapter for definitions of acronyms.